이학박사 학위논문

Studies on Direct Synthesis of Transition Metal Dichalcogenides for Electronic Applications

전자소자로 응용을 위한 전이금속계화합물의 직접 합성에 관한 연구

2021년 8월

서울대학교 대학원

화학부 물리화학 전공

박 성 웅

Studies on Direct Synthesis of Transition Metal Dichalcogenides for Electronic Applications

Advisor : Prof. Byung Hee Hong

Submitting a Ph.D. Dissertation of Chemistry

August 2021

Graduate School of Natural Sciences

Seoul National University

Chemistry Major

Seoungwoong Park

Confirming the Ph.D. Dissertation written by

Seoungwoong Park

August 2021

Chair _____

Vice Chair _____

Examiner _____

Examiner _____

Examiner _____

Abstract of Dissertation

Studies on Direct Synthesis of Transition Metal Dichalcogenides for Electronic Applications

Seoungwoong Park
Department of Chemistry
The Graduate School
Seoul National University

Transition metal dichalcogenides (TMDC) have been identified as excellent platforms for developing the next-generation commercial flexible logic devices and sensors, owing to their outstanding mechanical, optical, and electrical properties. The TMDCs can be used to produce novel form-factors for wearable electronic devices. Typically, synthesis of large-scale TMDC thin film have been achieved by complexity vacuum-based approach. Therefore, it is essential to develop a simple and effective method to boost-up mass production of TMDC thin films on a large scale upon arbitrary substrates. In this regard, the solution-based TMDC synthesis method is advantageous because it proposes a simplification of the fabrication processes and an easy scaling-up of the material with a non-vacuum system.

In Chapter 1, we summarize the evolution of the solution-based thin-film preparation and synthesis of the TMDCs; subsequently, we discuss the

merits and drawbacks of the recently developed methods to form TMDC thin films directly from the deposited precursor. Finally, we discuss the practical applications of the TMDC thin films, which demonstrate the feasibility of their commercialized applications in electronic devices and sensors.

In Chapter 2, we introduce a direct and rapid method for layer-selective synthesis of MoS_2 and WS_2 structures in wafer-scale using a pulsed laser annealing system (λ = 1.06 μm, pulse duration ~100 ps) in ambient conditions. As a proof of concept, we demonstrated the behavior of a MoS_2-based field-effect transistor, a skin-attachable motion sensor, and a MoS_2/WS_2-based heterojunction diode in this study.

In Chapter 3, we demonstrate synthesis technique to adjusting MoS_2 morphological structure, so that a surface-crumpled MoS_2 TENG device generates ~40% more power than a flat MoS_2 one. Compared to other MoS_2-based TENG devices, it shows high-performance energy harvesting (up to ~25 V and ~1.2 μA) without assistance from other materials, even when the counterpart triboelectric surface has a slightly different triboelectric series.

In Chapter 4, the summary and conclusion of the thesis are depicted, finally.

Keywords: Transition metal dichalcogenides, Laser annealing, Solution-based process, Electronic devices, Strain sensors.

Student Number: 2019-35429

Table of Contents

List of Figures and Tables

Chapter 1.

Chapter 2.

Chapter 3.

Chapter 1.

Introduction of Large-Scale Synthesis of Transition Metal Dichalcogenides

[*The contents of this chapter is reproduced from: Seoung-Woong Park, Yong Jun Jo, Sukang Bae, Byung Hee Hong, and Seoung-Ki Lee* *Applied Science and Convergence Technology* (2020) 29 (6), 133-142.

1.1. Introduction

Two-dimensional (2D) materials provide a versatile platform for investigating various electronic and optoelectronic phenomena. Since the exfoliated graphene was demonstrated in 2004, 2D materials have been one of the central research topics in the last two decades in the field of material science [1], physics [2], and electronics, [3, 4] providing. Various merits and applications of 2D materials have been verified through numerous analytical methods. In the next step, the synthesis of large-area 2D materials for their commercialization has become the focus of subsequent investigations. Bae and co-workers [5] developed the method of scaling-up of graphene, grown up to 30 inches by the chemical vapor deposition (CVD) method. Since then, various progressive strategies have been introduced for the production of high-quality graphene, even by companies, such as Sony [6] and Samsung [7].

The successful scalability of graphene boosted the mass production of

other 2D materials, which belong to the family of transition metal dichalcogenide (TMDC) [8]. The TMDCs, which have semiconducting characteristics, are preferred as the target materials for developing the next-generation electronic devices because of their unique properties, such as direct or indirect band gap modulation [9], quantum-confinement [10], transparency [11], and flexibility [12]. Therefore, the uniform synthesis of TMDCs on a large-scale is important to accelerate their mass production [13, 14]. Large-area TMDC thin films can be successfully fabricated via CVD, which can be used to grow vertically or horizontally stacked heterostructures [15–17]. However, the CVD-based synthesis is limited by several factors, such as the requirement of high temperatures (≈ 1000 °C), difficulties in modulating the deposited film thickness to a desired value, and long processing time, which cause delay in the material preparation [18]. Recently, solution-phase deposition methods have been reported, which have several technical advantages, such as relatively low processing temperature [19], compatibility with various substrates, including polymer film (e.g. polyimide (PI)) [20], easily controlled layer thickness [20], rapid synthesis, and scalability with the help of existing coating techniques [21]. Recently, the lithography-free approach has been developed to form patterns directly on a TMDC film [22–24]. In this paper, we review an industrially applicable solution-based TMDC synthesis method, involving trial and error of the solution-phase deposition and its underlying mechanisms. Further, we discuss the corresponding applications, such as in transistors, sensors, and

diodes, in detail. The achievements of the advanced synthesis method include large-scale fabrication of novel TMDC thin films for industrial applications.

1.2. Synthesis of TMDC thin films by thermolysis

Solution-phase synthesis of TMDC thin film is generally performed in several steps: the preparation of a precursor solution, deposition of the precursor, and conversion of the precursor`s chemical structure. The thickness or uniformity of the synthesized TMDC film can be adjusted by controlling the precursor concentration, solution composition, and coating environment. In this section, we review the development of various deposition and synthesis methods for fabricating TMDC thin films.

1.2.1 Principles of thermolysis

The solution-deposited TMDC compounds are usually synthesized by thermolysis of a precursor $[A]_{nb}[MX]_{a+n}$, where A is a cation that facilitates dissolution in the solvent, M is a transition metal, and X is a chalcogen that produces charge balance between A and M to support the precursor structure. MX is the anion in the precursor structure. This MX anion has a high bonding strength, which maintains its structure via the chalcogen bonding.

For example (Fig. 1-1 a), synthesis of MoS_2 requires an ammonium thiomolybdate ($[NH_4]_2[Mo_3S_{13}\cdot 2H_2O]$) precursor and a two-step thermolysis [25]. The precursor dissolves in a solvent as an anion $[Mo_3S_{13}]^{2-}$ and a cation $[NH_4]^{2+}$.

In the first step, at temperatures $120 \leq T \leq 360$ ℃ (where T represents temperature), the $[Mo_3S_{13}]^{2-}$ clusters cleave along an intermolecular bonding weakness to produce sulfur as H_2S. Additionally, as the bond strength of the Mo–Mo bond in Mo_3S_{13} obtained by a thermal reaction gradually weakens, it decomposes to amorphous MoS_4. Subsequently, for $T \geq 440$ °C, the remaining Mo–S bond breaks to yield a poorly crystallized MoS_2. The second thermolysis reaction produces sulfur as well as emits H_2S gas that escapes from the precursor, thereby producing a sulfur vacancy; therefore, to ensure a stable reaction, H_2 or H_2S gas is injected constantly into the reaction chamber. On completion of the reaction, MoS_2 is synthesized as a bulk structure (rod, wire, and dot) instead of being deposited on a specific substrate (Fig. 1-1 a, right). Generally, $[NH_4]_2[Mo_3S_{13}]$ has a high molecular weight; therefore, it is difficult to control the layer thickness, and this drawback impedes the formation of atomically thin TMDC films.

As an alternative precursor, ammonium tetrathiomolybdate (ATM, $[NH_4]_2MoS_4$) is used to facilitate thermal decomposition for the fabrication of the MoS_2 film [18] (Fig. 1-1 b). In the ATM structure, $[NH_4]_2$ is a cation; Mo maintains the bonding as the center of the precursor, and S_4 maintains the precursor structure. Prior to the two-step thermolysis, ATM is deposited on a specific substrate and all residual solvents are removed by heating at 100 °C. Next, amorphous MoS_3 is synthesized at $120 \leq T \leq 360$ °C in the first thermolysis step. In the second thermolysis step, a thin film of MoS_2 is

synthesized under an atmosphere of a mixture of Ar and S (i.e., Ar + S), with Ar injected into the chamber at $T \geq 440$ °C. The crystallinity of thermally decomposed MoS_2 can be improved by increasing T to 820 °C during the second thermolysis step [26].

1.2.2. Characteristics

The Raman spectral characteristics are generally used to analyze the intrinsic property of the TMDCs (MoS_2, WS_2, $MoSe_2$, WSe_2, and etc). Liu et al. [12, 27] comparatively analyzed the Raman spectrum of the thermally decomposed MoS_2 films on sapphire substrate, under Ar and Ar+S atmosphere. Fig. 1-1 c shows two representative Raman absorption peaks, which are ascribed to the E^1_{2g} and A_{1g} modes of the MoS_2 vibration. The E^1_{2g} mode reflects the in-plane vibration and A_{1g} mode reflects the out-of-plane vibration of the MoS_2 as the difference in the energy level of electron from Raman absorption. A higher intensity of the Raman peak implies a better quality of the MoS_2 film. Therefore, the sulfur gas aids in the filling of the sulfur vacancy, thereby enhancing the quality of the MoS_2 film during thermolysis. In Fig. 1-1 d, the frequency difference between the A_{1g} and E^1_{2g} modes ($\Delta\omega = \omega_{A_{1g}} - \omega_{E_{2g}}$) can be used to identify the number of layers of the synthesized MoS_2 (Fig. 1-1 d, bottom). The Raman mode spacing is considerably narrow ($\Delta\omega \approx 25$ cm^{-1}), which indicates that the MoS_2 film is composed of five layers; a mono layer has $\Delta\omega \approx 16.5$ cm^{-1} [28, 29]. As the number of layers of the synthesized MoS_2 approaches one, this

synthesized monolayer develops a direct band gap and has optical properties; it absorbs light of a specific wavelength (672 nm). Fig. 1-1 e shows the photoluminescence (PL) of a tri-layer MoS_2 film, thermally decomposed on a sapphire substrate. The PL peaks also exhibit a stronger intensity when Ar+S gas mixture is injected; the result indicates that a MoS_2 film of better quality is formed. Next, X-ray photoelectron spectroscopy (XPS) analysis was conducted to identify the chemical composition of the thermally decomposed MoS_2 film (Fig. 1-1 f). The Mo 3d shows two peaks at 229.3 and 232.5 eV, which are attributed to Mo $3d_{5/2}$ and S 2s peaks, indicating that the chemical composition of the MoS_2 film exists during the 2H phase formation. The S 2p peaks, shown in the inset, indicate the intramolecular bonding of divalent sulfide ions (S^{2-}). Accordingly, the two distinguished peaks are observed approximately at 163.3 and 162 eV, corresponding to the S $2p_{1/2}$ and S $2p_{3/2}$ orbital splits. As a result, it is possible to verify the intrinsic chemical composition of MoS_2 through the thermolysis of $[NH_4]_2MoS_4$. Additionally, the thickness modulation of a synthesized MoS_2 film can be demonstrated by adjusting the concentration of the ATM precursor [20]. Fig. 1-1 f shows the atomic force microscopy (AFM) image of a MoS_2 thin film, synthesized through a two-step thermolysis reaction with different concentrations of ATM precursor. Thus, a MoS_2 thin film, with one (0.65 nm) to a few layers (3.2 nm), can be synthesized by a two-step thermolysis method.

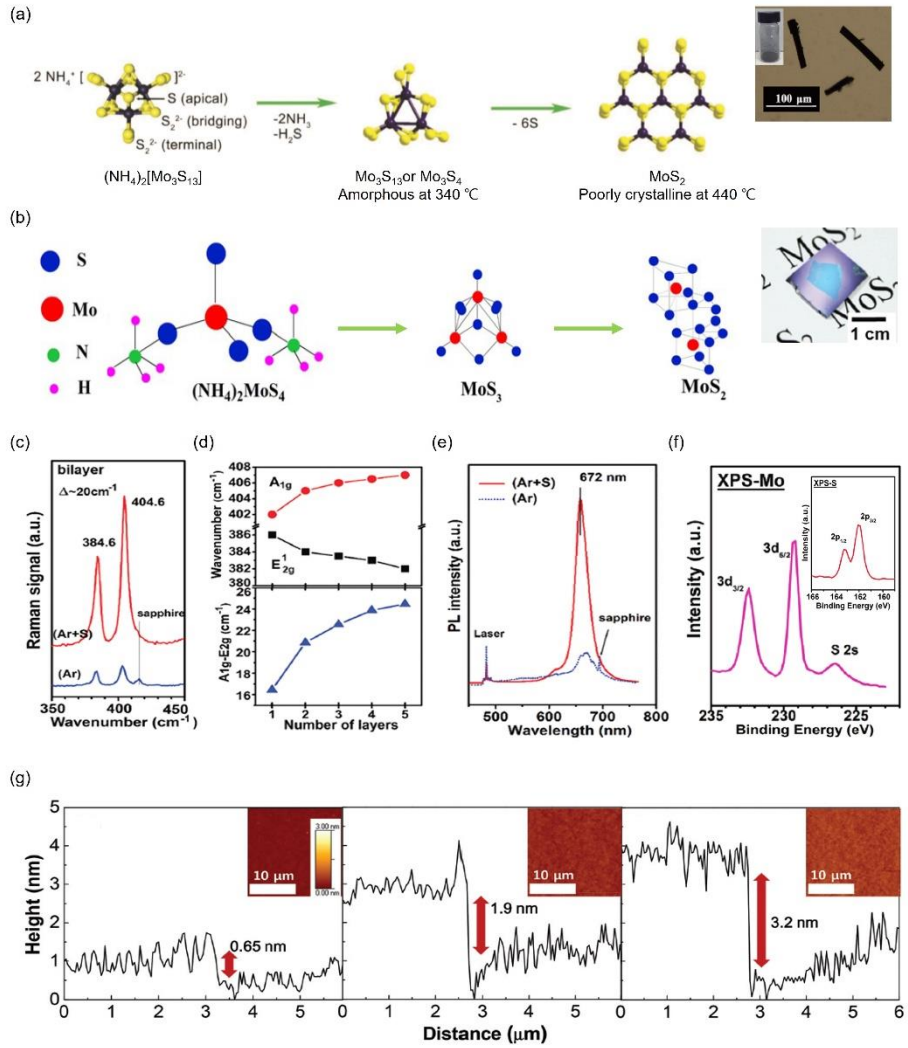

Figure 1-1. (a) Schematic of the chemical composition of bulk-type MoS_2 formation from $(NH_4)_2$ $[Mo_3S_{13}]$. (Reprinted with permission from A. Giri et al., Adv. Mater. 30, 1707577 (2018), © 2020, John Wiley and Sons [18]). Optical microscope image of rod-type MoS_2 (right). (Reprinted with permission from Z. Huang et al., Angew. Chem. Int. Ed. Engl. 54, 15181 (2015), © 2020, Elsevier [43]). (b) Schematic representation of the synthesis of thin-film MoS_2 via two-step thermolysis from $(NH_4)_2[MoS_4]$. (Reprinted with permission from T. Zhang et al., Chem. Asian J. 11, 1392-2398 (2016), © 2020, John Wiley and

Sons [44]). Optical microscopic image of synthesized MoS_2 thin film on SiO_2/Si substrate (right). (c) Raman spectra of two-step thermally decomposed MoS_2 under Ar or Ar+S atmosphere. (d) Energies of the two characteristic peaks: Variation of the spacing between E_{2g} and A_{1g} with number of MoS_2 layers. (e) PL intensity of the thermally decomposed triple layered MoS_2 film. (f) XPS spectra of the thermally decomposed MoS_2 film: Mo 3d and S 2s peaks. (Reprinted with permission from Liu et al., Nano Letters 12, 1538-1544 (2012), © 2020, American Chemical Society [27]). (g) Surface topographic images (insets) and cross-sectional height profile of the thermally decomposed MoS_2 with thickness modulation by adjusting $(NH_4)_2[MoS_4]$ concentration. (Reprinted with permission from H. Yang et al., Nanoscale 7, 9311-9319 (2015), © 2020, Royal Society of Chemistry [20]).

1.2.3. Synthesis of TMDC films on a large scale

To synthesize a TMDC film from a solution on an arbitrary substrate (*e.g.*, SiO_2/Si, and sapphire), it is important to monitor the precursor deposition since it determines the scale, thickness, and patterning of the TMDC films. Here, we first describe the dip coating deposition method, which is proposed by Liu and co-workers [27]. In this method, $(NH_4)_2MoS_4$ is dissolved in dimethylformamide (DMF) to form a precursor solution. A SiO_2 substrate that is prepared via the oxygen treatment is immersed into the $(NH_4)_2MoS_4$ solution. Next, the substrate is pulled out slowly (0.5 mm s^{-1}) from the solution. The deposition yield of $(NH_4)_2MoS_4$ film is determined by the precursor–substrate wettability and separation speed. The process is very simple; however, controlling the thickness

of the precursor layer is difficult; thus, this method is not suitable for the mass production of TMDC films.

Fig. 1-2 a illustrates the spin-coating strategy to obtain wafer-scale MoS_2 thin films through the dissolution of $(NH_4)_2MoS_4$ in n-methylpyrolidone (NMP) [30]. Spin coating is widely used to deposit photoresists during the semiconductor manufacturing; the coating thickness can be controlled easily by varying the rotation speed. Therefore, using the spin coating method, the precursor film thickness can be controlled by varying the concentration of the solution and rotating speed, thereby yielding precisely tuned mono-/bi-/tri-layers of the thermally decomposed MoS_2 film. Spin coating is advantageous for thickness control; however, only one solvent is used; therefore, the wetting of a substrate is low. As a result, the viscosity or surface tension of a precursor cannot be controlled easily. Therefore, this method is useful only to synthesize TMDC films on a relatively small scale.

Yang and co-workers [20] proposed a solution engineering that can easily control the wetting of precursors in the solution with the substrate. The DMF-based $(NH_4)_2MoS_4$ solution is reformulated additionally with two types of amino alcohol-based solvents. Before the spin coating, an oxygen plasma surface treatment is applied to increase the wettability of the precursor solution with the substrate. The quality of the spin-coated precursor film is gradually improved owing to the additive solvent (Fig. 1-2 b, left to right). During the spin coating of the precursor, the additive solvent promotes the solvation of

$(NH_4)_2MoS_4$ with balanced viscosity and surface tension. An optimized solvent mixture of DMF: n-butylamine: 2-aminoethanol = 4.5:4.5:1 (v/v/v, where v represents volume) generates a uniform spin-coating of the precursor, without pinholes or dewetted regions. Ionescu and co-workers [31] reported a spin coating technique, wherein the $(NH_4)_2MoS_4$ precursor is dissolved into a dimethyl sulfoxide (DMSO):ethylenediaminetetraacetic acid (EDTA) co-solvent. During the spin coating, the DMSO increases the wettability between the $(NH_4)_2MoS_4$ precursor and SiO_2 substrate, and EDTA stabilizes the precursor by chelation. Another method of improving the synthetic area of the MoS_2 thin film is the polymer-assisted precursor deposition technique, which was engineered by Yang and co-workers [21]. A linear polymer matrix (poly ethyleneimine, PEI) (Fig. 1-2 c) allows the viscosity modulation of $(NH_4)_2MoS_4$ precursor with full coverage of the spin-coated MoS_2 on a 6-inch SiO_2/Si wafer (Fig 1-2 d). The film thickness can be tuned by adjusting the concentration of the $(NH_4)_2MoS_4$ precursor.

Although the solution-engineered precursor deposition method increases the film area, this method has several drawbacks, such as low production yield, differences in the crystal growth depending on the substrate, and high production cost. Owing to these limitations, Lim and co-workers [32] developed a synthetic method of producing 20-inch-scale MoS_2 thin films using a roll-to-roll process (Fig 1-2 e). They suggested that spray coating of the $(NH_4)_2MoS_4$ precursor on a Ni foil can improve the production yield and crystallinity [33]. The

precursor deposited film is heated in a furnace at 800 °C under Ar or H_2 atmosphere to thermally decompose the $(NH_4)_2MoS_4$ precursor. This method significantly increases the production of the MoS_2 thin films on a large scale. A high yield can be achieved by controlling the various process parameters.

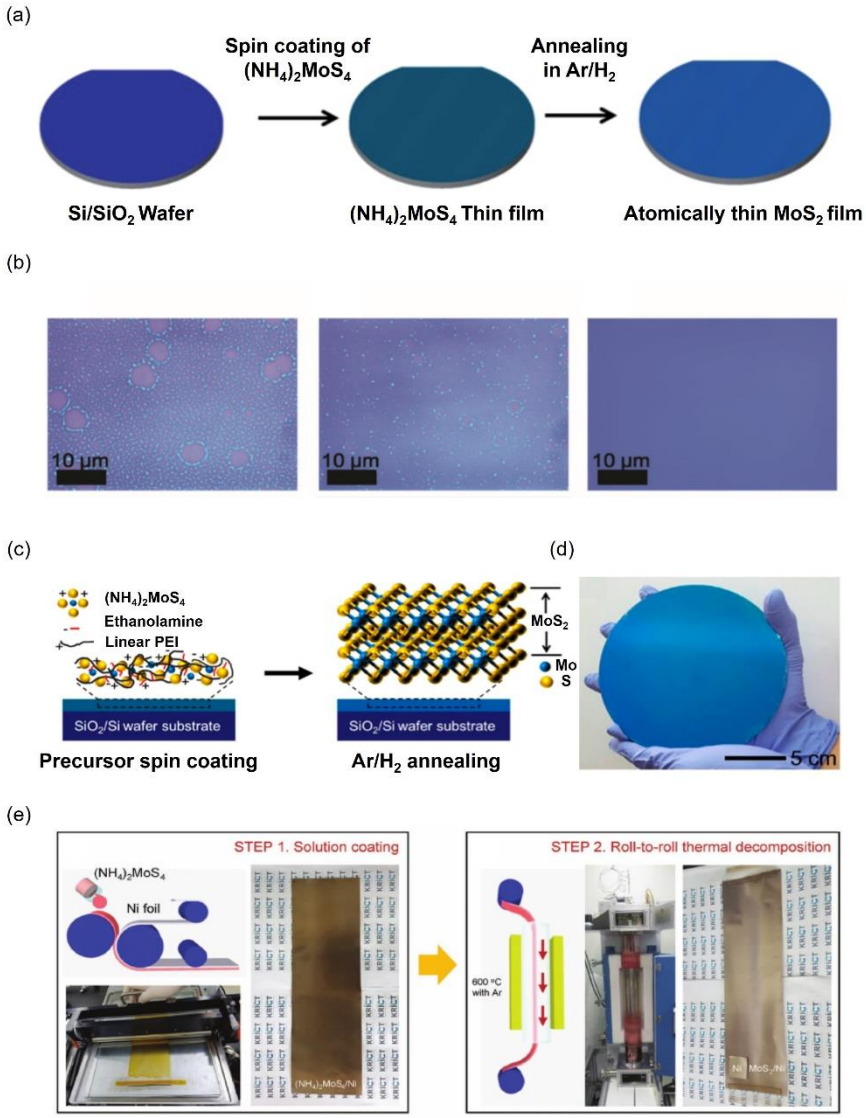

Figure 1-2. (a) Schematic representation of spin coating based 4 inch scaled MoS_2 thin-film synthesis. (Reprinted with permission from A.S. Gergo et al., Adv. Funct. Mater. 24, 7461-7466 (2014), © 2020, John Wiley and Sons [30]). (b) Optical microscope images of the spin coated $(NH_4)_2[MoS_4]$ films using different compositions of the solvent. (Reprinted with permission from Yang et al., Nanoscale 7, 9311-9319 (2015), © 2020, Royal Society of Chemistry [20]). (c), (d) Schematic diagram of the polymer-assisted spin coated $(NH_4)_2[MoS_4]$ film and its thermal decomposition on a 6-inch scaled SiO_2/Si wafer. (Reprinted with permission from Yang et al., Chem. Mater. 29, 5772-5776 (2017), © 2020, American Chemical Society [21]). (e) Schematic illustration and photographs of the roll-to-roll based 20-inch scaled MoS_2 thin-film synthesis: solution coating and thermal decomposition. (Reprinted with permission from Y. Lim et al., Adv. Mater. 30, 1705270 (2018), © 2020, John Wiley and Sons [32]).

1.2.4. Synthesis of direct-patterned TMDC films

To use a TMDC thin film in a practical electronic device, the fabricated film should be isolated to form a source–drain array. Therefore, a TMDC pattern is typically fabricated via the additional photolithography or oxygen plasma treatment-based mask process. To simplify this process, the precursor deposition and synthesis methods have been developed to form TMDC patterns directly, without the additional patterning step. Lee and co-workers [34] demonstrated the direct pattern formation in the TMDC precursor film through a dip coating method for the synthesis of WS_2 or MoS_2 wires. In this process, a piece of SiO_2, Si, or quartz wafer is soaked in $(NH_4)_2MoS_4$ (or ammonium tetrathiotungstate, $(NH_4)_2WS_4$) solution in de-ionized water. Next, the SiO_2, Si, or quartz wafer is lifted in the upward direction, and the precursor is

precipitated simultaneously in the form of a periodic wire. This method can yield both homostructured WS_2–MoS_2 wires and WS_2/MoS_2 heterostructured wires, under optimized parameters, such as proper pH and concentration of the aqueous precursor, required humidity and evaporation speed in the environment. The addition of isopropyl alcohol can tune the solvent's evaporation speed, thereby modulating the thickness of the precipitated precursor layer.

Later, Lee and co-workers [22] developed cross-aligned WSe_2/MoS_2 heterostructures through partial pinning of the solution to the substrate, which generates a regular and repetitive circular convection flow, i.e., Marangoni flow, during the precursor feeding (Fig. 1-3 a). The precursor nuclei in the solution continuously adhere to the SiO_2/Si substrate; therefore, vertically (directionally) heterostructured TMDC wires can be precipitated (Fig. 1-3 b, c). Such a direct method to form precursor patterns is useful to fabricate a specific heterojunction or to form patterns on a single material without using an additional patterning process. The fabricated cross-aligned wires show different cross-angles of 45° and 90°; this arrangement is advantageous for producing stacked TMDCs to develop integrated electronic devices (Fig. 1-3 d, e).

Park and co-workers [23] have recently developed a novel process that can freely form TMDC patterns through a pulsed laser annealing method. Using the precursor deposition method of Yang and co-workers [20], a precursor is initially deposited on a 4-inch TMDC thin film by spin coating. Next, a pulsed-laser source of wavelength 1.06 μm is irradiated on the precursor to achieve

photothermolysis (Fig. 1-3 f, g). As a result, a fine WS_2 or MoS_2 homostructure is formed with a WS_2 or MoS_2 vertical heterostructure pattern. This method allows the synthesis of a large-area patterned TMDC film only with a single-step heat treatment at room temperature and pressure in a shortened process time. Further, the fabrication is accomplished without the additional processes by easily blocking the external oxygen in a chalcogen gas (S, Se) rich atmosphere, wherein the gas is derived from the TMDC precursor. Details on the aforementioned synthesis methods are summarized in Fig. 1-T1.

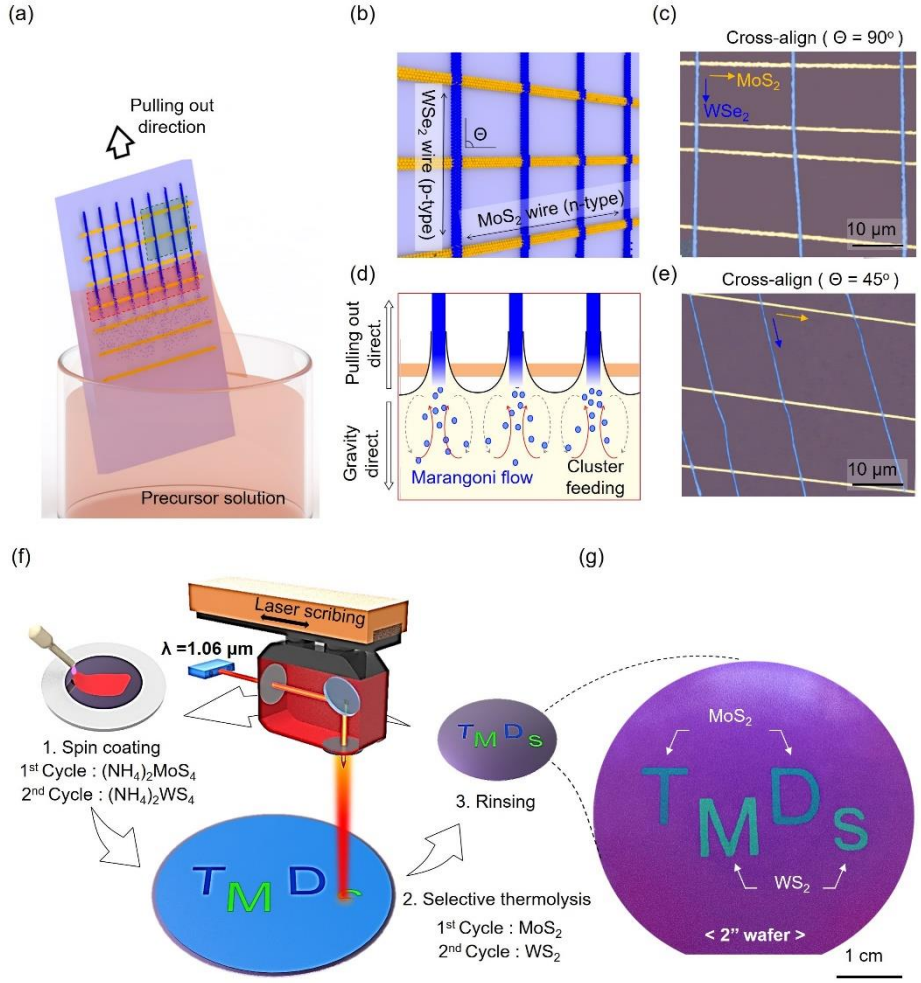

Figure 1-3. (a) Schematic diagram representing the synthesis of self-assembled WSe_2/MoS_2 wires. (b), (c) Image of cross-aligned WSe_2/ MoS_2 wires showing their growth directions. (d), (e) Optical microscopy images of different angles of WSe_2/MoS_2 wires: 90° and 45°. (Reprinted with permission from Lee et al., Adv. Mater. 31, 1904194 (2019), © 2020, John Wiley and Sons [22]). (f) Illustration of MoS_2 and WS_2 pattern formation, including spin coating, photothermal decomposition, and rinsing. (g) Photograph of the patterned MoS_2 and WS_2 supported on a 2-inch SiO_2/Si wafer. (Reprinted with

permission from Park et al., ACS Nano 14, 8485-8494 (2020), © 2020, American Chemical Society [23]).

Precursor Deposition	Precursor Solution	Annealing Method	Synthetic Area	Heterostructure	Reference
Dip coating (full cover)	DMF	Thermolysis (furnace)	1 × 1 cm^2	X	27.
Spin coating (full cover)	NMP	Thermolysis (furnace)	2 inch	X	30.
Spin coating (full cover)	DMF+ Additive	Thermolysis (furnace)	2 inch	X	20.
Spin coating (full cover)	DMF+DMSO	Thermolysis (furnace)	4 inch	X	31.
Spin coating (full cover)	DMF+PEI	Thermolysis (furnace)	6 inch	X	21.
Roll-to-Roll (full cover)	ethylene glycol	Thermolysis (furnace)	20 inch	X	32.
Dip coating (pattern)	DI water	Thermolysis (furnace)	1 × 1 cm^2	O	34.
Dip coating (pattern)	DMF	Thermolysis (furnace)	1 × 1 cm^2	O	22.
Spin coating (full cover)	DMF+Additive	Locally Thermolysis (pulsed laser)	4 inch	O	23.

Figure 1-T1. Comparison between the different of solution-processed TMDC thin film synthesis.

1.3. Applications of TMDCs

TMDC thin films obtained from a solution (e.g., MoS_2, WS_2, WSe_2) can be synthesized on a large scale using simple thermal decomposition processes and therefore have a variety of applications in electronic devices. In this section, we review the electronic devices and sensors that have been developed by using the solution-based synthesis methods.

1.3.1 Field-effect transistors (FETs)

One of the key characteristics of a TMDC thin film is its semiconducting property. A TMDC thin film has a tunable band gap depending on the number of its layers [35, 36]. Liu and co-workers [27] first reported the fabrication of an FET from the solution-based thermally decomposed MoS_2 thin films. The synthesized triple layered MoS_2 film has the property of n-type behavior and shows good field-effect electron mobility (4.7 $cm^2 V^{-1}s^{-1}$). The variation of the electron mobility, depending on the number of layers of the solution-synthesized MoS_2 film, is systemically investigated by Lee and co-workers [34]. Fig. 1-4 a shows a comparison of the transfer curves (I_{DS} *vs* V_{GS}) associated with the thickness modulation of the ion-gel gated MoS_2 wires. The transfer characteristics show that the current increases with increasing thickness of the wires (3 to 32 nm). In the case of a thick MoS_2 wire (32 nm) exhibits symmetric ambipolar behavior, indicating that enhanced electron and Hole mobility was observed. Fig. 1-4 b shows the variation of the mobility with the MoS_2 film

thickness. The statistically evaluated average effective mobility is approximately 100 $cm^2 V^{-1}s^{-1}$, as observed from Fig. 1-4 b. These results are due to the fact that, as the thickness of the MoS_2 films increase, their vulnerability to carrier scattering decreases, which in turn increases their carrier mobility [37, 38]. Several solution-synthesized MoS_2 thin films have been applied to FETs. However, they have low average effective carrier mobility, [20, 31] and are therefore not suitable for commercialization. The performance of the solution-processed MoS_2 FETs are summarized in Fig. 1-T2.

1.3.2 Photodetectors

Shifting the perspective to the optoelectronic properties of the solution-based MoS_2 thin films, Lim and co-workers [33] developed a thermally decomposed MoS_2-based visible light photodetector on a 4-inch SiO_2/Si wafer. They focused on the spatial distribution of the large-scale MoS_2 thin film with 100 devices (10 rows × 10 columns). The result of the homogeneous photoresponse is displayed in Fig. 1-4 e, which indicates that the device yielded a periodically varying photocurrent under a halogen lamp irradiation with a tunable power, regardless of the bias voltages (1, 5, 10, 15, and 20 V). For a fixed photocurrent at a bias voltage of 20 V, the illumination power increases from 7.0 to 12.5 mW cm^{-2}; this observation implies that the photocurrent is proportional to the illumination power, owing to an increase in the carrier-generation rate. Thus, the photocurrent of a photodetector is linearly dependent

on the illumination power.

Furthermore, Lee and co-workers [22] recently demonstrated a solution-based cross-aligned Wse_2/ MoS_2 *p-n* junction structured photodiode and detector. The analyzed photo responsivity of the fabricated device is ~5.39 A W^{-1}, which is higher than that of the previously reported TMDC-based optoelectronic devices that are made up of monolayer homo- and heterojunctions. Park and co-workers [23] demonstrated a *p-n* diode with vertically stacked solution-processed WS_2/MoS_2 thin films prepared by irradiating $(NH_4)_2WS_4/MoS_2$ films with an ultra-short laser pulse (~100 ps) to cause selective thermolysis of $(NH_4)_2WS_4$, since it shows ~60 times higher absorbance than the MoS_2 film during the laser annealing (1.06 μm). The process converts $(NH_4)_2WS_4$ to a WS_2 film with high crystallinity despite the instant formatting on the MoS_2 lattice. This *p-n* diode that uses WS_2/MoS_2 produces good electrical rectification with a forward-to-reverse current ratio of ~10^3.

1.3.3 Hydrogen evolution reactor (HER)

Another solution-based TMDC application has attracted considerable attention in the field of catalysis. Deng and co-workers [39] developed hydrogen evolution reaction (HER) catalysts from the one-step photothermal decomposition of PI and MoS_2 precursor by using a continuous-wave laser to ensure strong heating. The laser-irradiated sample must include a composite of

laser-induced graphene and MoS_2 nanoparticles; the composite significantly influences the HER activity by increasing the specific area and producing heat-induced surface defects. The results of the linear sweep voltammetry measurements, showing the polarization curves of bulk MoS_2, hydrothermal MoS_2, MoS_2/carbon hybrids, and Pt/ carbon, are shown in Fig. 1-4 e. The MoS_2/carbon hybrids exhibit a higher overpotential (216 mV) and a lower Tafel slope (64 mV dec^{-1}) than other samples (Fig. 1-4 f). Hasani and co-workers [40] demonstrated a solar-driven HER sensor having a heterojunction formed by thermally decomposed n-type MoS_2 on a p-type Si. This sensor shows the highest catalytic activity with the lowest Tafel slope of 65 mV dec^{-1}, when an appropriate MoS_2 thin-film thickness (16.8 nm) is used.

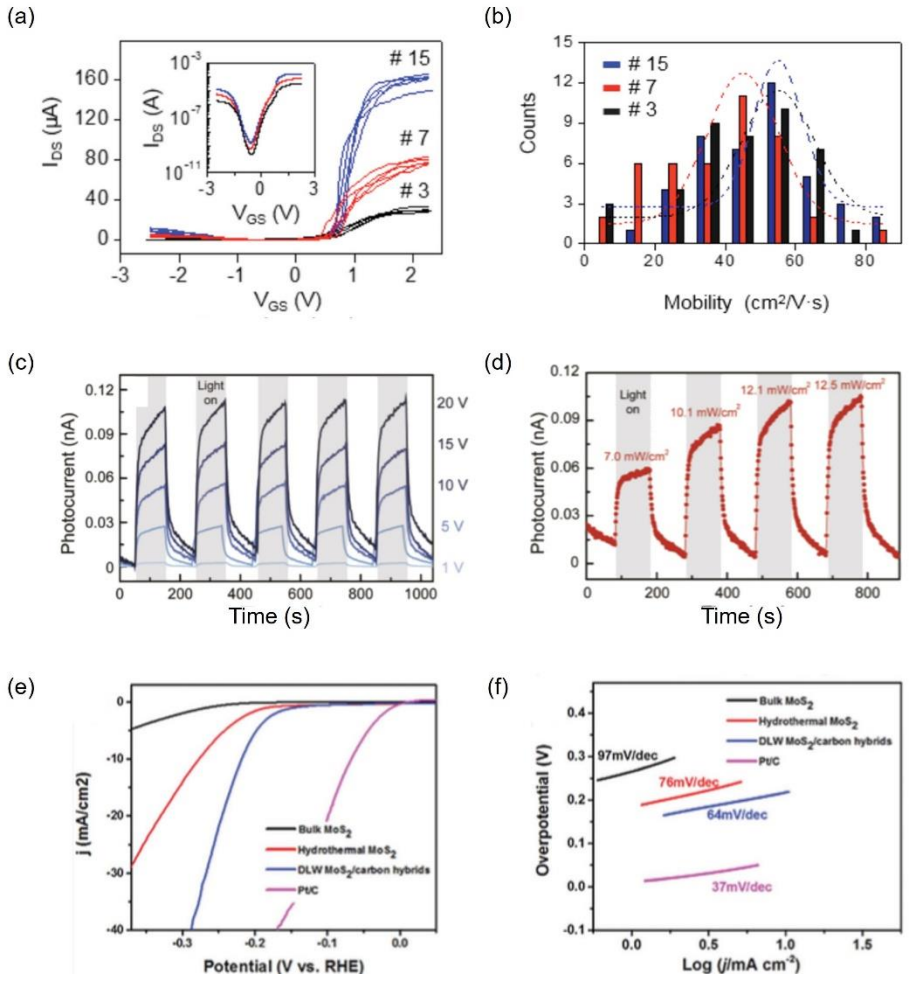

Figure 1-4. (a), (b) Transfer curves (I_{DS} *vs* V_{GS}) of the ion-gel gated MoS_2/graphene hybrid FETs, depending on the thickness of the wires in the channel and their effective charge mobility. (Reprinted with permission from Lee et al., Adv. Mater. 27, 4142-4149 (2015), © 2020, John Wiley and Sons [34]). (c), (d) Time-resolved photocurrent response of the thermally decomposed MoS_2 on PI film (Reprinted with permission from Y. Lim et al., Adv. Mater. 28, 5025-5030 (2016), © 2020, John Wiley and Sons [33]). (e), (f) Polarization curves of a series of samples: Pt/C, bulk MoS_2, hydrothermal MoS_2, and

photothermally decomposed MoS_2. (Reprinted with permission from Deng et al., J. Mater. Chem. A. 4, 6824-6830 (2016), © Royal Society of Chemistry [39]).

Materials	Annealing Method	On/ Off Ratio	Mobility ($cm^2 V^{-1}s^{-1}$).	Directly Patterning	Reference
MoS_2	Thermolysis (furnace)	~10^5	~4.7	X	27.
MoS_2 WS_2	Thermolysis (furnace)	~10^6	~100	O	34.
MoS_2	Thermolysis (furnace)	~10^4	~0.24	X	20.
MoS_2	Thermolysis (furnace)	~10^8	~0.1	X	31.
MoS_2 WS_2	Locally Thermolysis (pulsed laser)	~10^3	~6.4	O	23.

Figure 1-T2. Comparison of the performance of the FETs, produced by solution based-TMDC synthesis.

1. 3. 4. Strain and haptic sensors

The previously reported methods of TMDC-based strain sensor fabrication used thin films grown using CVD, with several subsequent photolithography steps to pattern the strain gauge [41, 42]. Park and co-workers [23] demonstrated the direct pattern formation of a MoS_2-based strain gauge and proposed that a lithography-free approach can be applied to develop a three-

axis strain gauge rosette. The application of an external force on the MoS_2 strain gauge causes strain-induced deformation of the conductive pathways, which changes the electrical conductivity of the material (Fig. 1-5 a). Notably, the relationship between the conductivity and strain is linear, and the gauge operates reversibly, without hysteresis, at a strain < 1.67%. Therefore, the range of the strain is restricted to the linear regime (≈ 1.5%), and the mechanical response of the strain gauge shows a stable response over 1000 repeated cycles (Fig. 1-5 b). When mounted on a human wrist, this three-axis strain gauge rosette can simultaneously respond in unknown X^o and Y^o directions (Fig. 1-5 c). The time-resolved resistance response of the rosette shows an omnidirectional sensing ability.

Direct-pattern formation by photothermal decomposition is used to fabricate self-powering haptic sensors that use a MoS_2 active layer. Park and co-workers [24] fabricated large-scale patterned MoS_2 thin films and developed strain induced crumpled MoS_2. The crumpled MoS_2 has distinct characteristics compared to the pristine MoS_2. A widening in the MoS_2 lattice and a decrease in the orbital overlap increase the work function of the sensor; these changes increase the charge-transfer effect during the generation of self-powering signal, i.e., the triboelectric current generation. Hence, the haptic sensor is self-powered and includes a triboelectric touchpad on a latex glove. The 4 × 4 arrayed, crumpled MoS_2 haptic touch sensor has a time-dependent mapping trajectory, according to the movement of a stylus (Fig. 1-5 d).

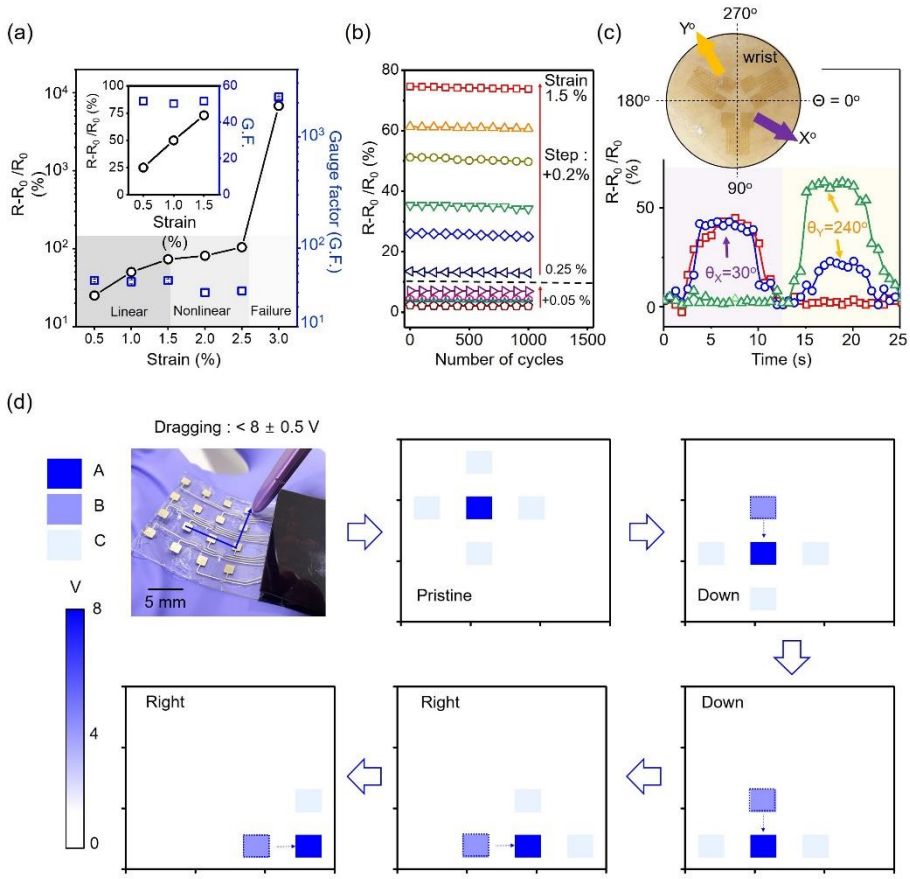

Figure 1-5. (a) Relative resistance variation and gauge factor of the MoS_2-based strain gauge in the range of 0.5–3.0%. (b) Mechanical stability of MoS_2-based strain gauge up to 1000 cycles with different strain levels. (c) Operation of the MoS_2-based 3-axis strain gauge rosette with sensing ability from unknown directions. (Reprinted with permission from Park et al., ACS Nano 14, 8485-8494 (2020), © 2020, American Chemical Society [23]). (d) Time-resolved trajectory mapping of the MoS_2-based haptic sensor using a stylus pen movement. (Reprinted with permission from Park et al., Nano Energy 78, 105266 (2020), © 2020, American Chemical Society [24]).

1. 4. Perspectives and Summary

This thesis covers a wide range of large-scale, inexpensive, and simple methods for synthesizing TMDC thin films from solutions with direct-pattern formation, in addition to elucidating their practical applications. Various precursor deposition methods have been developed to increase the film area and modulate the solution composition, which yields the appropriate coating conditions for large-scale fabrication. Thus, the thickness of the TMDC film is easily modulated by adjusting the precursor concentration. Notably, direct formation of the TMDC patterns is also achieved using the solution-phase precipitation and photothermal decomposition. These processes yield vertically stacked TMDC-based heterostructures, without complex processing steps. The synthesis of TMDCs from solutions can be practically applied to readily fabricate devices, such as FETs, photodetectors, HER catalysts, diodes, and mechanical sensors.

However, the TMDC thin film synthesis method covered in this review is still problematic to be applied to high performance electronic devices because of the small TMDC grain size. Therefore, the development of another methodology for the mass production of highly crystallinity of TMDC thin films is crucial for their applications in the semiconductor industry and researches.

1. 5. References

1. Y. Kim, S. S. Cruz, K. Lee, B. O. Alawode, C. Choi, Y. Song, J. M. Johnson, C. Heidelberger, W. Kong, and S. Choi, Nature 544, 340 (2017).

2. H. Schmidt, S. Wang, L. Chu, M. Toh, R. Kumar, W. Zhao, A. H. Neto, J. Martin, S. Adam, B. Ozyilmaz, and G. Eda, Nano. Lett. 14, 1909 (2014).

3. N. Perea-López, A. L. Elías, A. Berkdemir, A. Castro-Beltran, H. R. Gutiérrez, S. Feng, R. Lv, T. Hayashi, F. López-Urías, S. Ghosh, B. Muchharla, S. Talapatra, H. Terrones, and M. Terrones, Adv. Funct. Mater. 23, 5511 (2013).

4. S. B. Desai, S. R. Madhvapathy, A. B. Sachid, J. P. Llinas, Q. Wang, G. H. Ahn, G. Pitner, M. J. Kim, J. Bokor, and C. Hu, Science 354, 99 (2016).

5. S. Bae, H. Kim, Y. Lee, X. Xu, J.-S. Park, Y. Zheng, J. Balakrishnan, T. Lei, H. R. Kim, and Y. I. Song, Nat. Nanotechnol. 5, 574 (2010).

6. T. Kobayashi, M. Bando, N. Kimura, K. Shimizu, K. Kadono, N. Umezu, K. Miyahara, S. Hayazaki, S. Nagai, and Y. Mizuguchi, Appl. Phys. Lett. 102, 023112 (2013).

7. J.-H. Lee, E. K. Lee, W.-J. Joo, Y. Jang, B.-S. Kim, J. Y. Lim, S.-H. Choi, S. J. Ahn, J. R. Ahn, and M.-H. Park, Science 344, 286 (2014).

8. A. K. Geim and I. V. Grigorieva, Nature 499, 419 (2013).

9. S. Tongay, J. Zhou, C. Ataca, K. Lo, T. S. Matthews, J. Li, J. C. Grossman, and J. Wu, Nano Lett. 12, 5576 (2012).

10. G. Iannaccone, F. Bonaccorso, L. Colombo, and G. Fiori, Nat. Nanotechnol. 13, 183 (2018).

11. J. Yoon, W. Park, G. Y. Bae, Y. Kim, H. S. Jang, Y. Hyun, S. K. Lim, Y. H.

Kahng, W. K. Hong, and B. H. Lee, Small 9, 3295 (2013).

12. J. Pu, Y. Yomogida, K. K. Liu, L. J. Li, Y. Iwasa, and T. Takenobu, Nano Lett. 12, 4013 (2012).

13. H. Yu, M. Liao, W. Zhao, G. Liu, X. J. Zhou, Z. Wei, X. Xu, K. Liu, Z. Hu, K. Deng, S. Zhou, J. A. Shi, L. Gu, C. Shen, T. Zhang, L. Du, L. Xie, J. Zhu, W. Chen, R. Yang, D. Shi, and G. Zhang, ACS Nano 11, 12001 (2017).

14. Y. Kim, A. R. Kim, G. Zhao, S. Y. Choi, S. C. Kang, S. K. Lim, K. E. Lee, J. Park, B. H. Lee, M. G. Hahm, D. H. Kim, J. Yun, K. H. Lee, and B. Cho, ACS Appl. Mater. Inter. 9, 37146 (2017).

15. Y. Xue, Y. Zhang, Y. Liu, H. Liu, J. Song, J. Sophia, J. Liu, Z. Xu, Q. Xu, Z. Wang, J. Zheng, Y. Liu, S. Li, and Q. Bao, ACS Nano 10, 573 (2016).

16. N. Choudhary, J. Park, J. Y. Hwang, H. S. Chung, K. H. Dumas, S. I. Khondaker, W. Choi, and Y. Jung, Sci. Rep. 6, 25456 (2016).

17. A. Pant, Z. Mutlu, D. Wickramaratne, H. Cai, R. K. Lake, C. Ozkan, and S. Tongay, Nanoscale 8, 3870 (2016).

18. A. Giri, G. Park, H. Yang, M. Pal, J. Kwak, and U. Jeong, Adv. Mater. 30, 1707577 (2018).

19. C. Ahn, J. Lee, H. U. Kim, H. Bark, M. Jeon, G. H. Ryu, Z. Lee, G. Y. Yeom, K. Kim, J. Jung, Y. Kim, C. Lee, and T. Kim, Adv. Mater. 27, 5223 (2015).

20. J. Yang, Y. Gu, E. Lee, H. Lee, S. H. Park, M. H. Cho, Y. H. Kim, Y. H. Kim, and H. Kim, Nanoscale 7, 9311 (2015).

21. H. Yang, A. Giri, S. Moon, S. Shin, J.-M. Myoung, and U. Jeong, Chem. Mater. 29, 5772 (2017).

22. J. B. Lee, Y. R. Lim, A. K. Katiyar, W. Song, J. Lim, S. Bae, T. W. Kim, S. K. Lee, and J. H. Ahn, Adv. Mater. 31, e1904194 (2019).

23. S. Park, A. Lee, K. H. Choi, S. K. Hyeong, S. Bae, J. M. Hong, T. W. Kim, B. H. Hong, and S. K. Lee, ACS Nano 14, 8485 (2020).

24. S. Park, J. Park, Y.-g. Kim, S. Bae, T.-W. Kim, K.-I. Park, B. H. Hong, C. K. Jeong, and S.-K. Lee, Nano Energy 78, 105266 (2020).

25. S. J. Hibble and M. R. Feaviour, J. Mater. Chem. 11, 2607 (2001).

26. N. Kondekar, M. G. Boebinger, M. Tian, M. H. Kirmani, and M. T. McDowell, ACS Nano 13, 7117 (2019).

27. K. K. Liu, W. Zhang, Y. H. Lee, Y. C. Lin, M. T. Chang, C. Y. Su, C. S. Chang, H. Li, Y. Shi, H. Zhang, C. S. Lai, and L. J. Li, Nano Lett. 12, 1538 (2012).

28. J. G. Kim, W. S. Yun, S. Jo, J. Lee, and C. H. Cho, Sci. Rep. 6, 29813 (2016).

29. L. Liang and V. Meunier, Nanoscale 6, 5394 (2014).

30. A. S. George, Z. Mutlu, R. Ionescu, R. J. Wu, J. S. Jeong, H. H. Bay, Y. Chai, K. A. Mkhoyan, M. Ozkan, and C. S. Ozkan, Adv. Funct. Mater. 24, 7461 (2014).

31. R. Ionescu, B. Campbell, R. Wu, E. Aytan, A. Patalano, I. Ruiz, S. W. Howell, A. E. McDonald, T. E. Beechem, K. A. Mkhoyan, M. Ozkan, and C. S. Ozkan, Sci. Rep. 7, 6419 (2017).

32. Y. R. Lim, J. K. Han, S. K. Kim, Y. B. Lee, Y. Yoon, S. J. Kim, B. K. Min, Y. Kim, C. Jeon, S. Won, J. H. Kim, W. Song, S. Myung, S. S. Lee, K. S. An, and J. Lim, Adv. Mater. 30, 1705270 (2018).

33. Y. R. Lim, W. Song, J. K. Han, Y. B. Lee, S. J. Kim, S. Myung, S. S. Lee, K. S. An, C. J. Choi, and J. Lim, Adv. Mater. 28, 5025 (2016).

34. S. K. Lee, J. B. Lee, J. Singh, K. Rana, and J. H. Ahn, Adv. Mater. 27, 4142 (2015).

35. J. Zhu, J. Wu, Y. Sun, J. Huang, Y. Xia, H. Wang, H. Wang, Y. Wang, Q. Yi, and G. Zou, RSC Adv. 6, 110604 (2016).

36. A. Ebnonnasir, B. Narayanan, S. Kodambaka, and C. V. Ciobanu, Appl. Phys. Lett. 105, 031603 (2014).

37. S. L. Li, K. Wakabayashi, Y. Xu, S. Nakaharai, K. Komatsu, W. W. Li, Y. F. Lin, A. Aparecido-Ferreira, and K. Tsukagoshi, Nano Lett. 13, 3546 (2013).

38. J. Na, M. Shin, M.-K. Joo, J. Huh, Y. J. Kim, H. J. Choi, J. H. Shim, and G.-T. Kim, Appl. Phys. Lett. 104, 062901 (2014).

39. H. Deng, C. Zhang, Y. Xie, T. Tumlin, L. Giri, S. P. Karna, and J. Lin, J. Mater. Chem. A 4, 6824 (2016).

40. A. Hasani, Q. V. Le, M. Tekalgne, M.-J. Choi, T. H. Lee, H. W. Jang, and S. Y. Kim, NPG Asia Mater. 11, 1 (2019).

41. M. Park, Y. J. Park, X. Chen, Y. K. Park, M. S. Kim, and J. H. Ahn, Adv. Mater. 28, 2556 (2016).

42. Y. J. Park, B. K. Sharma, S. M. Shinde, M. S. Kim, B. Jang, J. H. Kim, and J. H. Ahn, ACS Nano 13, 3023 (2019).

43. Z. Huang, W. Luo, L. Ma, M. Yu, X. Ren, M. He, S. Polen, K. Click, B. Garrett, J. Lu, K. Amine, C. Hadad, W. Chen, A. Asthagiri, and Y. Wu, Angew. Chem. Int. Ed. Engl. 54, 15181 (2015).

44. T. Zhang, L. B. Kong, Y. H. Dai, K. Yan, M. Shi, M. C. Liu, Y. C. Luo, and L. Kang, Chem. Asian J. 11, 2392 (2016).

Chapter 2.

Layer-Selective Synthesis of MoS_2 and WS_2 Structures under Ambient Conditions for Customized Electronics

[*The contents of this chapter is reproduced from: Seoungwoong Park, Aram Lee, Kwang-Hun Choi, Seok-Ki Hyeong, Sukang Bae, Jae-Min Hong, Tae-Wook Kim, Byung Hee Hong*, and Seoung-Ki Lee* *ACS Nano* (2020) 14, 8485-8494. © 2020 American Chemical Society]

2. 1. Abstract

Transition metal dichalcogenides (TMDs) have attracted significant interest as one of the key materials in future electronics such as logic devices, optoelectrical devices, and wearable electronics. However, a complicated synthesis method and multistep processes for device fabrication pose major hurdles for their practical applications. Here, we introduce a direct and rapid method for layer-selective synthesis of MoS_2 and WS_2 structures in wafer-scale using a pulsed laser annealing system (λ = 1.06 μm, pulse duration ~ 100 ps) in ambient conditions. The precursor layer of each TMD, which has at least 3 orders of magnitude higher absorption coefficient than those of neighboring layers, rigorously absorbed the incoming energy of the laser pulse and rapidly pyrolyzed in a few nanoseconds, enabling the generation of a MoS_2 or WS_2 layer without damaging the adjacent layers of SiO_2 or polymer substrate. Through experimental and theoretical studies, we establish the underlying

principles of selective synthesis and optimize the laser annealing conditions, such as laser wavelength, output power, and scribing speed, under ambient condition. As a result, individual homostructures of patterned MoS_2 and WS_2 layers were directly synthesized on a 4 in. wafer. Moreover, a consecutive synthesis of the second layer on top of the first synthesized layer realized a vertically stacked WS_2/MoS_2 heterojunction structure, which can be treated as a cornerstone of electronic devices. As a proof of concept, we demonstrated the behavior of a MoS_2-based field-effect transistor, a skin-attachable motion sensor, and a MoS_2/WS_2-based heterojunction diode in this study. The ultrafast and selective synthesis of the TMDs suggests an approach to the large-area/mass production of functional heterostructure-based electronics.

2. 2. Introduction

Transition metal dichalcogenides (TMDs) have garnered plenty of attention, and high expectations have been raised in both the fundamental research field as well as industry due to their distinctive electronic and optical properties originating from two-dimensional (2D) quantum confinement [1]. Over the past decades, significant investigations on TMDs have shown impressive potential applications in sensors, logic devices, and optoelectronics, meeting expectations.[2-4] As the functions that can be implemented with TMDs become concrete, synthesizing materials in a more effective manner to produce practical electronics has become important. Pioneering improvements have

been achieved based on chemical vapor deposition (CVD). Since the first synthesis of single-crystalline graphene, in spite of the 2D crystals with biatom-based honeycomb lattice structure, wafer-scale fabrication MoS_2 and h-BN could have been achieved [5-8]. Recently, several routes for forming vertically or horizontally layered heterostructures (*e.g.*, MoS_2/BN, MoS_2/WS_2, and WS_2/WSe_2) through a modified CVD approach were reported [9, 10], and these structures worked as versatile Schottky junctions and *p*-*n* junctions, showing clear rectification, photoresponse, and photovoltaic action. However, despite remarkable achievements in material preparation, the practical applications have been delayed due to several limitations of CVD. First, generating TMD-based heterostructures with clean sharp interfaces without chemical complexes is still challenging due to the difficulty of selective control of the heat distribution. Second, an additional patterning process after synthesis of the film is essential. Current patterning techniques, including lithography and plasma etching, require a protective layer to define the desired pattern, which not only inevitably causes contamination but also increases the device fabrication complexity. These separated fabrication steps (synthesis → patterning) negate some of the advantages of CVD, delaying real applications. Although a few attempts aiming at patterned synthesis of TMD-based heterostructures using substrate treatment, patterned precursors, and self-assembly methods have been reported, these approaches are used in conjunction with complicated pretreatment steps in a vacuum chamber, and implementing a clear pattern at a

precise location over a large area with reproducibility is still difficult [11-13].

In this paper, we introduce a strategy for the direct synthesis of patterned MoS_2 and WS_2 structures by driving layer-selective thermolysis *via* laser beam annealing. By means of the atomic-scale modulation of temperature through the depth of pre-synthesis structure, the target precursor layer was selectively and effectively converted into MoS_2 from the $(NH_4)_2MoS_4$. The instant laser-based local treatment enabled the generation of a patterned MoS_2 structure on a 4-inch wafer within several minutes under ambient conditions without damaging the substrate, dramatically reducing the process time. Moreover, we succeeded in the selective synthesis of WS_2 layer on a MoS_2 layer and accordingly generated a WS_2/MoS_2 heterostructure with a sharp and clean junction interface. We performed a combined experimental and theoretical study to elucidate the mechanism of selective synthesis and to optimize the laser annealing conditions such as laser wavelength, output power, and scribing speed. The direct formation of high-quality patterned TMDs under ambient conditions effectively reduced the process steps, cost, and time for device fabrication. Furthermore, the versatility of patterned TMDs was proven through functional devices such as rectifiers, transistors, and strain sensors.

2. 3. Experimental

Spin-coating of precursors on SiO_2/Si wafer: Highly *p*-doped SiO_2/Si wafer (dielectric layer 300 nm) is immersed into a cleaning solution (ethyl alcohol for 10 min and deionized water for 10 min) and O_2 plasma-treated at 100 W for 100 s to increase the hydrophilicity of the substrate and enhance the coating adhesion. Aqueous type precursors were separately prepared by dissolving each of $(NH_4)_2MoS_4$ (Sigma-Aldrich, CAS No. 15060-55-6) and $(NH_4)_2WS_4$ (Alfa Aesar, CAS No. 13862-78-7) in DMF (n-butylamine : 2-aminoethanol = 5:2:1 (v/v/v)) and they were sonicated at 50 ºC for 30 min. Then the prepared precursors were drop-casted onto the plasma-treated wafer and consecutively spin-coated at 500 rpm for 10 s and 2500 rpm for 30 s. The residual solvents were removed by baking on hot plate at 150 ºC for 3 min.

Selective laser annealing process for MoS_2 and WS_2 based Heterostructure: The spin-coated $(NH_4)_2MoS_4$ precursor was irradiated by pulse laser (Universal laser, pulse duration ~100 ps, repetition rate 50 kHz) to thermally decompose it by the absorbed optical energy. The heat treatment area was precisely drawn *via* a preprogrammed pattern using a commercially available graphic design software (CorelDRAW Graphics Suite). After laser scribing, the precursor layer in the nontreated area was removed by DMF solvent, leaving a patterned MoS_2 film. Then the solvent of WS_2 precursor ($(NH_4)_2WS_4$ was deposited on the patterned MoS_2 film through spin-coating at 2300 rpm for 20 s and pre-baking

at 130 °C for 3 min. The WS_2 precursor/MoS_2 structure was again irradiated by the pulse laser and the top WS_2 precursor layer was selectively annealed due to its much higher optical absorbance. Finally, the untreated region of WS_2 precursor was removed by DMF solvent again.

MoS_2-based FET fabrication and electrical characterization: Source and drain electrodes (5/50 nm, Ti/Au) were thermally deposited on the laser patterned MoS_2 channel to evaluate its semiconducting property. The specifically chosen electrode helps the operation of *n*-type MoS_2 FET by formation of Ohmic-contact. Top-gated FET configuration was adopted to measure the dielectric characteristics, where an ionic liquid (1-Ethyl-3-methylimidazolium bis imide, Sigma-Aldrich, CAS No. 174899-82-2) was used as the top-gate. The sample was kept in a vacuum (~10^{-6} torr) shielded probe station (MSTECH, M5VC) and its three-probe characteristic was measured using a parameter analyzer (Keithley 4200-SCS).

Temporal monitoring of electrical resistance in rosette strain gauge: We utilized a custom-built strain test machine, which is equipped with a motorized stage to apply strain and output exact value of the resulted strain, to measure the performance of our MoS_2-based strain gauge which is transferred on a stretchable substrate (PSA, polysulfonic acid). A pair of contact pads (indium gallium eutectic, Sigma-Aldrich, 495425) was drop-casted at each end of the

strain gauge and the accordingly generated resistance variation was measured using a parameter analyzer (Keithley 4200-SCS).

2. 4. Results and discussion

Fig. 2-1 shows the strategy for selective thermolysis with the help of focused laser energy. The fabrication of patterned molybdenum disulfide (MoS_2, *n*-type) and tungsten disulfide (WS_2, *p*-type) films began with full covering of each precursor film, *i.e.*, ammonium tetrathiomolybdate ($(NH_4)_2MoS_4$) and ammonium tetrathiotungstate ($(NH_4)_2WS_4$), respectively, onto the target wafer. Dimethylformamide (DMF) was selected as the main solvent, and amine and amino alcohols were added into the precursor solution to control its surface tension and viscosity, which improved the uniformity of the film [14]. First, to synthesize patterned MoS_2, $(NH_4)_2MoS_4$ precursor was spin coated on a silicon wafer, covered with 300 nm-thick SiO_2, and annealed at 150 °C for 3 min to evaporate the residual solvents as a start of 1st cycle. $(NH_4)_2MoS_4$ requires high thermal energy (temperature > 500 °C) under inert or sulfur-rich conditions to thermally decompose into MoS_2 [15, 16]. Here, we used a pulsed fiber laser (Universal Laser, wavelength =1.06 μm, pulse width ~100 ps) to induce a local photothermal reaction, as shown in Fig. 2-1 a. The heat treatment area was precisely defined *via* a preprogrammed pattern drawn by a commercially available graphic design software (CorelDRAW Graphics Suite). After laser scanning, the precursor layer in the nontreated area was simply removed by

DMF solvent, leaving a patterned MoS_2 film ("T" and "D" text on the wafer, Fig. 2-1 b). Fig. 1c and d provides the mechanism of selective conversion of $(NH_4)_2MoS_4$ precursors into MoS_2. When the laser beam irradiated, a fraction of the laser energy was absorbed depending on the optical absorption of each material. To more deeply examine the thermodynamics, we conducted an analytical study by equating the absorbed optical energy (E_{op}) to the increase in the thermal energy (E_{th}). A commercial optical FDTD simulation tool (Lumerical FDTD) was used to numerically estimate the amount of optical energy absorbed in each layer under pulse irradiation. The required optical parameters of the materials, *e.g.*, precursor, MoS_2, and substrate, were directly measured by ellipsometry and applied to the simulation, enabling the temperature profile of each stacked layer to be obtained (Fig. 2-2 and Fig. 2-1 T1). The measured absorption coefficients ( ) of the $(NH_4)_2MoS_4$, MoS_2, and SiO_2 substrates are plotted in Fig. 2-1 d [17]. We found that the difference in the optical absorption factors between each material is a key parameter for the selective synthesis of patterned MoS_2. Notably, because of the ~10^4 times higher absorption in the precursor volume ($\alpha = 6.7 \times 10^4\ m^{-1}$) than in the SiO_2 ($\alpha \sim 1\ m^{-1}$) at wavelength of laser (λ=1.06 μm), the precursor layer was selectively self-heated to ~ 700 °C under a sub-nanosecond of pulse irradiation and converted to MoS_2 while releasing sulfur by pyrolysis. In our simulation that considered both inter- and intra-layer thermal transports through the entire geometric domain, a slight increase in the temperature of SiO_2 was observed as

well due to the consideration of heat transports from each of precursor and bulk Si substrate. However, given with the low thermal conductivity of SiO_2, such vertical thermal transports and following temperature change were highly suppressed, resulting in negligible effect on the synthesis of MoS_2. More specific time-domain simulation was described in Fig. 2-3. Importantly, once MoS_2 was synthesized, it could avoid additional energy injection by the successively incoming pulses due to its increased transparency, wherein the absorption coefficient of the MoS_2 layer ($\alpha = 1.2 \times 10^3\ m^{-1}$) is ~ 60 times lower than that of the $(NH_4)_2MoS_4$ precursor. Thus, the synthesized MoS_2 can be preserved during harsh laser-based thermal annealing. After fabricating the MoS_2, patterned WS_2 was synthesized with the same process sequence and mechanism but using a different precursor material $(NH_4)_2WS_4$) as a 2nd cycle, completing the MoS_2- and WS_2-based homostructures at room temperature and pressure (Fig. 2-4). Fig. 2-1 b shows a representative example of selectively patterned homostructure of *n*-type MoS_2 and *p*-type WS_2 on a 2-inch wafer. The quality of synthesized MoS_2 and WS_2 were characterized by Raman spectroscopy as shown in Fig. 2-1 e. For MoS_2, the in-plane stretching mode (E_{2g}) at 383 cm^{-2} and out-of-plane stretching mode (A_{1g}) at 406 cm^{-2} were identified. In addition, the WS_2 (B) exhibited two signals corresponding to the E_{2g} and A_{1g} modes at 350 and 418 cm^{-1}, respectively, suggesting the formation of a two-dimensional crystal structure. The detailed description of pulsed laser simulation and synthetic procedure were followed below (Fig. 2-2 – Fig. 2-5).

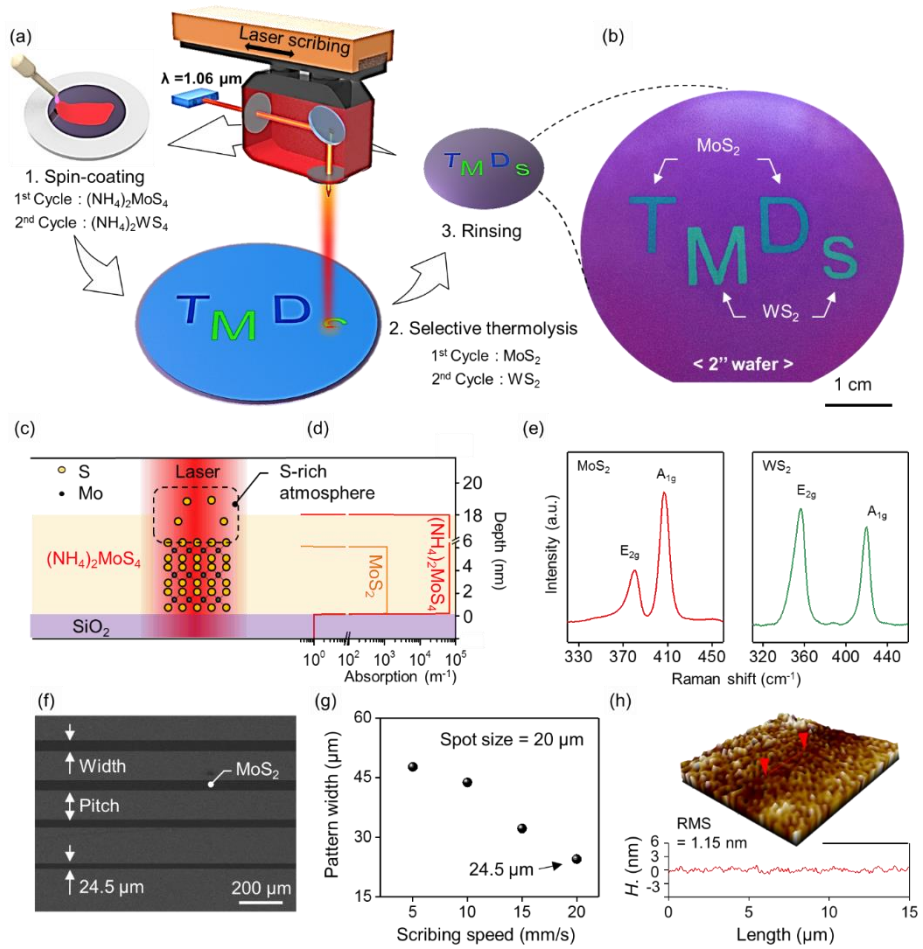

Figure 2-1. Layer-selective syntheses of homostructure MoS_2 and WS_2. (a) Schematic illustration of selective synthesis: MoS_2- and WS_2-based homostructures. (b) Photograph of patterned MoS_2 and WS_2 on 2-inch SiO_2/Si substrate. (c, d) Synthesis mechanism of MoS_2 and absorption coefficient profile of each layer. (e) Raman spectra of synthesized MoS_2 and WS_2. (f) SEM image of line-patterned MoS_2 with difference scribing speeds. (g) Pattern width and pitch variation as a function of scribing speed. (h) Three-dimensional surface morphology of MoS_2.

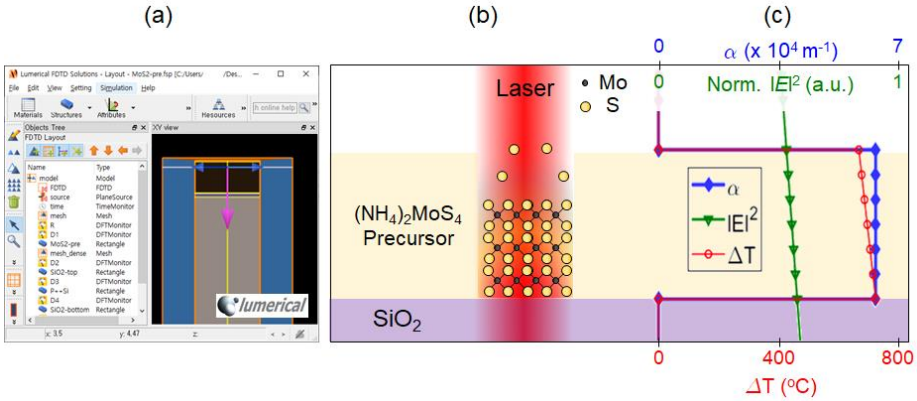

Figure 2-2. (a) GUI control panel of Lumerical FDTD optical simulation. (b) Illustration of laser-induced synthesis of MoS_2 homostructure. (c) Profiles of absorption coefficient and electric fields under a pulse irradiation and estimation of temperature change.

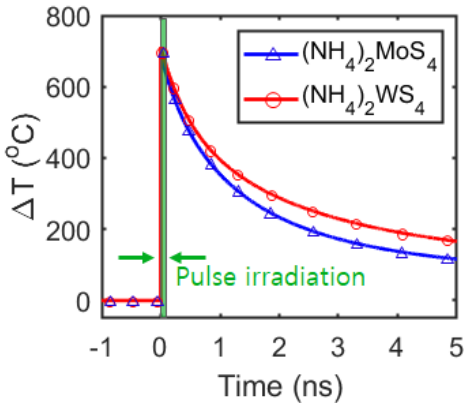

Figure 2-3. Transient temperature decays under a single laser pulse irradiation at t = 0 (pulse width ~ 100 ps) for the synthesis of MoS_2 (blue) and WS_2 (red) homostructures. Temporal analysis was carried out by solving the 3D Laplacian of temperature distribution. The thermal diffusion time constants for each case

are found to be 1.8 ns and 2.4 ns, respectively, which are much longer than the time scale of energy input.

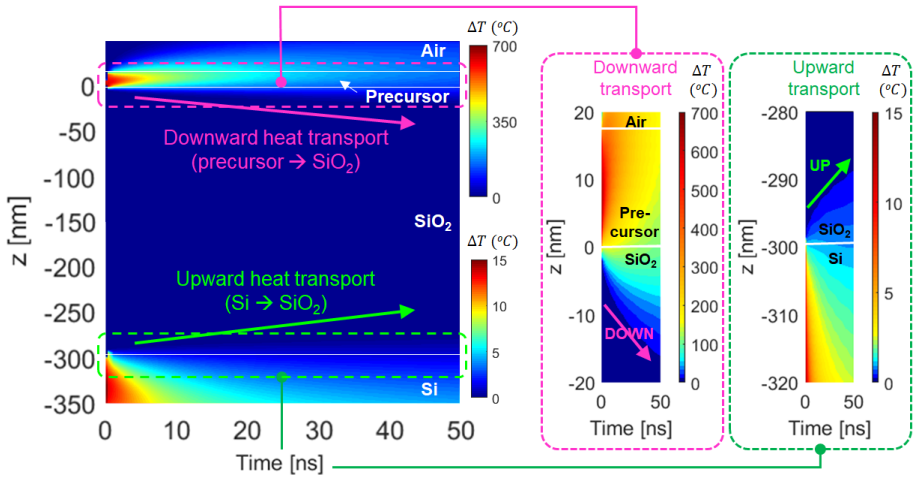

Figure 2-4. Time-domain thermal analysis of entire TMD synthesis configuration (precursor: 18 nm-thick / SiO_2: 300 nm-thick / Si: 675 μm-thick). Magnified views of each interface are provided on the right.

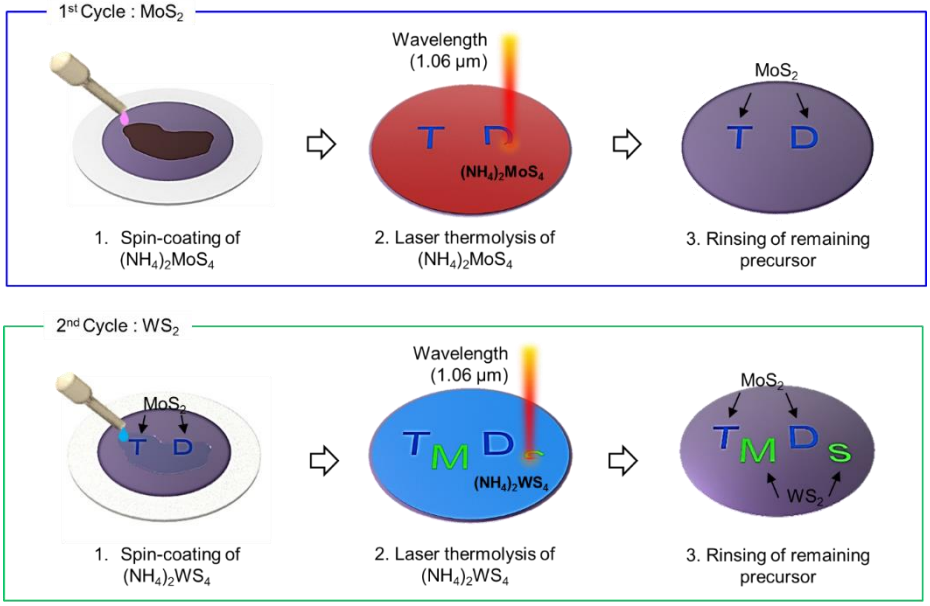

Figure 2-5. Schematic illustration of consecutive synthesis of individual MoS_2 and WS_2 homostructure patterns. Each cycle consists of 1) precursor spin coating, 2) laser annealing, and 3) rinsing of remaining precursor.

	Si	SiO_2	Air	$(NH_4)_2MoS_4$	MoS_2	$(NH_4)_2WS_4$	WS_2
n (refractive index)	3.5561	1.4497	1	1.4597	1.4591	1.4823	1.4680
k (extinction coefficient)	9.3×10^{-5}	0	0	5.7×10^{-3}	9.9×10^{-5}	6.0×10^{-3}	3.9×10^{-5}
t (thickness)	675 μm	300 nm	-	6 nm	2 nm	8 nm	3 nm

Figure 2-T1. Optical parameters of all materials used in the thermal analysis.

Given with the angstrom-scale flat structure of spin-coated nanolayers in conjunction with the clear interface formed by abrupt change of refractive indices (*n*) between each layer, there exists a preferable condition for the appearance of multiple reflection at optical wavelengths. In such circumstance, an accurate measure of the interaction between laser pulse and parallel interfaces of the nanostructure is required. We adopted a commercial optical FDTD simulation tool (Fig. 2-2 a, Lumerical FDTD) to numerically estimate the amount of optical energy absorbed in each layer under a pulse irradiation. The real/imaginary refractive indices, which were observed by the ellipsometry, govern the optical geometry in the simulation.

For a synthesis of homostructure MoS_2 layer (Fig. 2-2 b, the simulation assumes that a precursor layer is stacked on top of the SiO_2 substrate, and it

estimates the intensity of electric field along the depth, as shown in Fig. 2-2 c (green). Interestingly, the intensity is found to be even higher along the depth of precursor layer, which is commonly supposed to be at the outermost surface. Such phenomenon is due to the multiple reflection and accordingly induced optical interferences, where it signifies the need of optical simulation. In a more complicated structure, which may be studied in further works, *e.g.*, a stack consisting of tens of multiple nanolayers, the E-field distribution will be quite off from the simple estimation of Beer-Lambert law throughout the structure, and above process of optical simulation will become essential.

The product of the squared electric field (green) and absorption coefficient (blue) along the depth results in the amount of optical energy absorbed in each layer, which later be converted to the temperature change (red) ($\Delta T = \Delta E/cm$, c: specific heat, m: mass) under the assumption of 100 % energy conversion.

The thermal simulation in current study considers all heating and thermal transports in the entire geometric domain, which spans all of TMD synthesis configuration (precursor: 18 nm-thick / SiO_2: 300 nm-thick / Si: 675 μm-thick). To visualize the intra-/inter-layer thermal transports, above simulation result provides the temporal changes of temperatures for 50 ns from the pulse irradiation. For a specific representation of the two interfaces of our interest (precursor/SiO_2 and Si/SiO_2), the thick volume of Si ($z < -350$ nm) was omitted in the visualization. Also, due to 1 ~ 2 order of different temperature scales in each top and bottom regions of visualization, they are colored with different

color scales (0-700 ºC for precursor/SiO_2 and 0-15 ºC for Si/SiO_2). The two magnified views of interfaces are shown on the right to clearly indicate the downward and upward heat transports from each heat source (precursor and Si, respectively).

As a result, the initial heat generation and temperature increase in Si ($\Delta T \sim 15\ ^{o}C$) is found to be much smaller than the precursor ($\Delta T \sim 700\ ^{o}C$) roughly as much as the ratio of their absorption coefficients. In addition, due to the low thermal conductivity of SiO_2 (interfacing layer between precursor and Si), the upward heat transport from Si to SiO_2 is suppressed and the thermal energy in Si, whose thermal conductivity is ~2 orders higher, preferentially dissipates horizontally within itself. Similarly, the downward heat transport from precursor to SiO_2 can penetrate only a few nanometers into the depth of SiO_2, and followingly, the two vertical thermal transports are hardly bridged through the interfacing layer. Therefore, we could safely consider that the two thermal systems in precursor and Si are independent during the pulsed laser based synthesis. Such consideration was applied to our manuscript as well, and thus for a simplicity, only the layers of precursor and SiO_2 were presented in the main Fig. 2-1 c.

Interestingly, under the optimized laser condition, we could not obsenge spectrum analysis (Fig. 2-6). The detail oxidation issue of MoS_2 that may arise during atmospheric synthesis will be discussed later. Fig. 2-1 f shows an SEM image of patterned MoS_2 with microscale resolution, where the darker

area represents the synthesized film. Specifically, regarding the linewidth of the resulting micropatterns, Fig. 2-1 g shows the variation obtained by drawing straight line patterns at different laser scribing speeds (5, 10, 15, and 20 mm/s). At a slow speed (5 mm/s), the pattern width was ~2 times wider than the irradiated beam size (~ 20 μm) due to in-plane thermal diffusion. However, such dispersion could be alleviated with faster scribing speeds, and at 20 mm/s, the width became nearly comparable to the beam size. Moreover, the maskless patterning technique can fundamentally avoid the polymer-induced contamination commonly observed in conventional photolithography. As shown in Fig. 1h, we confirmed that the MoS_2 film has a clean and atomically flat surface even after the pattern was formed. In addition, to demonstrate the broad applicability of our laser-based synthesis, above procedure was repeated by another type of commercial laser, *e.g.*, CO_2 laser, and successful synthetic quality was confirmed by the Raman analysis in Fig. 2-7.

Next, we conducted a set of controlled tests by tuning two variables, so as to obtain deeper insight into the selective synthesis: 1) the fluence of the laser pulse (F_{pulse}) and 2) the thickness of precursor layer. Fig. 2-8 a shows the Raman spectra of MoS_2 obtained at different laser fluences with a constant scribing speed of 5 mm/s. At low fluence, no distinct peaks were observed, similar to the $(NH_4)_2MoS_4$ precursor, whereas E_{2g} and A_{1g} peaks began to be observed under the stronger fluences above 2.45 J/cm^2. This peak proves that the amorphous precursor was converted to crystalline hexagonal MoS_2 because

the sufficient injection of optical energy locally heats the precursor layer to over the pyrolysis temperature of ~ 500 °C. Specifically, for the optimally synthesized MoS_2 film at F_{pulse} = 2.62 *J*/cm^2, an X-ray photoelectron spectroscopy (XPS) analysis was conducted. The regimes of higher/lower binding energies are separately shown in Fig. 2-8 b and c, respectively, and Mo $3d_{5/2}$ and S2 $p_{3/2}$ peaks were observed at 229.6 eV and 162.6 eV, respectively, which signifies the formation of 2H-MoS_2 [18, 19]. Strikingly, the absence of the Mo^{6+} $3d_{5/2}$ peak at 236 eV and S 2p peaks at 168 and 170 eV indicates successful synthesis of MoS_2 under open-air conditions without oxidation of Mo and S. Fig. 2-8 d shows the atomic ratios of sulfur, molybdenum, and oxygen extracted from the XPS spectra for intuitive comparison of the composition according to the laser fluences from 2.5 *J*/cm^2 to 3.0 *J*/cm^2. At the two opposite cases of lowest (2.5 *J*/cm^2) and highest fluences (3.0 *J*/cm^2), relatively high oxygen concentrations were observed, whereas the S/Mo atomic ratio was close ~2 at the optimal level of fluences (2.6 *J*/cm^2 ≦ F_{pulse} ≦ 2.9 *J*/cm^2). As a result of cross-checking with Raman analysis of the synthesized film for the tracking of oxygen (Fig. 2-6), it was identified that the intermediate reactant (*e.g.,* MoO_2) was remained in the film due to incomplete pyrolysis at low (≦ 2.5 *J*/cm^2) fluence condition [20, 21]. On the other hand, when the pulse fluence was higher than 3 *J*/cm^2, the surface of the MoS_2 film began to be oxidized and damaged because of the excessive photothermal energy [22, 23]. In addition, we found that the appearance of a small amount of oxygen under the optimized condition (2.6

$J/cm^2 \leqq F_{pulse} \leqq 2.9\ J/cm^2$) is attributed to the underlying SiO_2 layer, not to the MoS_2 film. Although the specific mechanism in the chemical reaction of the above partial thermolysis is not yet clear, an important piece of information is already obtained from the Raman and XPS analyses: high-quality MoS_2 can be synthesized even under ambient conditions if the precursor is rapidly pyrolyzed. Under such a rapid laser-induced photothermal reaction, we speculate that the S dramatically released from the precursor may push out the oxygen, which locally generates a sulfur-rich atmosphere and enables the synthesis of MoS_2. At low fluence ($\leqq 2.5\ J/cm^2$), the Raman peak of MoO_2 (*i.e.,* intermediate reactant) was observed at 284.4, 663.5, 820.8, and 993.3 cm^{-1} due to incomplete pyrolysis (Fig. 2-6 a). On the other hand, such oxygen peaks were not observed at the optimal level of fluences ($2.6\ J/cm^2 \leqq F \leqq 2.9\ J/cm^2$). In this reason, we can conclude a small amount of oxygen measured by XPS under the optimized condition is attributed to the underlying SiO_2 layer, not to the MoS_2 film. In addition, peaks of MoO_3 (oxidized MoS_2) at 225.3, 565.6, 750.7, and 823.5 cm^{-1} were observed at high fluence ($\geqq 3.0\ J/cm^2$), which was originated by oxidized or ablated MoS_2 due to excessive photothermal energy.

Moreover, we controlled the thickness of precursor layer to modulate the thickness of accordingly synthesized MoS_2 film, where the resulted variation could be directly measured by an atomic force microscopy (AFM) or indirectly estimated by comparing the mode spacing between E_{2g} and A_{1g} Raman peaks ($\Delta\omega = \omega_{A_{1g}} - \omega_{E_{2g}}$) [24]. As a result shown in Fig. 2-8 e, an increasing trend of

MoS_2 thickness during the use of thicker precursor layer was confirmed from both AFM and Raman estimation. Additionally, at the thinnest precursor layer of ~ 6 nm, the resulted thickness of MoS_2 was found to be 2.2 nm by AFM and the Raman mode spacing was as narrow as $\Delta\omega$ = 22.3 cm^{-1}, indicating a synthesis of approximately 3-layered MoS_2. The thickness uniformities of precursor film as well as followingly synthesized MoS_2 were confirmed by the mapping of height profiles using AFM across the 4 inch wafer. To demonstrate wafer-scale uniformity, the key factor is the deposition of homogeneous precursor film on the substrate by precise determination of the volume fraction of mixed solvent, concentration of solution, and volume dispensed on the wafer prior to spin coating. Detail parameters of spin-coating and the thicknesses of prepared precursor and resulted MoS_2 films are provided in Fig 2-T2. As a result, we were able to synthesize wafer-scale homogeneous MoS_2 films with their thicknesses from 8.2 ± 1.1 to 2.2 ± 0.4 nm while controlling the thicknesses of the precursor films from 24.1 ± 1.2 to 6.1 ± 0.6 nm, respectively (Fig. 2-9). The cross-sectional transmission electron microscopy (TEM) images in Fig. 2-8 f provide direct information on the number of MoS_2 lattices through the depth of the film. Due to the high crystallinity of our laser-annealed MoS_2 appearing as clear fringes in the TEM images, the resulted film thickness was measured as 6.2, 4.1, and 2.6 nm, which can be considered as 8L, 5L, and 3L of MoS_2 film, respectively. The insets in Fig. 2-8 f display top-view optical microscope images of the patterned MoS_2 film. The monotonous color

distribution means that all the synthesized areas have a uniform thickness. Overall, the results have proven the feasibility of the laser-based thermolysis method in controlling the physical (thickness) properties of the MoS_2 layer. Furthermore, the high degree of freedom provided by selective laser synthesis can further enable the fabrication of customized devices while providing extraordinary versatility in their designs and structures. Throughout these synthetic parameters (i.e. precursor preparation and spin coating) were explained in followed descriptions.

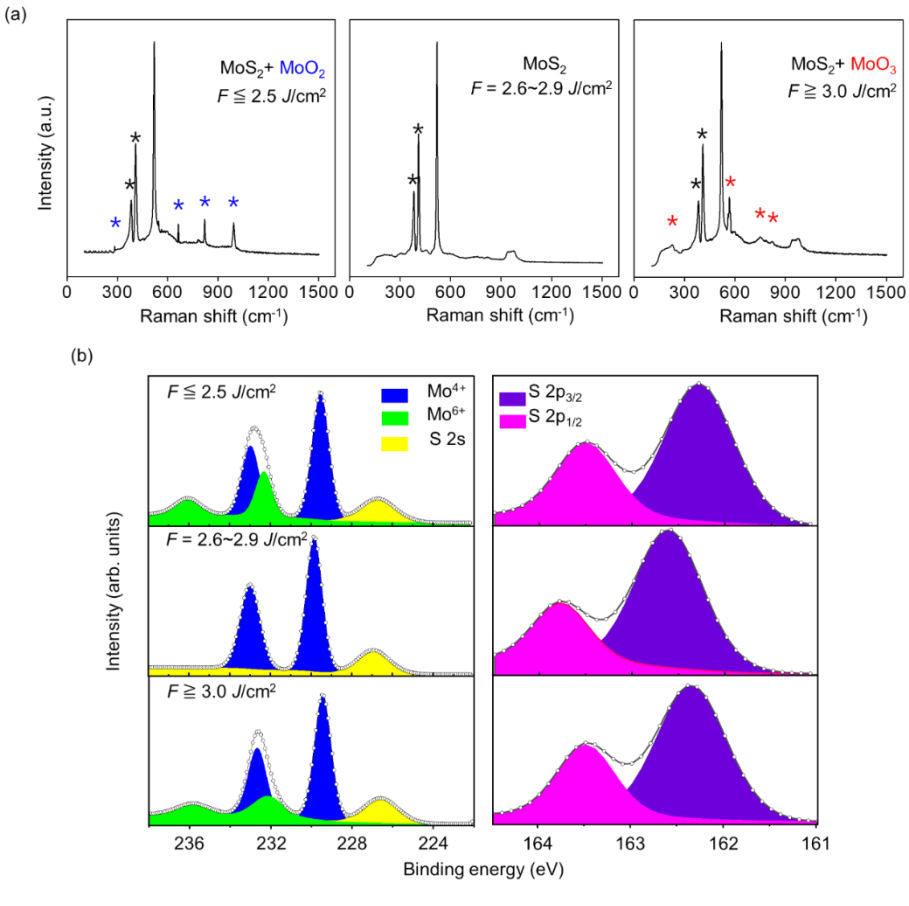

(c)

Laser fluence	Binding energy [eV] Mo 3d $3d_{5/2}$	Mo 3d $3d_{3/2}$	S 2s $S\ 2p_{3/2}$	S 2s $S\ 2p_{1/2}$	S/Mo ratio
2.34 J·cm^{-2}	229.48	232.71	162.37	163.46	1.83[a]
2.62 J·cm^{-2}	228.98		162.58	163.79	1.92[a]
3.07 J·cm^{-2}	229.53	232.72	162.11	163.45	1.78[a]

Figure 2.6. (a) Raman spectra of MoS_2 films synthesized at different laser fluences. (b) XPS spectra of Mo3d and S2p from different pulse laser fluences. (c) Detail information of Mo3d and S2p orbitals and their S/Mo ratios.

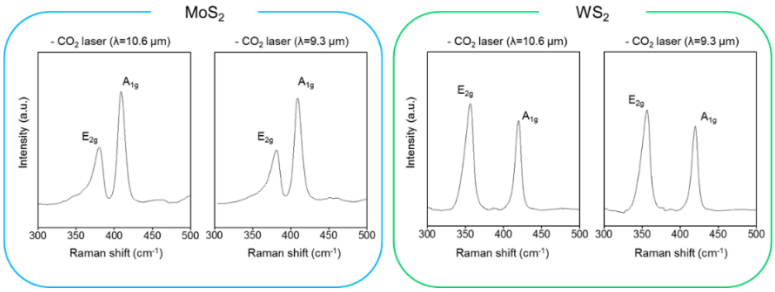

Figure 2-7. Raman spectra of MoS_2 and WS_2 films synthesized by different type of laser (CO_2 laser: λ= 10.6 μm and 9.3 μm).

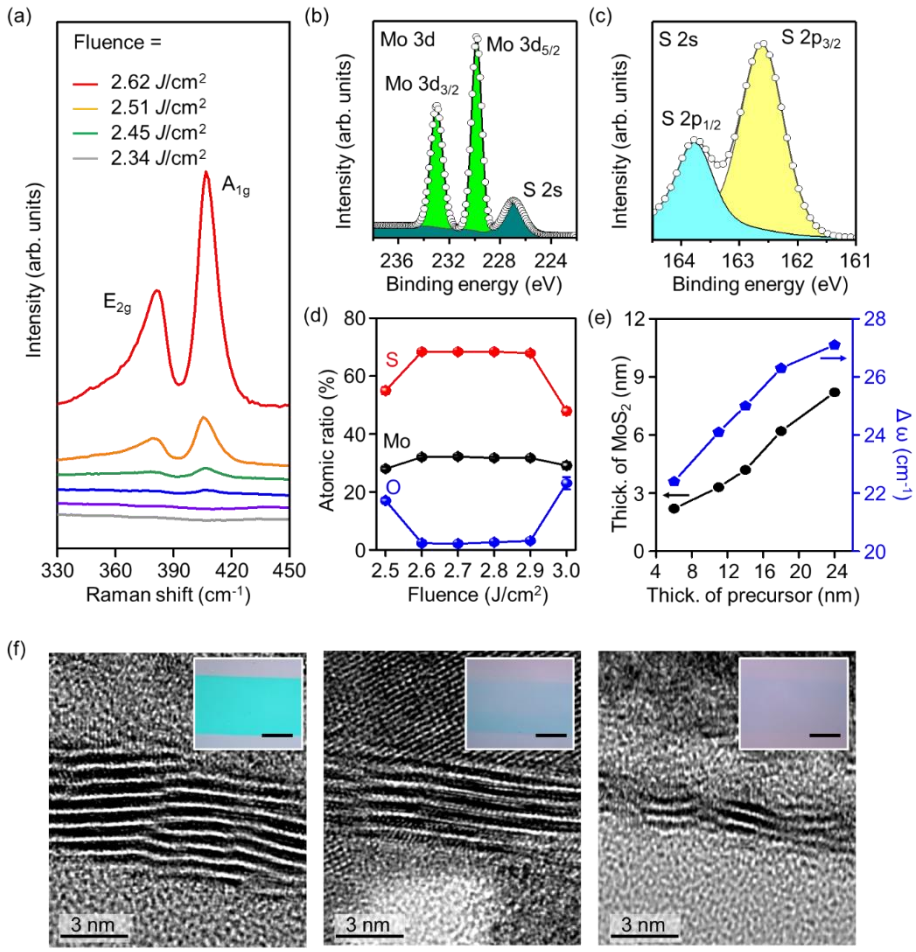

Figure 2-8. Crystallographic characterizations of selectively synthesized MoS_2. (a) Raman spectra of MoS_2 depend on laser fluence (J/cm^2) at fixed scribing speed 5 mm/s. (b, c) XPS results of Mo 3d and S 2p orbitals of synthesized MoS_2 film (2.62 J/cm^2). (d) Atomic ratios of Mo, O, and S in MoS_2 films synthesized at difference laser fluences. (e) Thickness modulation of MoS_2 by using different thicknesses of precursor layer (left: thickness of MoS_2, right: mode spacing between E_{2g} and A_{1g}). (f) Cross-sectional HR-TEM images of the

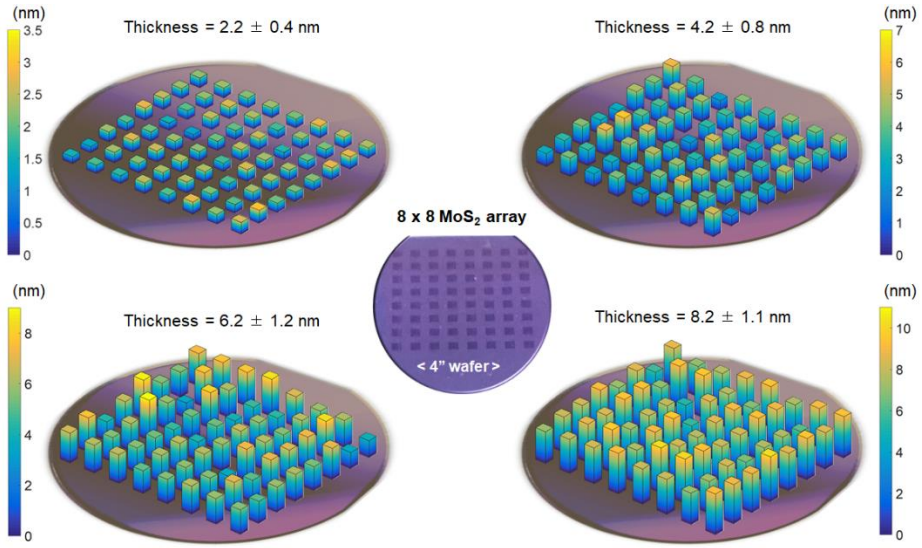

Figure 2-9. AFM-measured height profiles of 8×8 MoS_2 arrays with three different mean thicknesses.

In a synthesis of MoS_2 in wafer-scale, the uniformity of resulted film thickness highly depends on the quality of its precursor deposition, which often adopts a spin-coating with following parameters: precursor concentration (*i.e.*, precursor amount), solvent volume fraction, and spin-coating condition (rpm and time). Thus, through optimizations based on multiple tryouts, appropriate ranges of these parameters and recipe of mixture were defined for the preparation of homogeneous precursor film.

First, the precursor concentration was demonstrated in the manuscript for the control of synthesized MoS_2 film thickness as summarized in above Fig. 2-T2. Though, at a nominal extent of the concentrations (< 5 mM), the thickness control was successful with high uniformity, but further excessive dose inevitably brought in a non-uniformity, which was presumably attributed to the limited solubility of the precursor in solvent.

Second, the DMF solvent was mixed with two additives of n-butylamine and 2-aminoethanol because, in the use of DMF by itself, significant amount of pinholes and dewetted regions were observed on the spin-coated precursor film. Thus, n-butylamine was introduced to enhance the solvation of precursor by increasing hydrogen bondings of thiomolybdate, where the enhanced dispersion decreased the chance of pinhole generation. Additionally, 2-aminoethanol was added to control the viscosity and surface tension of the mixture in an attempt to increase the chance of adsorption on the substrate during the spin-coating, resulting in a complete cover of entire wafer without

leaving a vacancy. The volume fraction of the mixture was optimized as DMF : n-butylamine : 2-aminoethanol = 5 : 2 : 1 (v/v/v).

Last but not least, the rpm and duration of spin-coating were carefully adjusted. Specifically, once the sufficient amount of precursor solution was drop-casted on a 4-inch wafer, the sample was pre-rotated at 500 rpm for 10 s to gently spread out the bulk solution throughout the surface and remove the excessive remaining volume. Consecutively, the rpm was increased to 2500 and maintained for 30 s to enforce stronger centrifugal force to leave a least amount, where the accordingly resulted thickness throughout the substrate was dominantly regulated by the attractive force between precursor molecules and substrate.

Given with the optimized method of precursor deposition, MoS_2 films were synthesized at each precursor concentration listed in above Fig. 2-T2, and characterized by AFM. In general, the thickness of synthesized MoS_2 film approximately followed one third of the original precursor film [1, 2], and attributing to the homogeneous precursor film, the resulted MoS_2 thickness distributions were found to be reasonably narrow.

*(DMF : n-butylamine : 2-aminoethanol)

Precursor concentration (mM)	Solvent volume fraction* (v/v/v)	Precursor amount (mg)	Spin coating	Precursor thickness (nm)	MoS_2 thickness (nm)
3.6	5:2:1 in 6 ml	38	1st : 500 rpm, 10s 2nd : 2500 rpm, 30s	24.1 ± 1.2	8.2 ± 1.1
2.4		25		18.1 ± 1.1	6.2 ± 1.2
1.8		19		14.1 ± 0.8	5.2 ± 1.1
1.2		13		11.1 ± 1.2	4.2 ± 0.8
0.6		6		6.1 ± 0.6	2.2 ± 0.4

Figure 2-T2. Optical parameters of all materials used in the thermal analysis.

It is also important to clarify the electrical characteristic of the synthesized two-dimensional material. To this end, we directly formed a micropatterned MoS_2 array on a 4-inch SiO_2/Si wafer, where each pattern works as a channel of a field-effect transistor (FET). Notably, only 5 min (with a scribing speed of 10 mm/s) was required to create 1600 rectangular micropatterns (150 μm × 300 μm). Then, the micropatterns were combined with a pair of thermally deposited Au/Ti contact electrodes, resulting in the representative wafer-scale MoS_2-based FET array shown in Fig. 2-10 a. Fig. 2-10 b plots the typical output characteristics obtained from the ion-gel gated MoS_2-based FET. The drain current (I_{DS}) exhibited saturation behavior and gradually increased as the positive gate voltage (V_{GS}) increased, showing the typical operation of an *n*-type semiconductor. The transfer characteristics (I_{DS}–V_{GS}) of a 6 nm-thick MoS_2 transistor at three different V_{DS} are shown in Fig. 2-10 c, with its log-scale in the inset. In an attempt to claim a uniform FET operation throughout the array,

50 randomly chosen devices were electrically characterized in terms of their threshold voltage, on/off ratio, and field-effect mobility, resulting in their statistical distributions summarized in Fig. 2-10 d-f, respectively. The same test was carried out three times for each FET array on a separate wafer with different mean thicknesses of MoS_2, *i.e.*, 2.2, 4.2, and 6.2 nm. From the repeated characterizations, the production yield was estimated at approximately 90 % and the rest of failure cases were not presented. As a result, the mean threshold voltage was found to be ~ 1.9 V with almost no dependence on the active layer thickness and the on/off ratios of drain currents were reasonably high up to ~ 10^3. In addition, the mean mobilities at increasing MoS_2 thicknesses were calculated to be 2.17, 4.54, and 6.39 $cm^2/V{\cdot}s$, respectively, and such positive correlation is attributed to the decrease in 1) interfacial coulomb impurity scattering and 2) contact resistance with increasing MoS_2 thickness [25, 26]. In addition to the MoS_2 with *n*-type aspects, we confirmed the feasibility on our selective synthesis of WS_2 which exhibits *p*-type semiconducting behavior. The uniformity of synthesis was validated by electrical characterizations of 50 different FET devices with mean thickness of 7.2 nm as shown in Fig. 2-11. It is noteworthy that even though the MoS_2 and WS_2 were synthesized under room conditions, still maintain their performances comparable to those of conventional solution process-based method as summarized in Figure 2-T3.

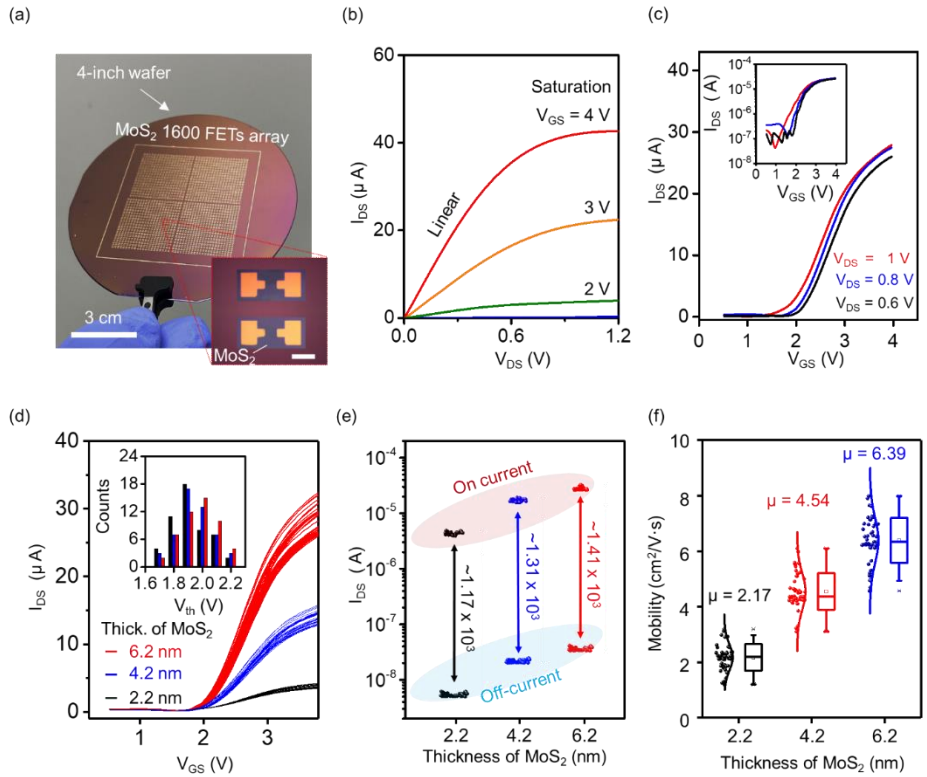

Figure 2-10. Electrical characterizations of selectively synthesized MoS_2. (a) Photograph of a MoS_2-based FET array on a 4-inch SiO_2/Si wafer, inset: magnified image of MoS_2 FETs, scale bar: 100 μm. (b) Output curve (I_{DS} *vs* V_{DS}) and (c) Transfer curve (I_{DS} *vs* V_{GS}) of ion-gel gated MoS_2 FET, inset: semilogarithmic scale. (d) Accumulated transfer curves (I_{DS} *vs* V_{GS}) from randomly selected MoS_2-based FET devices (50 samples for each set of thickness), inset: distributions of threshold voltages. (e) On/off ratio. (f) Distributions of charge mobility for each set of MoS_2 film thickness.

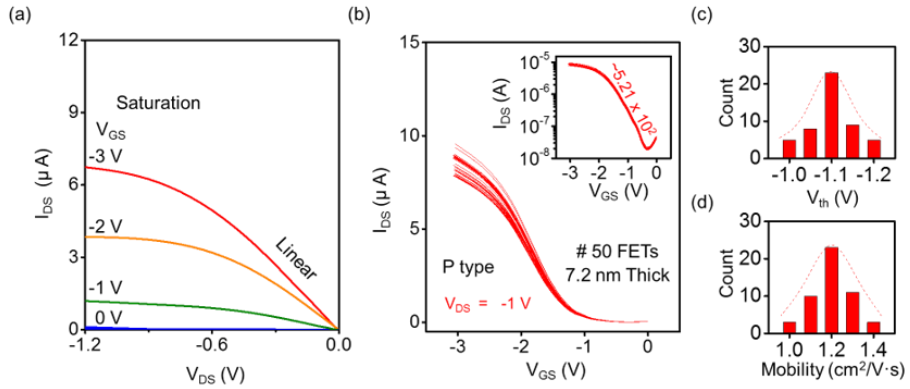

Figure 2-11. (a) Output curves (I_{DS} *vs* V_{DS}) and (b) transfer curves (I_{DS} *vs* V_{GS}) of ion-gel gated WS_2-based FETs, inset: semilogarithmic scale. Statistical distributions of (c) threshold voltages and (d) charge mobilities.

Materials	Synthetic method	Precursor/ source	On/ Off Ratio	Mobility	Reference
MoS_2	Dip-coating/ CVD	$(NH_4)_2MoS_2$/ Ar + S	~ 10^5	~ 12.5	3
MoS_2	Dip-coating/ CVD	$(NH_4)_2MoS_2$/ Ar + S	~ 10^5	~ 6	4
MoS_2	Spin-coating/ CVD	$(NH_4)_2MoS_2$/ Ar + S	~ 10^5	~ 0.5	5
MoS_2	Laser thinning	MoS_2 flake	~ 10^3	~ 0.49	6
MoS_2	Spin-coating/ CVD	$(NH_4)_2MoS_2$/ Ar + H_2	~ 10^4	-	2
MoS_2	Spin-coating/ CVD	$(NH_4)_2MoS_2$/ Ar + S	~ 10^4	~ 0.24	7
MoS_2,WS_2, $Mo_xW_{2-x}S_2$	Spin-coating/ CVD	$(NH_4)_2MoS_2$/ $(NH_4)_2WS_2$ Ar + S	~ 10^8	~ 0.1	8
MoS_2, WS_2	Spin-coating/ laser annealing	$(NH_4)_2MoS_2$/ $(NH_4)_2WS_2$	~ 10^3	~ 6.39	Our work

Figure 2-T3. Comparison of electrical properties of transistors fabricated by different synthetic methods.

Throughout the experimental verifications in this study, our laser based layer-selective thermolysis approach has been confirmed to allow rapid formation of various patterns over a large area without damaging the surrounding materials and is capable of the production of customized electronic devices. As a proof of concept, we directly demonstrate MoS_2-based strain gauge on rubber substrate to monitor human motion, which requires various patterned structures depending on the purpose of detecting mechanical deformations such as bending, stretching, and distortion. The fabrication process of strain gauge is presented in Figure 2-12 a, which follows almost the same layer-selective synthesis of homostructure in Figure 2-1, but the only difference is the existence of pressure-sensitive adhesive film (PSAF, 200 μm-thick) as a rubber substrate on top of the precursor (step 1). Due to the high transparency and low absorption coefficient $\alpha = 25\, m^{-1}$ of PSAF at $\lambda = 1.06\ \mu m$ (Figure 2-13), its quality could safely be maintained under the laser irradiation even while the underlying precursor layer was selectively heated (step 2). After that, the synthesized MoS_2 with a flexible PSAF substrate was naturally separated from the original SiO_2/Si substrate by wet-etching of underlying SiO_2 sacrificial layer (step 3). The direct synthesis of MoS_2 on a rubber substrate can be regarded as a representative advantage of our layer-selective synthesis, where only the precursor layer was selectively annealed while the adjacent layer could avoid excessive temperature increase. The completed strain gauge was then transferred to a stretching machine for an

accurate application of tensile strain, and the following change in the relative resistance of the gauge was monitored in a range of 0 to 3 % as shown in Figure-12 b. Under low strain (<1.67 %), the gauge operated reversibly without hysteresis, and its resistance was linearly proportional to the strain, known as the piezoresistive effect. However, as the strain increased (1.67 % ≤ ε < 2.6 %), its response slightly shifted to the nonlinear regime with poor reversibility, attributed to microcrack formation in MoS_2 [27]. At even higher strains above 2.6 %, the device suffered from large fractures and lost its functionality. In the linear regime, which will be used for the normal range of operation, the gauge factor (G.F.) was found to be 51.2, which was slightly lower than but comparable to that obtained with CVD-grown MoS_2 (≈ 70) [28]. We speculate that the lower G.F. value originated from the larger thickness of the MoS_2 film, resulting in a narrow and indirect bandgap [29]. A single strain gauge of MoS_2 was subjected to a rigorous repeatability test to evaluate its mechanical stability at different strain levels between 0 and 1.5 %, and the resulting relative resi stance changes are shown in Figure 2-12 c. Up to the highest strain in t he linear operation regime (ε =1.5 %), the strain gauge presented a sta ble response throughout 1000 repeated test cycles. Next, we demonstrate a rosette strain sensor consisting of three strain gauges offset by 120° from each other, which can be used to find the direction of unknown stress. For calibration, a spot near each gauge was gently pressed, and all configured sensors worked uniformly. The detail each gauge information was demonstrated in Figure 2-14.

Figure 2-12 d summarizes the simultaneously measured resistance variation for each aligned gauge when stress was applied in unknown X° (purple) and Y° (orange) directions on the wrist. Since each gauge experiences different effective strains that depend on the direction of applied stress, we can estimate the unknown direction through the mutual resistance variation behavior. Therefore, the values of the above X° and Y° were obtained as 30° and 240°, respectively [30].

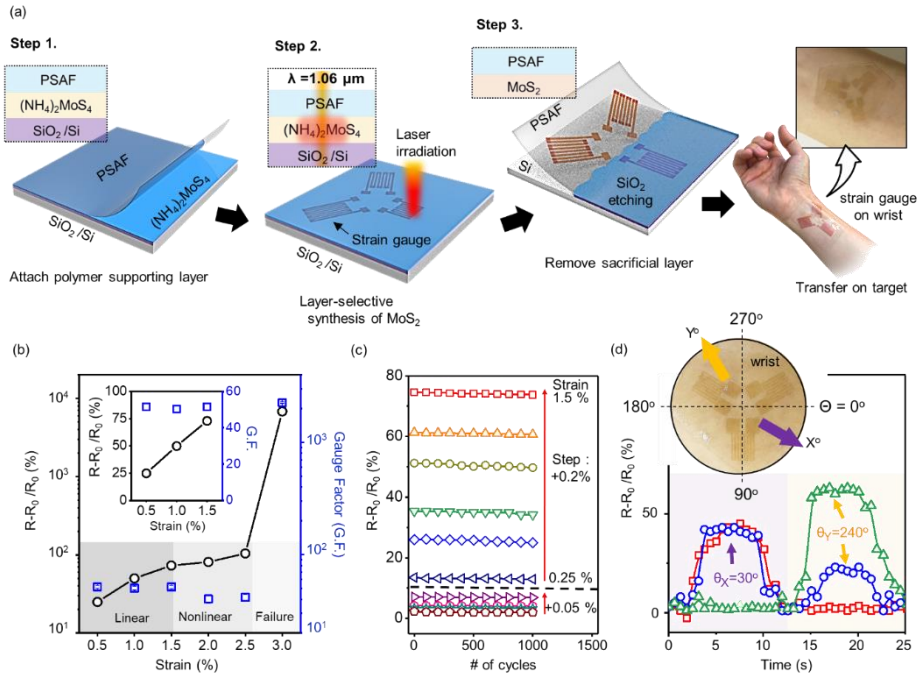

Figure 2-12. Layer-selectively synthesized MoS_2 strain gauge on rubber substrate. (a) Schematic illustration of the fabrication process of MoS_2-based rosette strain gauge. (b) Changes of relative resistance and gauge factor in a strain gauge under different amount of enforced strains, inset: magnified view of linear regime. (c) Fatigue test (1000 cycles) of MoS_2 strain gauge with a

variety of strain levels within 0.05 % and 1.5 %. (d) Operation of MoS_2-based rosette strain gauge on a human wrist.

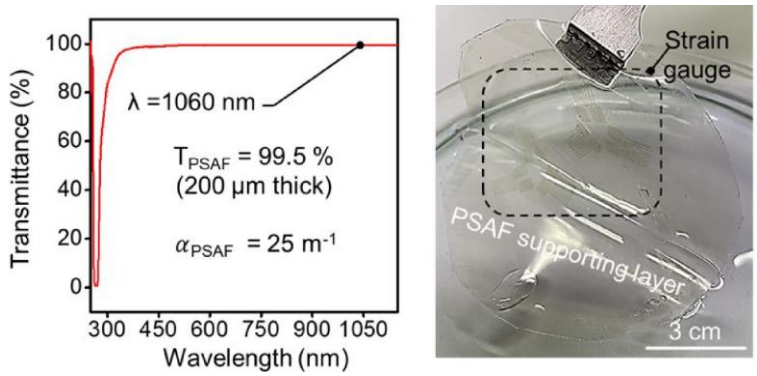

Figure 2-13. Transmittance of PSAF (left) and photograph of MoS_2-based strain gauge (right).

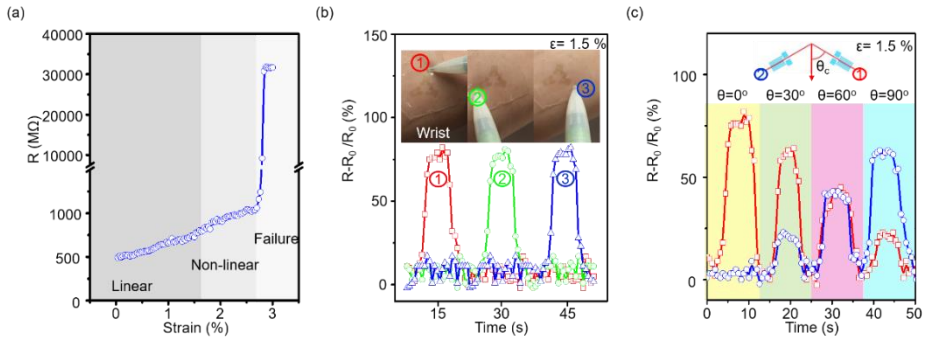

Figure 2-14. (a) Resistance change in MoS_2 strain gauge under different amount of enforced strains. (b) Operation of rosette strain gauge with three sensing branches placed in each different direction. (c) Directional responses of rosette strain gauge.

The laser-based selective synthesis method proves its real worth when implementing vertically stacked WS_2/MoS_2 heterostructure. For this, we coated $(NH_4)_2WS_4$ precursor layer on top of a pre-synthesized MoS_2 layer and continued with the abovementioned laser annealing. Here, we note that the optical absorption coefficient of $(NH_4)_2WS_4$ ($\alpha = 7.1 \times 10^4\ m^{-1}$) is ~ 60 times higher than that of MoS_2. Accordingly, when the laser pulse was irradiated onto the $(NH_4)_2WS_4/MoS_2$ structure, only the $(NH_4)_2WS_4$ layer rigorously absorbed the incoming optical energy and selectively decomposed into WS_2, whereas the bottom MoS_2 layer experienced a minor temperature increase, as shown in Figure 2-15 a. For the quantitative analysis of such heterostructure thermolysis, the temperature profile throughout the depth of the stacked structure was simulated. Due to the use of a sub-nano pulse, whose time scale is much shorter than the thermal diffusion into the surrounding volume, the maximum temperature increase can simply be assumed to be linearly proportional to the input energy: $\Delta T = E_{op}/cm$ (c: specific heat, m: mass) [31]. The thermomechanical parameters of all materials under consideration are listed in Table S1. Finally, the vertical temperature profile of the heterostructure was obtained, as shown in Figure 2-15 b, and it is in good agreement with the abovementioned selective thermolysis; only the $(NH_4)_2WS_4$ precursor layer experiences a severe temperature increase to > 700 °C, which is a sufficient temperature for pyrolysis [32], while the pre-synthesized MoS_2 immediately beneath the hot precursor remains cold (< 100 °C) such that it is not thermally

degraded. Hence, the above result has proven that selective annealing by a pulsed laser is an effective way to produce layer-by-layer TMD structures. Moreover, it is noteworthy that the selective synthesis without possible damage to the neighboring structure is not yet available for conventional CVD-based thermal annealing systems. Figure 2-15 c provides a TEM image of the WS_2/MoS_2 heterostructure obtained with the selective synthesis method, whose junction interface is clearly identified by the color differences arising from different atomic numbers. The precursors were fully converted into WS_2 and MoS_2, and their interlayer spacing were 6.3 Å (WS_2) and 6.8 Å (MoS_2), which is comparable to conventional results [33]. In addition, no impurities were observed within the interface or at the top surface. Figure 2-15 d shows a Raman mapping image of the cross-aligned WS_2 (green, A)/MoS_2 (red, B) heterostructures and their junction (C), whose colors represent the intensity of the A_{1g} mode. The three representative Raman spectra observed at each location are compared in Figure 2- 15e. From position A and B, narrow and sharp E_{2g} and A_{1g} peaks were confirmed, which indicate the formation of MoS_2 and WS_2. Importantly, the Raman signal at the crossing point (WS_2/MoS_2 heterostructure, C) presents all the above four Raman modes, which means that the crystallinity of the bottom MoS_2 was preserved during exposure to the pulse. The electrical rectification property of WS_2/MoS_2-based *p-n* heterojunctions was evaluated after depositing Au/Ti and Au/Pd metal contacts for efficient charge injection. During the sweep of electric potential from -3.5 V to 3.5 V, the vertical

heterostructure exhibited good rectifying behavior, showing a forward-to-reverse current ratio of up to 10^3 as shown in Figure 2-15 f. Given with above confirmations on the successful synthesis of TMDs and their various applications to the electrical devices, our laser-based thermolysis are expected to have advantages over the previously reported solution-based methods, *e.g.*, liquid-phase-precursor-assisted method, hydrothermal method, and microwave-assisted method, in terms of its simultaneous patterning, short synthesis time, and hybridization with other TMDs. More details on the above comparative analyses are displayed in Figure 2-T4.

Our synthetic approach can be promise mask-less with p-n junction about the previous researches. In this perspective, the comparison of characteristics was descripted in below. The solution-based syntheses of transition metal dichalcogenides (TMDs) hold promises for a various opportunities because of their scalable and high-yield products by using low-cost precursors. In addition, the method can precisely control the composition of solution at the molecular level, which makes rational modifications on the process and composition of synthesized materials. With these advantages, the solution-based methods have become promising research for the synthesis and hybridization of 2D materials as summarized in Figure 2-T2. The representative solution-based synthesis methods can be classified into the hydrothermal and thermolysis methods. Generally, the former method has a form of nanosheets dispersed in a solution, the latter has a form of a thin film on a target substrate. Because of their

morphological differences [9-11], the thermolysis method is preferred for the demonstration of large-area electronics in array configurations.

In thermolysis method, the first remarkable achievement was reported in 2012 by using $(NH_4)_2MoS_4$ precursor [3]. This method became the standard for solution process-based TMDs synthesis. However, the relatively long process time (~ 2 hour) for sufficient decomposition of the TMDs precursor under high-temperature (~1000 ^oC), requiring a thermal furnace with pressure-controlled chamber, was considered as a huddle to be overcome. To reduce the thermal annealing time, U. Jeong group reported microwave-assisted annealing method. The method not only significantly reduced the synthesis time (45 ~ 90 sec), but also allowed a direct formation of TMDs film on a Si wafer substrate [12]. Furthermore, a study introducing functional additives in order to increase the film uniformity and production area was also reported [2]. However, their result in a form of thin film requires an additional patterning step in order to be mounted on an electronic device, demanding further processing time. In this regard, a direct patternable synthesis method by controlling the internal flow of solution precursor was suggested [13, 14]. By inducing anisotropic precipitation during the dip coating process, unidirectionally oriented TMDs ribbons were produced simultaneously with the synthesis. Although this method realized a MoS_2/WSe_2 heterojunction by allowing the TMDs to be stacked with other two-dimensional materials, but there was limited room for varying the patterns and enlarging the size. Considering above discussed research trends, our proposed

method of laser-based synthesis can achieve the formation of TMDs-based *p-n* junction structures with simultaneous patterning as well as the synthesis of wafer-scale active layer on a substrate within short processing time.

Recently, an interesting result of synthesizing doped TMDs using liquid-phase precursor was reported [15]. Although this method still seems difficult to synthesize in large areas, it presents important insights that can extend the functionality of TMDs which fabricated through the solution process. Therefore, if the synthesis mechanism is applied to the laser-based synthesis method suggested by us, it will be a unique way to fabricate TMDs with functionality as well as productivity.

Materials	Synthetic method	Synthetic area	Synthetic Time	*p-n* junction	Patternable	Ref.
MoS_2	Hydrothermal	Nanosheet	12 hr	X	X	9
MoS_2, WS_2	Hydrothermal	Nanosheet	24 hr	X	X	10
TiO_2/ MoS_2	Hydrothermal	Nanosheet	24 hr	X	X	11
MoS_2	Thermolysis (furnace)	1 x 1 cm^2	1.3 hr	X	X	3
MoS_2	Thermolysis (furnace)	6 inch	1.4 hr	X	X	2
MoS_2, WS_2 $MoSe_2$,WSe_2	Thermolysis (microwave-assisted)	2 x 2 cm^2	45~90 s	X	X	12
MoS_2 WSe_2	Thermolysis (furnace)	1 x 1 cm^2	2 hr	O	O	13
MoS_2 WS_2	Thermolysis (furnace)	1 x 1 cm^2	3 hr	O	O	14

MoS_2 ReS_2	Thermolysis (Liquid-phase precursor)	30 x 30 μm^2	0.45 hr	O	X	15
MoS_2, WS_2	Thermolysis (pulsed laser)	4 inch	~10 min	O	O	Our work

Figure 2-T4. Comparison of different methods of solution based-TMDs synthesis.

2. 5. Conclusion

In summary, we have successfully demonstrated the fabrication of patterned semiconducting MoS_2 and WS_2 films over a large area under ambient conditions using a rapid pyrolysis *via* laser annealing method. The high light absorption of the precursor allows selective and immediate heating, thus enabling the implementation of a patterned homostructure as well as a vertically stacked *p-n* heterojunction structure with a sharp interface. The resulting capabilities could facilitate applications not only in the fabrication of wafer-scale transistor arrays but also in customized electronics that require the formation of various patterns in a short time even under air condition. The obvious advantages, such as the ultrafast fabrication speed with process simplification, solution-based scalable/inexpensive process, and open-chamber process, are highly compatible with mass production. Our study is expected to contribute to the realization of high-performance TMD-based electronics with a similar technique as for present silicon-based electronics.

2. 6. References

1. Akinwande, D.; Huyghebaert, C.; Wang, C.-H.; Serna, M. I.; Goossens, S.; Li, L.-J.; Wong, H.-S. P.; Koppens, F. H. Graphene and Two-Dimensional Materials for Silicon Technology. *Nature* **2019**, *573*, 507—518.
2. Desai, S. B.; Madhvapathy, S. R.; Sachid, A. B.; Llinas, J. P.; Wang, Q.; Ahn, G. H.; Pitner, G.; Kim, M. J.; Bokor, J.; Hu, C. MoS_2 Transistors with 1-Nanometer Gate Lengths. *Science* **2016**, *354*, 99—102.
3. Goossens, S.; Navickaite, G.; Monasterio, C.; Gupta, S.; Piqueras, J. J.; Pérez, R.; Burwell, G.; Nikitskiy, I.; Lasanta, T.; Galán, T. Broadband Image Sensor Array Based on Graphene–CMOS Integration. *Nat. Photonics* **2017**, *11*, 366—371.
4. Iannaccone, G.; Bonaccorso, F.; Colombo, L.; Fiori, G. Quantum Engineering of Transistors Based on 2D Materials Heterostructures. *Nat. Nanotechnol.* **2018**, *13*, 183—191.
5. Lee, J.-H.; Lee, E. K.; Joo, W.-J.; Jang, Y.; Kim, B.-S.; Lim, J. Y.; Choi, S.-H.; Ahn, S. J.; Ahn, J. R.; Park, M.-H. Wafer-Scale Growth of Single-Crystal Monolayer Graphene on Reusable Hydrogen-Terminated Germanium. *Science* **2014**, *344*, 286—289.
6. Kang, K.; Xie, S.; Huang, L.; Han, Y.; Huang, P. Y.; Mak, K. F.; Kim, C.-J.; Muller, D.; Park, J. High-Mobility Three-Atom-Thick Semiconducting Films with Wafer-Scale Homogeneity. *Nature* **2015**, *520*, 656—660.
7. Lee, J. S.; Choi, S. H.; Yun, S. J.; Kim, Y. I.; Boandoh, S.; Park, J.-H.; Shin, B. G.; Ko, H.; Lee, S. H.; Kim, Y.-M. Wafer-Scale Single-Crystal Hexagonal Boron Nitride Film *via* Self-Collimated Grain Formation. *Science* **2018**, *362*, 817—821.
8. Kang, K.; Lee, K.-H.; Han, Y.; Gao, H.; Xie, S.; Muller, D. A.; Park, J. Layer-by-Layer Assembly of Two-Dimensional Materials into Wafer-Scale Heterostructures. *Nature* **2017**, *550*, 229—233.
9. Duan, X.; Wang, C.; Shaw, J. C.; Cheng, R.; Chen, Y.; Li, H.; Wu, X.; Tang,

Y.; Zhang, Q.; Pan, A. Lateral Epitaxial Growth of Two-Dimensional Layered Semiconductor Heterojunctions. *Nat. Nanotechnol.* **2014**, *9*, 1024—1030.

10. Son, Y.; Li, M.-Y.; Cheng, C.-C.; Wei, K.-H.; Liu, P.; Wang, Q. H.; Li, L.-J.; Strano, M. S. Observation of Switchable Photoresponse of a Monolayer WSe_2–MoS_2 Lateral Heterostructure *via* Photocurrent Spectral Atomic Force Microscopic Imaging. *Nano Lett.* **2016**, *16*, 3571—3577.
11. Mahjouri-Samani, M.; Lin, M.-W.; Wang, K.; Lupini, A. R.; Lee, J.; Basile, L.; Boulesbaa, A.; Rouleau, C. M.; Puretzky, A. A.; Ivanov, I. N. Patterned Arrays of Lateral Heterojunctions within Monolayer Two-Dimensional Semiconductors. *Nat. Commun.* **2015**, *6*, 1—6.
12. Xue, Y.; Zhang, Y.; Liu, Y.; Liu, H.; Song, J.; Sophia, J.; Liu, J.; Xu, Z.; Xu, Q.; Wang, Z. Scalable Production of a Few-Layer MoS_2/WS_2 Vertical Heterojunction Array and its Application for Photodetectors. *ACS Nano* **2016**, *10*, 573—580.
13. Lee, J. B.; Lim, Y. R.; Katiyar, A. K.; Song, W.; Lim, J.; Bae, S.; Kim, T. W.; Lee, S. K.; Ahn, J. H. Direct Synthesis of a Self-Assembled WSe_2/MoS_2 Heterostructure Array and its Optoelectrical Properties. *Adv. Mater.* **2019**, *31*, 1904194.
14. Yang, J.; Gu, Y.; Lee, E.; Lee, H.; Park, S. H.; Cho, M.-H.; Kim, Y. H.; Kim, Y.-H.; Kim, H. Wafer-Scale Synthesis of Thickness-Controllable MoS_2 films *via* Solution-Processing Using a Dimethylformamide/n-Butylamine/2-Aminoethanol Solvent System. *Nanoscale* **2015**, *7*, 9311—9319.
15. Liu, K.-K.; Zhang, W.; Lee, Y.-H.; Lin, Y.-C.; Chang, M.-T.; Su, C.-Y.; Chang, C.-S.; Li, H.; Shi, Y.; Zhang, H. Growth of Large-Area and Highly Crystalline MoS_2 Thin Layers on Insulating Substrates. *Nano Lett.* **2012**, *12*, 1538—1544.
16. Giri, A.; Park, G.; Yang, H.; Pal, M.; Kwak, J.; Jeong, U. Synthesis of 2D Metal Chalcogenide Thin Films through the Process Involving Solution-

Phase Deposition. *Adv. Mater.* **2018**, *30*, 1707577.

17. Kitamura, R.; Pilon, L.; Jonasz, M. Optical Constants of Silica Glass from Extreme Ultraviolet to Far Infrared at Near Room Temperature. *Appl. Opt.* **2007**, *46*, 8118—8133.
18. Jadwiszczak, J.; O'Callaghan, C.; Zhou, Y.; Fox, D. S.; Weitz, E.; Keane, D.; Cullen, C. P.; O'Reilly, I.; Downing, C.; Shmeliov, A. Oxide-Mediated Recovery of Field-Effect Mobility in Plasma-Treated MoS_2. *Sci. Adv.* **2018**, *4*, eaao5031.
19. Park, W.; Baik, J.; Kim, T.-Y.; Cho, K.; Hong, W.-K.; Shin, H.-J.; Lee, T. Photoelectron Spectroscopic Imaging and Device Applications of Large-Area Patternable Single-Layer MoS_2 Synthesized by Chemical Vapor Deposition. *ACS Nano* **2014**, *8*, 4961—4968.
20. Wang, H. W.; Skeldon, P.; Thompson, G. E. Thermogravimetric–Differential Thermal Analysis of the Solid-State Decomposition of Ammonium Tetrathiomolybdate During Heating in Argon. *J. Mater. Sci*. **1998**, *33*, 3079—3083.
21. Ponomarev, E. A.; Neumann-Spallart M.; Hodes, G.; Lévy-Clément, C. Electrochemical Deposition of MoS_2 Thin Films by Reduction of Tetrathiomolybdate. *Thin Solid Films* **1996**, *280*, 86—89.
22. Hu, L.; Shan, X.; Wu, Y.; Zhao, J.; Lu, X. Laser Thinning and Patterning of MoS_2 with Layer-by-Layer Precision. *Sci. Rep.* **2017**, *7*, 1—9.
23. Yang, H.; Giri, A.; Moon, S.; Shin, S.; Myoung, J.-M.; Jeong, U. Highly Scalable Synthesis of MoS_2 Thin Films with Precise Thickness Control *via* Polymer-Assisted Deposition. *Chem. Mater.* **2017**, *29*, 5772—5776.
24. Castellanos-Gomez, A.; Barkelid, M.; Goossens, A.; Calado, V. E.; van der Zant, H. S.; Steele, G. A. Laser-Thinning of MoS_2: on Demand Generation of a Single-Layer Semiconductor. *Nano Lett.* **2012**, *12*, 3187—3192.
25. Li, S.-L.; Wakabayashi, K.; Xu, Y.; Nakaharai, S.; Komatsu, K.; Li, W.-W.; Lin, Y.-F.; Aparecido-Ferreira, A.; Tsukagoshi, K. Thickness-Dependent

Interfacial Coulomb Scattering in Atomically Thin Field-Effect Transistors. *Nano Lett.* **2013**, *13*, 3546—3552.

26. Na, J.; Shin, M.; Joo, M.-K.; Huh, J.; Jeong Kim, Y.; Jong Choi, H.; Hyung Shim, J.; Kim, G.-T. Separation of Interlayer Resistance in Multilayer MoS_2 Field-Effect Transistors. *Appl. Phys. Lett.* **2014**, *104*, 233502.
27. Park, M.; Park, Y. J.; Chen, X.; Park, Y. K.; Kim, M. S.; Ahn, J. H. MoS_2-Based Tactile Sensor for Electronic Skin Applications. *Adv. Mater.* **2016**, *28*, 2556—2562.
28. Park, Y. J.; Sharma, B. K.; Shinde, S. M.; Kim, M.-S.; Jang, B.; Kim, J.-H.; Ahn, J.-H. All MoS_2-Based Large Area, Skin-Attachable Active-Matrix Tactile Sensor. *ACS Nano* **2019**, *13*, 3023—3030.
29. Yazyev, O. V.; Kis, A. MoS_2 and Semiconductors in the Flatland. *Mater. Today* **2015**, *18*, 20—30.
30. Bae, S.-H.; Lee, Y.; Sharma, B. K.; Lee, H.-J.; Kim, J.-H.; Ahn, J.-H. Graphene-Based Transparent Strain Sensor. *Carbon* **2013**, *51*, 236—242.
31. Taylor, L. L.; Scott, R. E.; Qiao, J. Integrating Two-Temperature and Classical Heat Accumulation Models to Predict Femtosecond Laser Processing of Silicon. *Opt. Mater. Express* **2018**, *8*, 648—658.
32. George, A. S.; Mutlu, Z.; Ionescu, R.; Wu, R. J.; Jeong, J. S.; Bay, H. H.; Chai, Y.; Mkhoyan, K. A.; Ozkan, M.; Ozkan, C. S. Wafer-Scale Synthesis and High Resolution Structural Characterization of Atomically Thin MoS_2 Layers. *Adv. Funct. Mater.* **2014**, *24*, 7461—7466.
33. Lee, S. K.; Lee, J. B.; Singh, J.; Rana, K.; Ahn, J. H. Drying-Mediated Self-Assembled Growth of Transition Metal Dichalcogenide Wires and Their H eterostructures. *Adv. Mater.* **2015**, *27*, 4142—4149.

Chapter 3.

Laser-Directed Synthesis of Strain-Induced Crumpled MoS_2 Structure for Enhanced Triboelectrification toward Wearable Haptic Sensors

[*The contents of this chapter is reproduced from: Seoungwoong Park, Jiseul Park, Yeon-Gyu Kim, Sukang Bae, Tae-Wook Kim, Kwi-Il Park, Byung Hee Hong, Chang Kyu Jeong*, and Seoung-Ki Lee* *Nano Energy* (2020) 78, 2211-2855. © 2020 Elsevier]

3. 1. Abstract

Two-dimensional (2D) transition metal dichalcogenide (TMDC) nanomaterials are currently regarded as next-generation electronic materials for future flexible, transparent, and wearable electronics. Due to the lack of compatible synthesis and study, however, the characteristic influences of 2D TMDC nanomaterials have been little investigated in the field of triboelectric nanogenerator (TENG) devices that are currently one of the main technologies for mechanical energy harvesting. In this report, we demonstrate a fast, non-vacuum, wafer-scale, and patternable synthesis method for 2D MoS_2 using pulsed laser-directed thermolysis. The laser-based synthesis technique that we have developed can apply internal stress to MoS_2 crystal by adjusting its morphological structure, so that a surface-crumpled MoS_2 TENG device generates ~40% more power than a flat MoS_2 one. Compared to other MoS_2-

based TENG devices, it shows high-performance energy harvesting (up to ~25 V and ~1.2 μA) without assistance from other materials, even when the counterpart triboelectric surface has a slightly different triboelectric series. This enhanced triboelectrification is attribute to work function change as well as enlarged surface roughness. Finally, the direct-synthesized MoS_2 patterns are utilized to fabricate a self-powered flexible haptic sensor array. The technique we propose here is intended to stimulate further investigation of the triboelectric effects and applications of 2D TMDC nanomaterials.

3. 2. Introduction

As human interface technologies continue to develop, an increasing number of electronic devices are capable of being implanted in or attached to the human body. For this reason, small-scale energy devices are regard as essential to pursuit fourth-generation industrial innovations for operating Internet of Things (IoT) electronics which are portable and mobile [1, 2]. Because mechanical energy sources are omnipresent in the surrounding environment, a wide range of piezoelectric and triboelectric energy harvesting technologies have been studied that convert biomechanical movement and environmental vibration into electric energy that can be utilized by self-powered electronic devices or sensors [3–6]. In particular, triboelectric nanogenerator (TENG) devices have attracted extensive attention both in academic research and the industrial sector, since they are capable of generating high electrical output as well as

being manufactured by low-cost and easy processes [3, 7, 8].

The mechanism of the TENG system is based on the coupling effect between triboelectrification resulting from surface frictions and electrostatic induction through equivalent circuits [9, 10]. Numerous materials for obtaining triboelectric effects from frictional surfaces have been investigated in previous studies, including polymers, ceramics, metals, and even some liquids [11]. Unfortunately, however, in spite of some progress in the development of TENG technologies, the field of self-powered triboelectric devices remains well short of its target: atomically thin two-dimensional (2D) transition metal dichalcogenide (TMDC) nanomaterials (e.g., MoS_2, WSe_2, etc.), regarded as the most representative future electronic materials for the flexible, transparent, and/or nanoscale devices of tomorrow [12, 13]. While a few studies have been conducted of 2D TMDC nanomaterials in triboelectric devices that use exfoliation processes or chemical vapor deposition (CVD) methods [14–17]. These approaches have critical drawbacks, including restrictions in synthesis area, time, and/or cost problems. For example, the active surface area in triboelectric devices is important for the density of current output generated. More significantly, these conventional methods for fabricating 2D TMDC nanomaterials have been unable to demonstrate reliable morphological controllability, even though surface morphology and proper roughness are highly crucial in triboelectric effects and related TENG performance [18].

This limitation remains a critical hurdle to overcome in the investigation of

triboelectric phenomena in 2D TMDC nanomaterials and related self-powered device applications. The well-known transfer technique after exfoliation or CVD synthesis is ineffective for morphological modifications, particularly for subsequent device fabrications with patterning [12, 19, 20]. Additional processes using 2D TMDC nanomaterials in device patterning have shown similar limitations with regard to aching fast and cost-effective device fabrications.

To investigate the triboelectrification principles of 2D TMDC nanomaterials, we present here a direct single-step laser processing method for morphologically controlled synthesis of atomically thin 2D MoS_2 layers, using a the photonic thermolysis mechanism. This directly patternable laser synthesis method tunes the surface topography of 2D MoS_2 layers in non-vacuum atmosphere, without any additional treatment or modification. The single-step morphological tunability results from interfacial cavities caused by the laser-assisted separation of the underlying SiO_2 thin film layer on the Si wafer. Both flat and crumpled MoS_2 layers synthesized by laser-directed thermolysis are thoroughly investigated using various material characterizations to analyze triboelectric phenomena on MoS_2 layers, as well as TENG device properties more generally. The flat MoS_2 TENG device produces an energy harvesting output of 17 V, 0.85 μA, and 1.6 μW, whereas the crumpled MoS_2 TENG generates 25 V, 1.2 μA, and 2.25 μW. On the basis of these results, it is evident that the crumpled MoS_2 TENG generates ~40% more power than the flat one. Throughout the comprehensive material characterizations, the main

determining factors in the performance enhancement are not only the increased surface roughness but also deviations in the work function of the laser-assisted crumpled 2D MoS_2 layers [21]. Finally, we transfer the patterned crumpled-MoS_2 layers onto a flexible plastic substrate to show a practical application. The crumpled MoS_2-based self-powered haptic sensor array detects well the movement of a stylus pen. By means of the noteworthy laser synthesis that it uses, this approach overcomes the limitations of previous 2D TMDC nanomaterials in the field of triboelectric energy harvesting and self-powered devices.

3. 3. Experimental

Synthesis method for laser-directed flat and crumpled MoS_2: Several pieces of highly p-doped SiO_2/Si (thermally oxidated SiO_2 thin film, 300 nm in thickness) were sonicated for 10min under ethanol and deionized water (DI water), in each case. To enhance hydrophilicity of the SiO_2 surface, O_2 plasma treatment was implemented at 100 W for 100 s, which provides good adhesive properties between the precursor solution and the SiO_2/Si wafer. The MoS_2 precursor, ammonium tetrathiomolybdate ($(NH_4)_2MoS_4$, Sigma-Aldrich), was dissolved in the co-solvent of *N,N*-dimethylformamide (DMF): n-butylamine: 2-aminoethanol = 5:2:1 (v/v/v) to tune the surface tension and viscosity of the precursor. The precursor was then spin-casted onto the surface-treated SiO_2/Si wafer at 2000 rpm for 40 s. The residual precursor solvent was dried at 150 °C

for 3 min. The deposited precursor was subsequently irradiated by a pulsed fiber laser system (Universal Laser Systems, Inc., wavelength of 1.06 μm, pulse width of ~100 ps, frequency of 50 kHz), under non-vacuum and simple open-chamber conditions. Prior to the laser irradiation, the printing condition was optimized with tuning Z-height (working distance) from 1 mm to 2.5 mm to a defocused laser beam for synthesizing MoS_2 film type. After characterizing laser condition, laser scribing was implemented onto the coated precursor film ($(NH_4)_2MoS_4$ solution on the SiO_2/Si wafer), which was thermally decomposed by the absorbed photonic energy. The irradiated area and the scribing pattern information were controlled by Corel DRAW software and laser scribing software, respectively. To remove residual precursor film from non-irradiated regions, the specimen was immersed in DMF at 130 °C for 10 min.

Triboelectric nanogenerator (TENG) fabrication process: 2D MoS_2 (10 mm × 10 mm of active area) synthesized onto the SiO_2/ Si wafer was used for triboelectric layers with different surface morphologies. The highly p-doped Si wafer was also used for a bottom electrode. The polydimethylsiloxane (PDMS) (SYLGARD 184, Dow-Corning) used for the counterpart triboelectric surface was prepared using silicone elastomer base and curing agent mixed at a ratio of 10:1 (w/w). The PDMS liquid was spin-coated several times onto an Al plate as a top electrode, followed by curing. Copper wires were connected to each electrode for measurement. The TENG`s overall structure was established on

an acrylic fixture with four elastic springs and a gap of 3 mm, to produce an optimized contact-separation mode TENG [65].

Flexible haptic touch sensor fabrication process: The 4 × 4 direct patterned array of MoS_2 active layers was synthesized onto the SiO_2/ Si wafer from a laser-directed synthesis method. The area of a single MoS_2 sensor unit was 3 mm × 3 mm. The patterned Ag electrode was then directly formed on the MoS_2 array using an inkjet printer (Voltera, Q-V_ONE) with injection rate of 1 $uL \cdot s^{-1}$, speed of 10 $mm \cdot s^{-1}$, and working distance of 1 mm for measuring the self-powered sensor signals. To transfer the sensor array device to a flexible substrate, the PDMS film was spin-coated and cured on the prepared Ag/MoS_2 array patterns. The PDMS-covered Ag/MoS_2 array device was soaked in a wet etchant (buffered oxide etchant (BOE) : HF solution = 3 : 1 (v/v)) for 20 min to eliminate the underlying SiO_2 layer (i.e., sacrificial layer). Finally, the transferred sensor array device was cleaned by DI water to remove etchant residue. Then each MoS_2/Ag patterns was connected with an electrometer (Keithley 6514) measured the triboelectric signal of flexible haptic sensor during the single, multi, and dragging touch under the real-time.

Electrical measurements: Mechanical stress was periodically applied to the TENG devices using a bespoke pressing machine, a function generator (33220A, Agilent) and a power amplifier (pa-138, Labworks Inc.). The energy

harvesting signals extracted from the TENG devices were measured by an electrometer (6514 Electrometer, Keithley, USA). An oscilloscope (DPO 5204B, Tektronix, USA) was also used for frequency and force variation measurement. It should be noted that the electrometer has a large internal resistance, so it is easily capable of observing the electrical signals typically generated by TENG devices. However, it is relatively difficult to follow sensitive responses according to frequency and force changes. For this reason, an oscilloscope was used to monitor frequency and force changes, even though the measured signals tended to be reduced slightly due to the smaller internal resistance of the oscilloscope [66].

3. 4. Results and Discussion

Figure 3-1 a schematically illustrates the synthesis procedure for generally the flat MoS_2 as well as for the crumpled MoS_2 structure. Our photonic synthesis approach is based on the thermolysis of spin-coated $(NH_4)_2MoS_4$ precursor film to form atomically thin 2D MoS_2 layers, using a laser-directed annealing method on a thermally-oxidized silicon wafer (Si wafer with 300 nm-thick SiO_2 thin film). As shown in Figure 3-2, the $(NH_4)_2MoS_4$ precursor (light blue region) demonstrates strong sensitivity to the fluence of the fiber laser (at a wavelength of 1.06 μm) and its irradiation working distance. For this approach, the fluence of the laser pulse (F_{pulse}) was precisely controlled while working distance was set at 2.0 mm. When the laser is irradiated onto the

precursor/ SiO_2/ Si substrate, the photothermal interaction leads to heating of the precursor above a thermal threshold, forming a 2D MoS_2 layer (yellow region). Subsequently, $(NH_4)_2MoS_4$ residual precursor film from non-irradiated regions was immersed in DMF at 130 °C for 10 min. It has been reported that the $(NH_4)_2MoS_4$ precursor was almost pyrolyzed stepwise at a temperature above 500 °C, as shown in the following chemical formulae [22].

$$(NH_4)_2MoS_4 \rightarrow 2NH_3 + H_2S + MoS_3$$

$$MoS_3 \rightarrow MoS_2 + S$$

It should be noted that we successfully synthesized 2D MoS_2 using fast laser irradiation in non-vacuum and ambient environments, without needing to use a high-temperature furnace or chamber as an energy source for inducing thermolysis [23, 24]. The high optical absorptivity of $(NH_4)_2MoS_4$ at the wavelength of 1.06 μm ($\alpha = 6.7 \times 10^4$ m^{-1}) results in conversion to 2D MoS_2 layers while releasing ammonia and sulfur through absorption-induced self-heating under a F_{pulse} level above 2.52 $J \cdot cm^{-2}$. Due to instantaneous heating by the laser beam, around 12 nanoseconds are sufficient to synthesis 2D MoS_2 layers. A further noteworthy aspect of the MoS_2 synthesis method we have developed, then is that it has dramatically reduced the time of synthesis itself compared to previously reported methods [24–26]. Although some optical synthesis methods have been reported for graphene, [27–29]. Almost none have been reported

for 2D TMDC materials. Using various laser F_{pulse} levels, it was determined that the synthesized 2D MoS_2 layers have a flat surface when laser power is within the range from 2.52 to 2.61 $J \cdot cm^{-2}$ (indicated in blue pentagon shape in Figure 3-2). By contrast, the MoS_2 surface becomes three-dimensionally distorted and wrinkled when the irradiating F_{pulse} is stronger than 2.62 $J \cdot cm^{-2}$. As F_{pulse} increases, the small wrinkles that occurred in the early stages merge with one another, causing the larger crumpled structure, as seen in the optical microscopy (OM) image of Figure 3-3. As Figure 3-1 b illustrates, in this study, each surface structure of 2D MoS_2 is employed to contact-separation type triboelectric nanogenerators (TENG) devices to investigate the effect of 2D TMDC layers on triboelectric devices. Polydimethylsiloxane (PDMS) is used as a counterpart triboelectric material. Triboelectric output is generated by mechanical input that applies contact and separation between the two surfaces to induce triboelectric charges and surface potential differences.

Figure 3-1 c shows the cross-sectional scanning electron microscopy (SEM) images depicting the crumpled structure composed of a series of hills (red dotted lines) and valleys (blue dotted lines). Interestingly, the hill regions result from the interfacial separation between the underlying SiO_2 thin film and the Si mother wafer at repetitive parts, thus creating interfacial cavities. In the valley regions, the 2D MoS_2 and SiO_2 layers have remained in close contact. The distinct layer information of synthesized film was defined as a few layers of 2D MoS_2 parallel to the underlying SiO_2 layer, as shown in the cross-sectional

transmission electron microscopy (TEM) image (Figure 3-1 c, inset). The magnified images (right panels of Figure 3-1 c) confirm that the MoS_2/SiO_2 layers clearly detach from the bottom Si wafer without mechanical cracking while forming the local cavities.

This interfacial separation phenomenon can be explained by the principle of the laser-lift-off (LLO) process and intrinsic compressive stress on the thermally oxidized SiO_2 thin film as a result of the molar volume discrepancy between the Si and SiO_2 [30–32]. At F_{pulse} of around 2.6 $J \cdot cm^{-2}$, the SiO_2/Si interface containing the sub-stoichiometric oxide species begins to deteriorate, weakening interfacial adhesion [33]. As the F_{pulse} increases, the internal compressive stress of SiO_2 is correspondingly relaxed by the larger mechanical deformation due to interfacial detachment, resulting in the crumpled structure. The synthesized MoS_2 was characterized using Raman spectroscopy, as presented in Figure 3-1 d. Two strong E_{2g} and A_{1g} bands are displayed at wavelength positions of 379.9 cm^{-1} and 406.9 cm^{-1}, respectively, indicating that few-layered MoS_2 was successfully synthesized even on the crumpled structure. Figure 3-1 e plots the geometrical analysis of crumpled MoS_2 structures according to F_{pulse}. When irradiated F_{pulse} is 2.52 $J \cdot cm^{-2}$, the generally flat MoS_2 has begun to be synthesized, whereas the crumpled structure is formed at F_{pulse} of 2.6 $J \cdot cm^{-2}$ and above. As F_{pulse} increases up to 2.92 $J \cdot cm^{-2}$, both the height and period of the crumpled surface structure increase simultaneously. The most crumpled structure (with a hill height of ~5 μm and a period of ~22 μm) is

obtained at F_{pulse} of 2.92 J·cm^{-2}. The related evidence of series of hills and valleys was displayed in Figure 3-3, cross-sectional SEM images and line profile of the 3D holographic image. At higher laser fluence than 3 J·cm^{-2}, the precursor solution or synthesized MoS_2 layers undergo severe thermal oxidation.

For a systematic study, the modification in MoS_2 morphology can be classified according to the degree of surface distortion: flat MoS_2 (F-MoS_2, F_{pulse} = 2.52 J·cm^{-2}), less crumpled MoS_2 (LC-MoS_2, F_{pulse} = 2.78 J·cm^{-2}), and most crumpled MoS_2 (MC-MoS_2, F_{pulse} = 2.92 J·cm^{-2}) layers. The specific laser conditions for various MoS_2 surface morphology are detailed in Figure 3-4.

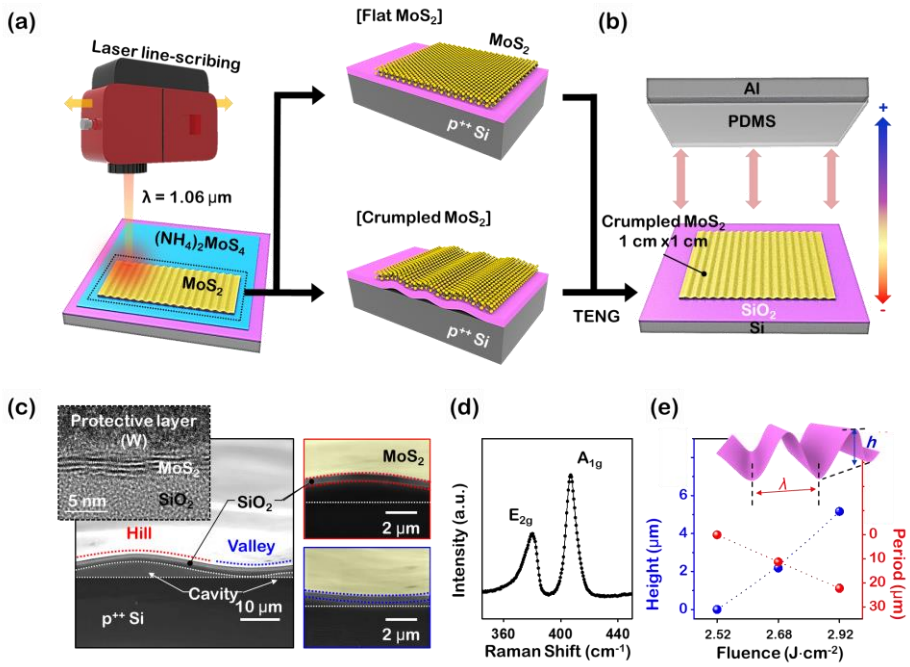

Figure 3-1. (a) Schematic illustration of laser-directed synthesis of 2D MoS_2

on the SiO_2/Si wafer, which can control the surface morphology: flat *versus* crumpled structures. (b) Illustration of MoS_2-based TENG device structures. (c) Cross-sectional SEM images of crumpled MoS_2 with various magnifications. Inset: cross-sectional TEM image of MoS_2. The right panels show the hill and valley of crumpled structure in detail. (d) Brief Raman spectrum of the crumpled MoS_2. (e) Variation of crumpled MoS_2 structures plotting the hill height and the wavy period according to incident laser fluence of the laser-directed synthesis.

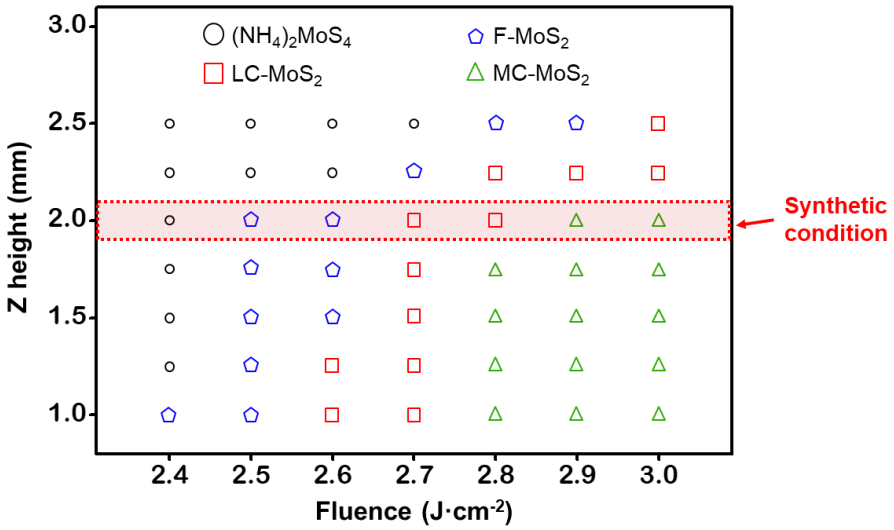

Figure 3-2. Phase diagram of MoS_2 structures according to the level of laser fluence.

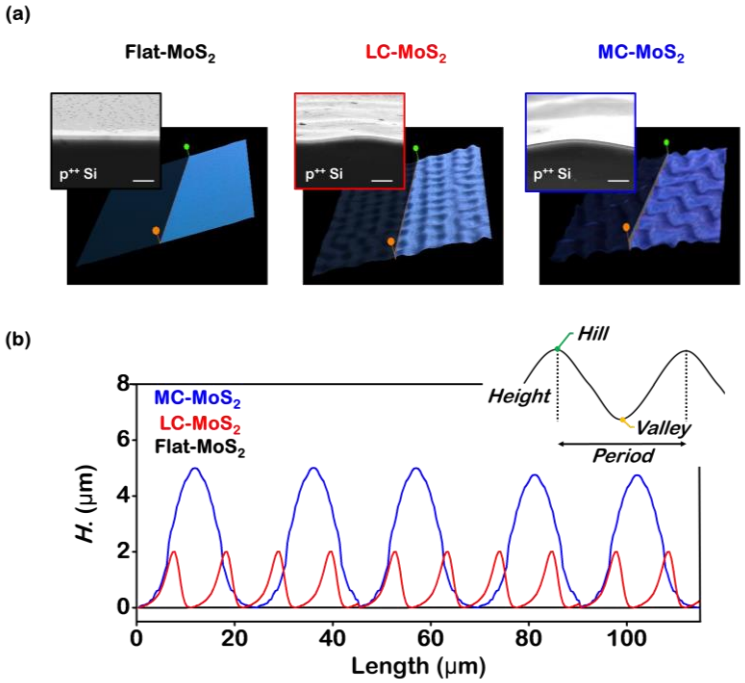

Figure 3-3. (a) The 3D optical compiler image of F-, LC-, and MC-MoS_2 films. Inset: cross-sectional SEM image of F-, LC-, and MC-MoS_2 films (scale bar: 10 μm). (b) Line profile of F-, LC-, and MC-MoS_2 films as marked along in 3D optical compiler image.

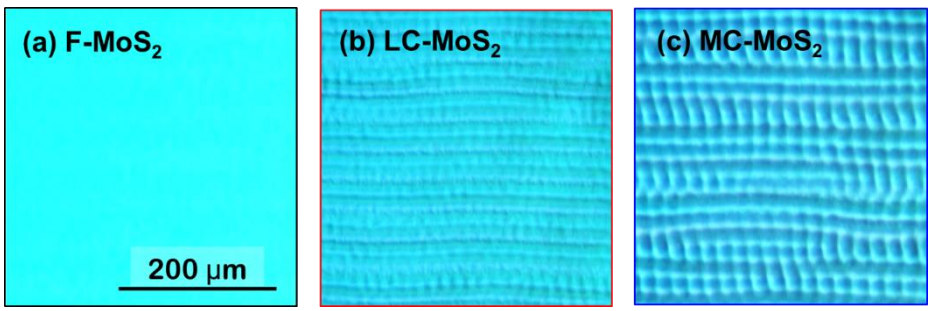

Figure 3-4. Optical microscopy (OM) images of laser-directed synthesized (a) F- MoS_2, (b) LC- MoS_2 and (c) MC-MoS_2 structures.

In-depth analyses were performed to investigate the electronic properties of laser-directed MoS_2 layers according to surface morphology. Figure 3-5 a shows atomic force microscopy (AFM) topographic 3D images of synthesized F-, LC-, and MC-MoS_2 layers over an area of 45 μm × 45 μm. The F-MoS_2 image shows uniform color distribution without significant wrinkles and/or cracks. However, some corrugated structures are observed with wrinkles, showing a hill height of 2.3 μm with a wavy period of around 10.2 μm. By contrast, the wrinkles in the MC-MoS_2 structure have a higher hill height about 5 μm with a larger wavy period of around 22 μm than those of the LC-MoS_2 structure. It should be noted that the larger wavy period entails a smaller number of hills and valleys, a phenomenon attributable to wrinkles merging with one another.

X-ray photoelectron spectroscopy (XPS) was also utilized to assess the chemical composition of each of the synthesized MoS_2 structures. As displayed in Fig. S4, the XPS spectra of F-, LC-, and MC-MoS_2 randomly measured at 10 point exhibit similar peaks in Mo3d ($3d_{3/2}$: 232.9 eV and $3d_{5/2}$: 229.8 eV with the S2s band of 226.8 eV) and S2p ($2p_{1/2}$: 163.7 eV and $2p_{3/2}$: 162.5 eV), respectively. These peaks indicate uniformly the presence of synthesized single phase of MoS_2, regardless of surface morphologies. Notably, the peaks in question provide information about the single phase of the MoS_2, existed as 2H-phase polymorphic without a Mo^{6+} peak (MoS_2 oxidation state) at the higher binding energy of 235.3 eV [34]. Using the information obtained from XPS

spectra, variations in the atomic composition of the synthesized MoS_2 layers was quantitatively analyzed according to F_{pulse}, as described in Fig. 3-5 b. The stoichiometric ratio of MoS_2 was well maintained within a fluence range from 2.5 $J \cdot cm^{-2}$ to 2.9 $J \cdot cm^{-2}$, indicating that high-quality 2D MoS_2 layers are synthesized on the surface without loss of sulfur or molybdenum atoms. This feature confirms that inducting morphological changes in as-synthesized MoS_2 by laser-based thermolysis does not produce undesirable ablation of or damage to the MoS_2. When laser fluence exceeds the threshold point (> 2.96 $J \cdot cm^{-2}$), the high photonic power dramatically accelerates oxidation of the MoS_2 layers, resulting in mechanical destruction (Figure 3-6).

Raman spectroscopy provides clear evidence of the atomic tensile strain caused by MoS_2 crumpling. Figure 3-5 c manifests Raman spectra for F-, LC-, and MC-MoS_2, respectively, using a 532 nm laser source. In the case of the F-MoS_2, two dominant peaks are observed, including the in-plane stretching mode at 383 cm^{-2} (E_{2g}) and the out-of-plane stretching mode at 406 cm^{-2} (A_{1g}), which typically indicate few-layered MoS_2 with approximately 4~6 layers [35]. By contrast, the MC-MoS_2 shows the redshift (or vibration softening) tendency of 1.6 cm^{-2} and 0.8 cm^{-2} at the E_{2g} and A_{1g} bands, respectively. Note that the redshift change of the E_{2g} peak is greater than that of the A_{1g} peak. These shifted spectra can be ascribed to softening in atomic vibration of MoS_2 owing to the atomic strain within the crumpled MoS_2 structures on account of the uniaxial strain that result from crumpling in underlying SiO_2. Moreover, the tensile

strain level of MC-MoS_2 is calculated as around 0.6% according to Raman analysis of the wrinkled MoS_2 [36]. This corresponds closely with the uniform uniaxial tensile strains during expansion of the MoS_2 lattice, as reported previously [37, 38]. In this concern, the MoS_2 crystallinity also changed from different tensile strain level, which caused by disordering of the MoS_2 crystal due to tensile strain and induces out-of-plane expansion, causing a peak shift of the lower angle from the (105) and (106) planes. (Figure 3-7).

The electrical properties of the crumpled MoS_2 layers were analyzed to investigate the effects of surface morphology, which is inevitably related to triboelectric properties. To measure electrical conductivity, contact electrodes (70 nm-thick Au with 7 nm-thick Ti adhesion) were fabricated on each of the MoS_2 structures for current (*I*)-voltage (*V*) curves (Figure 3-5 d). The measurement of electrical conductivity of the series of MoS_2 film begins with a value of resistance calculated by the slope of the *I–V* curve according to the Ohm's law. Then, the electrical conductance is expressed in equation (1), cm^2

$$\sigma = \frac{l(cm)}{\mathrm{R}(\Omega)\cdot A(cm^2)} \quad (1)$$

Where σ is the electrical conductivity of MoS_2, *l* is the channel length, *A* is the cross-sectional area of channel, *R* is the resistance at ambient temperature (30 °C). To calculate the electrical conductance under the same measuring condition, we defined the MoS_2 channel (3 nm in thickness

according to the TEM analysis) with a width of 50 μm and a length of 30 μm. As the surface corrugation increases from F- to MC-MoS_2, electrical conductance is augmented from 6.27×10^{-3} S cm^{-1} to 2.07×10^{-2} S cm^{-1}, approximately 3.3 times greater. The higher conductance is originated from the reduction of intervalley electron scattering by the strained lattice of the crumpled MoS_2 structure. The reduced scattering leads to a relatively small energy distance between K- and Q-valleys in the electronic band configuration of MoS_2, resulting in high conductance in the MC-MoS_2 structure [39].

As shown in Figure 3-5 e, ultraviolet photoelectron spectroscopy (UPS) analysis was also conducted to confirm the work function (Φ) of each MoS_2 structure, which is one of the important factors determining the triboelectricity of certain materials. The variation of work function is shown by UPS with increasing strain levels for various MoS_2 surface morphologies. The position of Fermi levels was calibrated using a gold reference sample measured in the same batch. The F-MoS_2 presented the lowest work function value (4.32 eV), which as reported previously is generally comparable to few-layered MoS_2 [40]. In comparison, the LC-MoS_2 had a higher work function value (4.43 eV), while the MC-MoS_2 presented the highest work function (4.54 eV). In comparison, the LC-MoS_2 had a higher work function value (4.43 eV), while the MC-MoS_2 presented the highest work function (4.54 eV). When the tensile strain applied to MoS_2, the separation between atoms gets increased due to its cause the orbital overlap toward decreased. Hence, the effective work function of the valence

band of highest point attains was moved from the *K* point of the valence band to the *Γ* point as followed MoS_2 lattice widening. Therefore, the location of valence bandwidth was decreased as well as Fermi energy level, which cause to increasing work function of MoS_2. In this perspective, increasing the work function of MoS_2 can accept more induced negative electron from the polymer layer during the triboelectrification because of widening empty electronic state of the MoS_2.

This electronic property can be considered as a significant factor in investigating the triboelectrification of 2D MoS_2 structures, because higher work function levels tend to induce more negative triboelectric charges in triboelectric series [41, 42]. In this perspective, increasing the effective work function of MoS_2 can accept more induced negative electron from the polymer layer during the triboelectrification because of widening empty electronic state of the MoS_2. The electron transfer process can be highly involved in triboelectric phenomena with semiconducting or metallic materials [43, 44]. Essentially, 2D MoS_2 has a higher work function than PDMS ($\Phi_{MoS2} > \Phi_{PDMS}$), electrons can be injected from the filled electronic state of PDMS to the empty one of 2D MoS_2 in order to equalize their respective Fermi levels during mechanical contact between two different material surfaces (the inset of Fig. 2e) [14]. Nevertheless, the triboelectric contributions of other charge types, such as ionic (e.g., H-termination) and/or mass (e.g., macromolecular chains) transfers, are still a subject of debate in cases involving insulating or polymeric

materials (e.g., PDMS) [45–47], and to date there has been no comprehensive study of the triboelectric effects of 2D MoS_2. The section that follows investigates effects more closely in regard to variations in work function and morphological changes of 2D MoS_2.

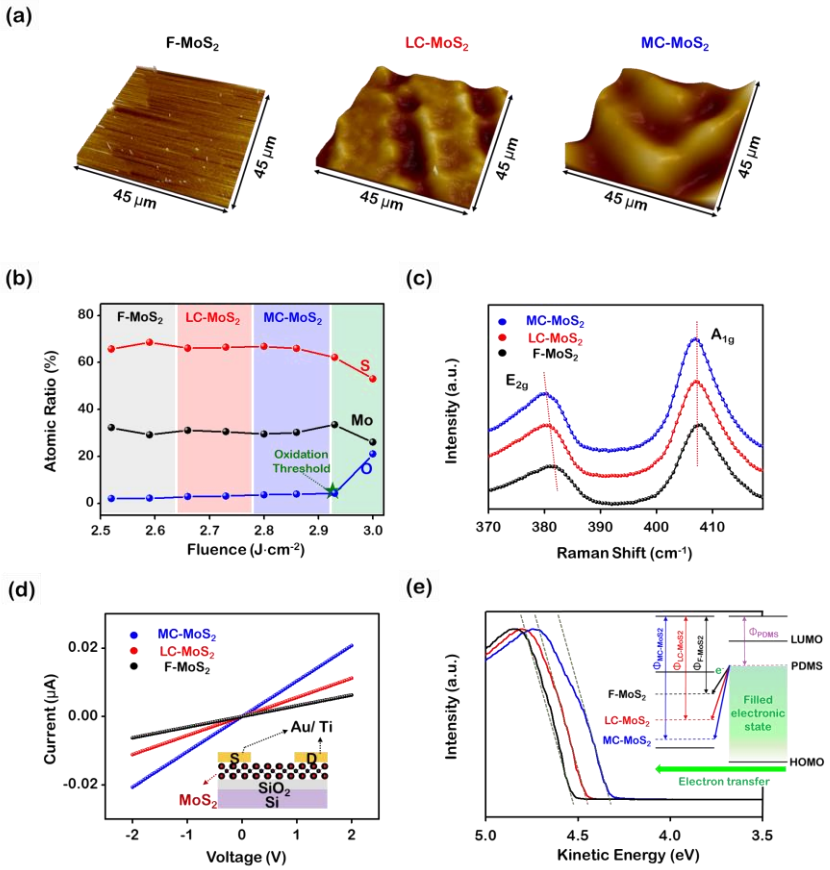

Figure 3-5. (a) AFM topographical images of three morphology types of the laser-directed MoS_2. (b) Atomic percentage of sulfur (S), molybdenum (Mo) and oxygen (O) extracted by the XPS spectra. (c) Raman spectra of the laser-directed F-, LC- and MC-MoS_2 layers. (d) Correlations of the conductance and

input voltage of F-, LC- and MC-MoS_2 layers (Inset: device structure for measuring conductance). (e) Variation of the effective work function of F-, LC- and MC-MoS_2 layers. Inset: schematic illustration of the mechanism of electron transfer depending on the work function modulation.

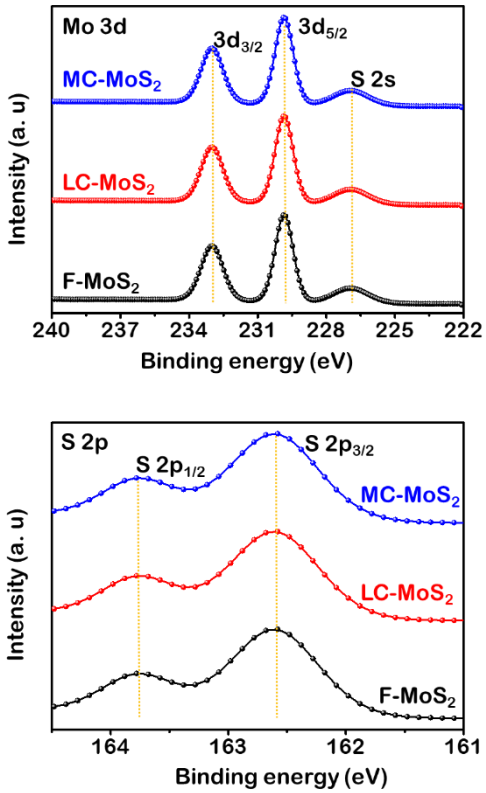

Figure 3-6. XPS spectra (scanning Mo3d and S2p energy levels) of the F-, LC- and MC-MoS_2 structures.

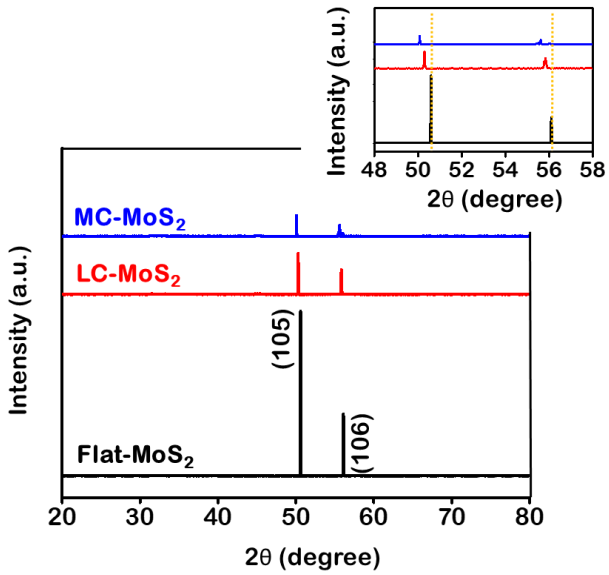

Figure 3-7. XRD spectra of the F-, LC- and MC-MoS_2 structures.

Based on laser-directed MoS_2 synthesis and surface modulation, the triboelectric effects of MoS_2 were investigated by fabricating the triboelectric nanogenerator (TENG) devices aforementioned in Figure 3-1 b. The pliable PDMS perfectly follows the curvature of the crumpled MoS_2 and prevents device breakage by dispersing the force applied to the Si wafer in contact-separation mode that applies a large force. To investigate the effects of the surface morphology of MoS_2 layers on triboelectric properties, each of the F-MoS_2 and MC-MoS_2 PDMS pairs was also measured as a comparison group under the same conditions. As shown in Figure 3-8 a and 3b, the TENG devices generate open-circuit voltage (V_{OC}) and short-circuit current (I_{SC}) energy harvesting signals under the default mechanical input (at a force of 160 N and

a frequency of 1 Hz). The flat MoS_2-based TENG (F-TENG) presented V_{OC} and I_{SC} 17 V and 0.85 μA, respectively, whereas the most crumpled MoS_2-based TENG (MC-TENG) produced V_{OC} and I_{SC} of 25 V and 1.2 μA, respectively. It should be noted that even the pristine MoS_2 (F-TENG) showed superior triboelectric energy harvesting performance compared to previous MoS_2-used TENG devices, without assistance from other materials and in spite of the smallness of difference in triboelectric series between MoS_2 and PDMS [14, 48]. This is presumably due to the grain size and layered structures specified by laser-based synthesis [49, 50], which we plan to study further in our follow-up research. Polarity-switched energy harvesting signals with the same levels were also obtained by the reverse connection with measurement equipment (Figure 3-9 a, b), indicating that the output measured was generated by the triboelectric devices. Additionally, the total generated charges affecting current flows at a single cycle can be calculated, showing a higher charge density of MC-TENG than that of F-TENG (Figure 3-9 c). Detailed fabrication and device conditions are described in the Experimental Section.

To inspect unpredictable flexoelectric effects in strained MoS_2 or SiO_2 layers, piezoresponse force microscopic (PFM) analysis was performed on both F-MoS_2 and MC-MoS_2. As previously reported, PFM displacement exists even in the out-of-plane direction of MoS_2, without intrinsic piezoelectric properties. This is due to a different form of electromechanical coupling known as flexoelectricity, produced by the inherent wrinkles-induced strain gradient [51].

As presented in Figure 3-8 c, the electromechanical response of MC-MoS_2 was around 4 times higher than that of F-MoS_2, but it is difficult to ascribe this to flexoelectric effects since the ~400% increase in piezoresponse is not theoretically possible due to flexoelectricity alone [51–53]. The sharp rise in PFM slope of the MC-TENG need to explained by other factors. A secondary effect producing strong impact on PFM is electrostatic charging within the object itself [53,54]. It can therefore be deduced that the interfacial cavities between the MoS_2/SiO_2 layers and the Si wafer inside the MC-MoS_2 specimen include substantial electrostatic charges, thus contributing to the unexpected surge in PFM signals.

The significant performance enhancement of MC-TENG can be attributed to the combined effects of the properties of the electronic material itself and its surface structural factor. Essentially, MoS_2 occupies slightly more negative position than PDMS in the triboelectric series [14]. Because the MC-MoS_2 has a lower the electronic work function due to its surface corrugation, its position in the triboelectric series can be considerably more negative, leading to a larger difference in triboelectric series between MoS_2 and PDMS. For this reason, larger electron transfers can occur when the two surfaces are in contact with one another. As typically is well known, the increase in the surface roughness of MC-MoS_2 can also lead to improvements in contact electrification. In cases where ionic and/or mass transfer mechanisms are dominant, however, merely increasing surface roughness will not enhance triboelectric output, because

more positive mass charges from the PDMS adhere to the MC-MoS_2`s surface [55], resulting in a far smaller triboelectric series difference between the two. Accordingly, we confirm that the triboelectrification principle of MoS_2 can be generally considered as an electron transfer mechanism, even with an insulating polymer. It may also be noted that the LC-MoS_2 shows similar triboelectric energy harvesting signals to those of the MC-MoS_2, indicating that the effects of work function should be a primary consideration in such a MoS_2 system. The high electronic conductivity of the MoS_2 synthesized by our laser-directed approach further supports this estimation.

As schematically illustrated in Fig. 3-8 d, the working principle of the MC-TENG device can be explained as a combination of contact electrification and electrostatic induction. In the initial state (i), no electron transfer occurs on either of the two triboelectric surfaces since they have had no prior contact with one another. In the pressed state (ii), the two triboelectric surfaces come into full contact with each other, generating triboelectric charges on their surfaces due to electron transfer from PDMS to MoS_2, depending on differences in their respective work function-based triboelectric series [14]. As negative triboelectric charges are produced on the MC-MoS_2 surface, the PDMS surface correspondingly turns into a relatively positive charged surface. As shown in Figure 3-8 c, secondary electrostatic charges may also emerge within the interfacial cavities due to the instantaneous contact between the strained SiO_2 thin film and its underlying Si wafer (as shown in Figure 3-8 d, upper right

inset). SiO_2 and Si can present relatively positive and negative charges, respectively [56]. Because inter-cavity electrostatic charging is highly localized, however, its effect on performance enhancement appears minimal. Moreover, it is clear that this secondary effect does not interfere with device performance overall, since the triboelectric charging tendency well corresponds to whole device structures (i.e., PDMS (+) / gap (3 mm) / MoS_2 (-) / SiO_2 (+) / Si (-)). As the external mechanical pressure is withdrawn in the releasing state (iii), the distance of the gap between the two charged surfaces is restored by the fixture springs of the device frame. At that point, an electrical potential is generated within the gap, generating to current flow from the top to the bottom electrode throughout the external circuit to compensate for the triboelectric charges produced by electrostatic induction. In the completely released state (iv), triboelectric charges are balanced, and the device`s system is electrically neutral. When mechanical force is reapplied to the device (v), the two triboelectric charged surfaces again move nearer to one another, breaking the electrical equilibrium and inducing an opposite electrical potential. Their electrons also travel in opposite directions through the external circuit and the polarities of the triboelectric signals are thus revered. When reciprocating mechanical force is applied repeatedly to the TENG device, the electrical energy harvesting signals are generated in response to the repetition in the mechanical sequence.

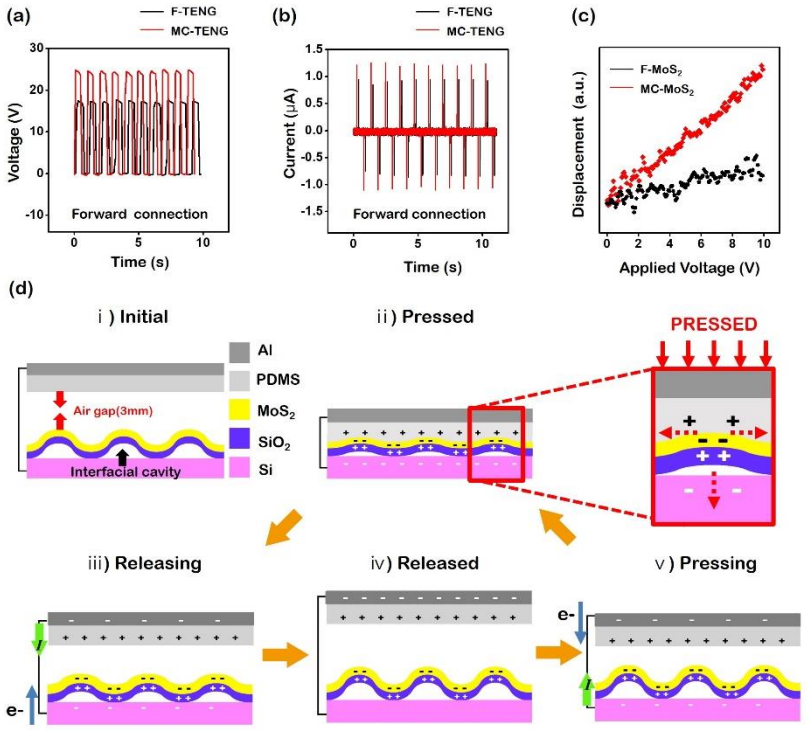

Figure 3-8. (a) Open-circuit voltage and (b) Short-circuit current generated from the F-MoS_2- and MC-MoS_2-based TENG devices under the external mechanical input of 1 Hz and 160 N as a default setting, with the forward connection to measuring equipment. (c) PFM analyses showing electromechanical coupling responses of laser-directed F-MoS_2 and MC-MoS_2. (d) Schematic diagrams presenting the device mechanism of the MC-TENG in its 5 states: i) initial, ii) pressed, iii) releasing, iv) released and v) pressing state.

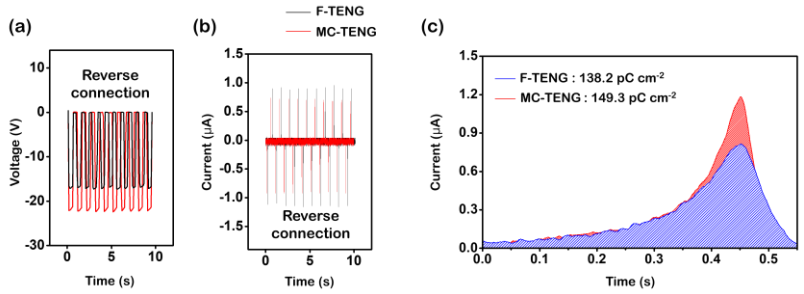

Figure 3-9. (a) Open-circuit voltage and (b) Short-circuit current generated from the F-MoS_2- and MC-MoS_2-based TENG devices under the external mechanical input, with the reverse connection to measuring equipment. (c) Area of a single generated current signal peak of F- and MC-TENG devices.

Figure 3-10 a depicts the instantaneous power generated as load resistance levels ranging from 1 kΩ to 1 GΩ for intuitive comparison between the F-TENG and MC-TENG devices. Power was calculated based on the equation, $P = V^2/R$ (P: instantaneous power, V: voltage, and R: load resistance) [9]. The voltage increases as the resistance increases, and then the voltage saturation begins at a specific resistance. At the beginning of the voltage saturation, the highest power is generated, after this, the power becomes low again following the equation. In our research, after showing the highest voltage at 100 MΩ, the saturation proceeded. As a result, the power decreased after 100 MΩ. When load resistance was 100 MΩ, both F-TENG and MC-TENG devices exhibited a maximum power of 1.6 and 2.25 μW, respectively. It is important that the MC-TENG produced energy harvesting power ~40% higher than the F-TENG. The matching resistance of both devices was the same (~100 MΩ), indicating that it was affected by macroscopic device structures, rather than the devices` MoS_2 surface morphologies.

The stability of the MC-TENG device was evaluated by the durability test over 10000 cycles of mechanical pressure input, as shown in Figure 3-10 b. Energy harvesting signals were stably maintained for the duration of cycle test. It has confirmed that the crumpled MoS_2 surface morphology remained securely on the substrate even after the durability test (Figure 3-11). The somewhat depressed topography in the MoS_2 microscope image is presumably due to the cumulative pressure exerted by the adhesive PDMS and the

lubrication of the MoS_2 layers, possibly causing the stabilized energy harvesting voltage down to ~21 V. Nevertheless, it is evident that strain-induced crumpling of laser-synthesized MoS_2 and the energy harvesting performance of a MoS_2-based TENG device can be stably used in various applications. The mechanical properties of 2D MoS_2 may be developed and improved in future studies that further investigate its various nano- and microstructures.

Figure 3-10 c shows the response of energy harvesting signals to changes in frequency within a range of from 1 to 10 Hz with constant mechanical stress. As the mechanical input frequency increased, the current output generated by the MC-TENG gradually decreased to 5 Hz. Figure 3-12 a also presents the voltage signal responses to changes within the same frequency range. The decrease in energy harvesting signals in response to increasing frequency was due to insufficient time in completing charge compensation and/or full contact electrification [57, 58]. After input frequency rose above 5 Hz, the energy harvesting signals became saturated, presumably due to the limited resolution of the measuring equipment [59]. The electrometer has the large internal resistance of the instrument, so it can be easy to measure the typical signal V_{OC}, I_{SC} measurement. However, it is relatively difficult to sensitive response about frequency and force changes. So, the frequency-dependent measurement was conducted using an oscilloscope. In order to maximize the accuracy of the tendency, an oscilloscope was set to the maximum plotting resolution (measured sample rate: 5 × 105 points / maximum sample rate: 10 $GS \cdot s^{-1}$,

maximum record length: 50 M points, vertical resolution: 8 bits). It could be note that, using an oscilloscope, though the measured values of VOC and ISC are slightly different due to the internal resistance, the trends can be clearly shown according to input condition. (In this case, an oscilloscope with probe internal impedance of 10 MΩ is used.)

With decreasing input mechanical force in the range from 160 N to 35 N, both voltage and current output generated by MC-TENG were gradually reduced (Figure 3-10 d and Figure 3-12). Lowered pressure force result in the less conformal contact between the MoS_2 layers and the counterpart PDMS surface as triboelectrification occurs [60, 61]. This explains the maximum triboelectric energy harvesting signals generated at 160 N. When mechanical force becomes greater than 160 N, the SiO_2/Si wafer under MoS_2 layers tended to suffer mechanical damage. To maximize the accuracy, force dependency was also measured by an oscilloscope. The frequency and force dependency of the energy harvesting signals generated by F-TENG devices was also evaluated (Figure 3-13), indicating that the output efficiency of MC-TENG is always higher than that of F-TENG regardless of the type of mechanical input.

To present some practical applications of using MoS_2-based triboelectric devices, we applied the MC-TENG device to simple commercial electronic components. As shown in Figure 3-10 e, electrical energy generated by the device can be directly used as a power electrical source for light-emitting diodes (LEDs), without the need for any additional energy sources. 25 blue LED bulbs

were connected in series to the device and a rectifier. They were activated intermittently following activation of the device. A 6 nF capacitor was connected to the device to confirm energy storage capability (Figure 3-10 4f). It was charged up to ~15.1 V by the 1 Hz-based energy harvesting output of MC-TENG for 90 s (Figure 3-10 f). Interestingly, the voltage charging graph exhibits a stair-shaped pattern, which clarifies that the capacitor was charged exclusively by the energy harvesting output from the MC-TENG device, without external artifacts. As expected, the charging rate became slower depending on the capacitance of the capacitors, indicating the TENG device`s applicability to general electrical circuits (Figure 3-13). The graph`s overall shape was parabolic, not linear, because charging and saturation are gradual in a capacitor with a constant capacity.

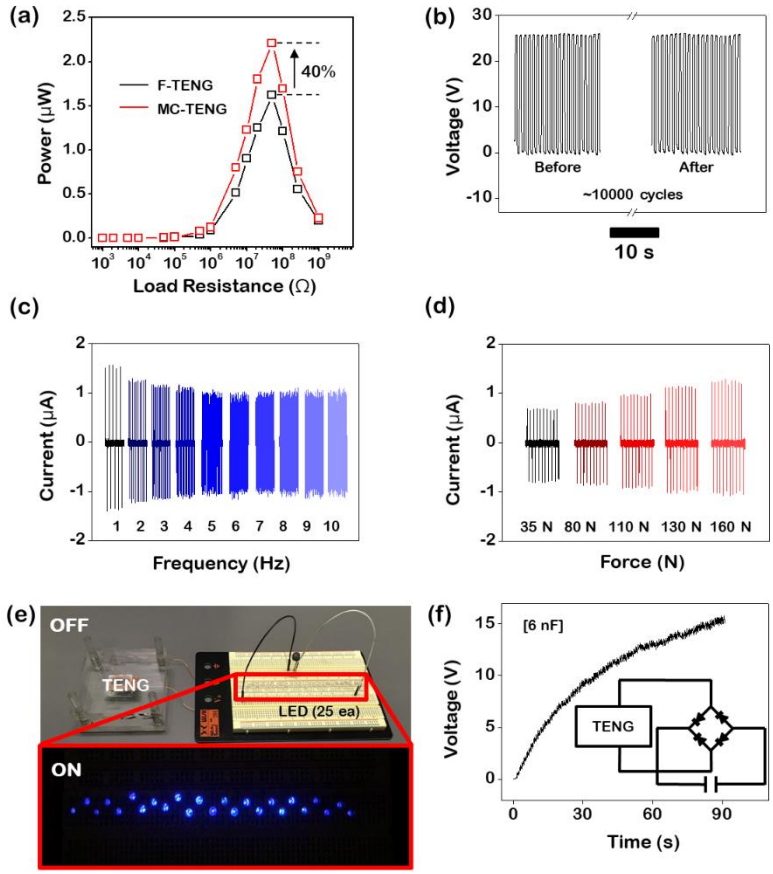

Figure 3-10. (a) Generated instantaneous output power levels of the F-TENG and the MC-TENG according to external resistance load. (b) Durability test of the MC-TENG devices over 10000 pressing cycles. (c) Frequency and (d) applied force dependence of generated current signals from the MC-TENG device. (e) Photograph of the commercial 25 blue LED bulbs connected to a rectifier and the MC-TENG devices (the upper panel). The 25 blue LEDs turned on by the MC-TENG (the lower panel). (f) A 6 nF capacitor stored up to 15.1 V for 90 s by the MC-TENG device.

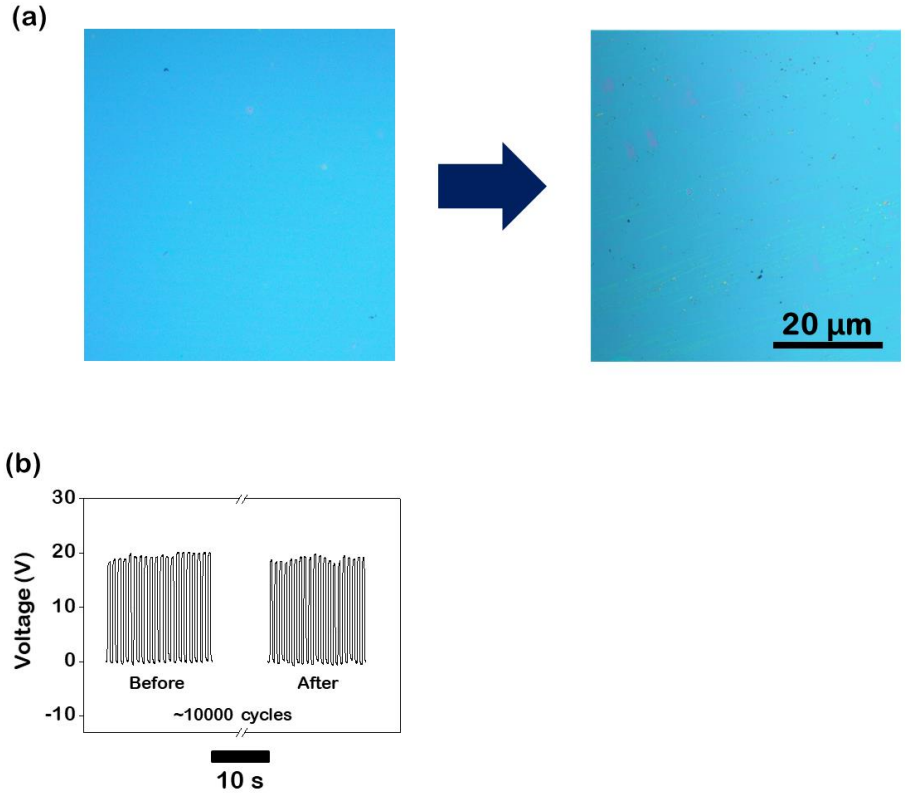

Figure 3-11. (a) Optical microscopy images of the F-MoS_2 surface before and after the durability test (tens of thousands of cycles) of TENG device.(b) Durability test of the F-TENG devices over 10000 pressing cycles.

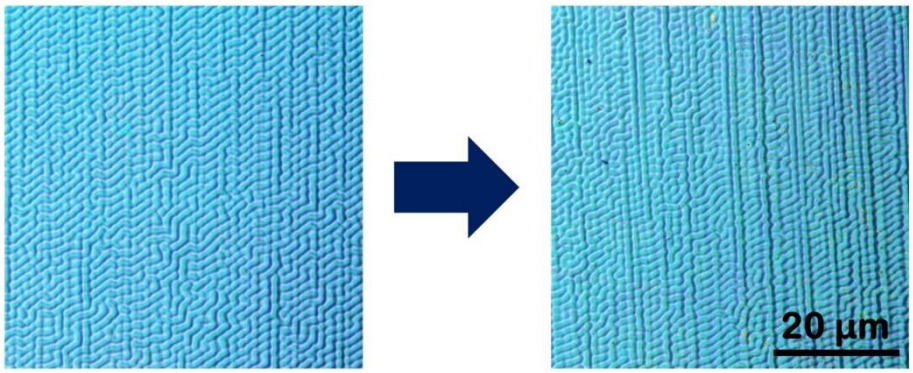

Figure 3-12. Optical microscopy images of the MC-MoS_2 surface before and after the durability test (tens of thousands of cycles) of TENG device.

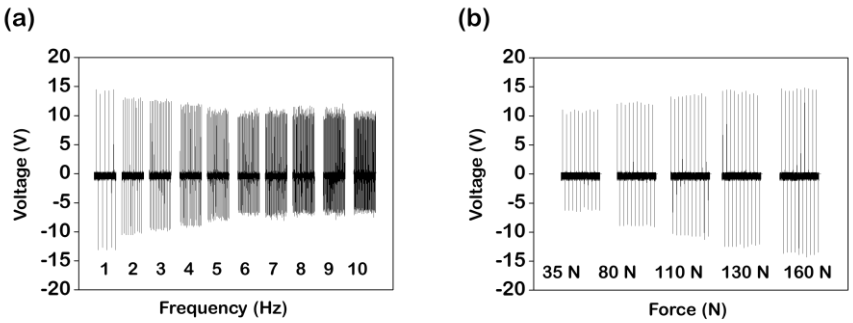

Figure 3-13. (a) Frequency and (b) applied force dependence of generated voltage signals from the MC-TENG device.

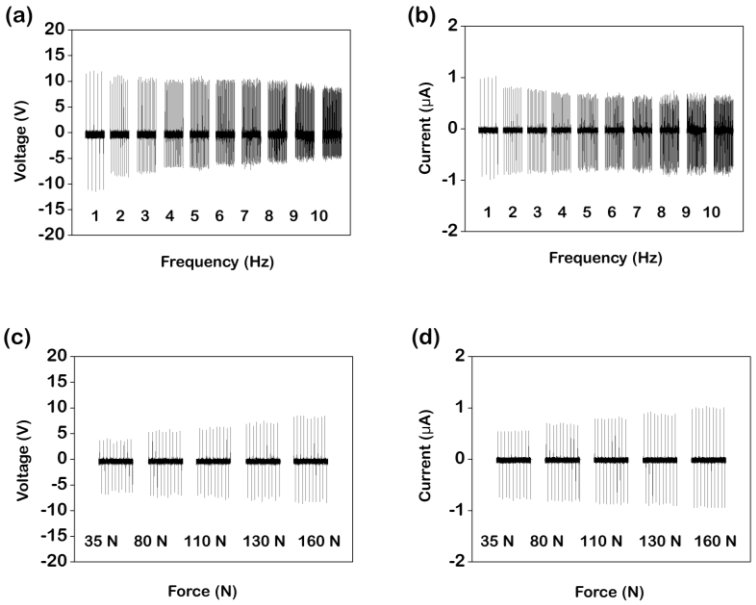

Figure 3-14. Energy harvesting output generated from the F-TENG under varied applied force and frequency. Frequency dependence of generated (a) voltage and (b) current signals. Force dependence of generated (c) voltage and (d) current signals.

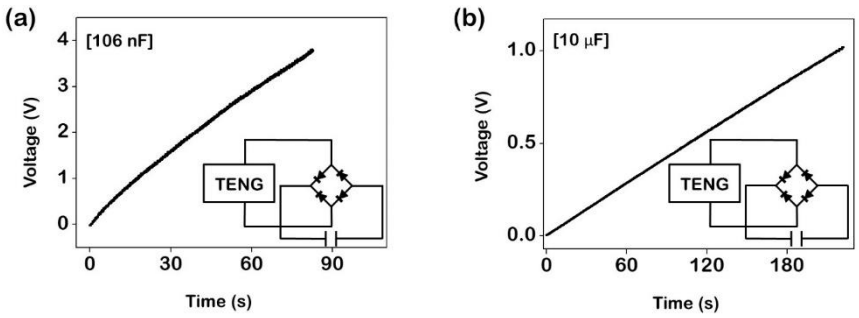

Figure 3-15. (a) 106 nF and (b) 10 uF capacitors stored by MC-TENG up to 4 V for 90 s and 1 V for 180 s, respectively. Inset: the TENG device connected with a bridge diode rectifier circuit with the capacitors.

The laser-directed synthesis method was have developed for fabricating 2D MoS_2 layers allows not only for fast, vacuum-free processing but also direct patterning methods. Accordingly, we demonstrated a flexible touch sensor array device with multi-touch and position-mapping capabilities, since energy harvesting devices can be also applied to self-powered sensor applications [12, 62]. To fabricate the flexible sensor array, a 4×4 patterned crumpled MoS_2 array was directly synthesized onto a SiO_2/Si wafer. Ag electrode lines were established on the patterned MoS_2, using an inkjet printer, dispensing with the conventional lithography procedure. The resulting Ag/ MoS_2 pattern array was transferred from the wafer onto a flexible elastomer substrate by wet etching of the SiO_2. Finally, a connector was linked to the Ag bottom electrodes of the sensor array to measure voltage signals from the self-powered flexible triboelectric sensors (Figure 3-16 a). The structure of the sensor device was based on a single-electrode triboelectric device type so as to use MoS_2 surfaces directly as triboelectric sensory pixels and to simplify fabrication processing [63, 64]. Notably, all of these fabrication steps were successfully realized, from establishing the active layers to integrating the electrode connections using direct-writing approaches (i.e., laser scribing and inkjet printing). To exclude external artifacts, in preference to human manual input the triboelectric haptic sensor array was tested using a stylus pen (Galaxy Note 9 touch pen, Samsung Electronics).

To investigate the triboelectric sensitivity of the MC-MoS_2, we also

prepared flexible sensor array devices with F-MoS_2 layers and only Ag electrodes, respectively, using the same fabrication process. As plotted in Figure 3-16 b, the MC-MoS_2 sensor far higher voltage output than the F-MoS_2 and the only Ag electrode-only devices when tested under the different force levels: 5, 10, and 20N, respectively. This suggests that the crumpling effect of the laser-directed MoS_2 may also be useful in triboelectrification with other materials. Also, the wearable haptic touch sensor was operated from various pressure, 5 N (50 kpa) to 20 N (200 kpa). Notably, the pressure of 5N means that it responds to the level of general contact pressure (40-50 kpa) as previously reported triboelectric nanogenrator-based touch pad.[ref] Multi-touch contact motion with a stylus pen along different pixels of a flexible sensor array, is illustrated in the left panel of Figure 3-16 c.

The differences in potential between touched and untouched MoS_2 pixels can be observed without serious interference, indicating the feasibility of multi-touch detection via triboelectric voltage (see right panel of Figure 3-16 c). This feature should encourage further steps towards developing 2D materials-based flexible and transparent haptic sensors. The trajectory mapping of the wearable haptic sensor consist of a self-designed 4 x 4 (row x column) matrix of square MoS_2/ Ag pattern that act as a triboelectric layer with a stylus pen. These each square patterns was connected with an electrometer and then the trajectory mapping was recognized via measuring the output voltage signal of each pixel generated in real time. Figure 3-16 d shows position mapping according to the

trajectory of stylus pen movement. The haptic sensor displayed instantaneous voltage responses, allowing for motion-mapping in response to the trajectory of the dragging content of letter (‘L’ shape) and drawing patterns (down and right). First, the stylus pen is located on (2,2) and drags down and then (2,4) to (4,4). In this trajectory, the faint-blue square is caused by induced charges to adjacent cells that occur during touch operation (< 0.8 V). The light-blue square is caused by separation when the stylus moves to another MoS_2 active layer (~ 6V). Therefore, this wearable haptic sensor was successfully demonstrated with position mapping as well as TENG.

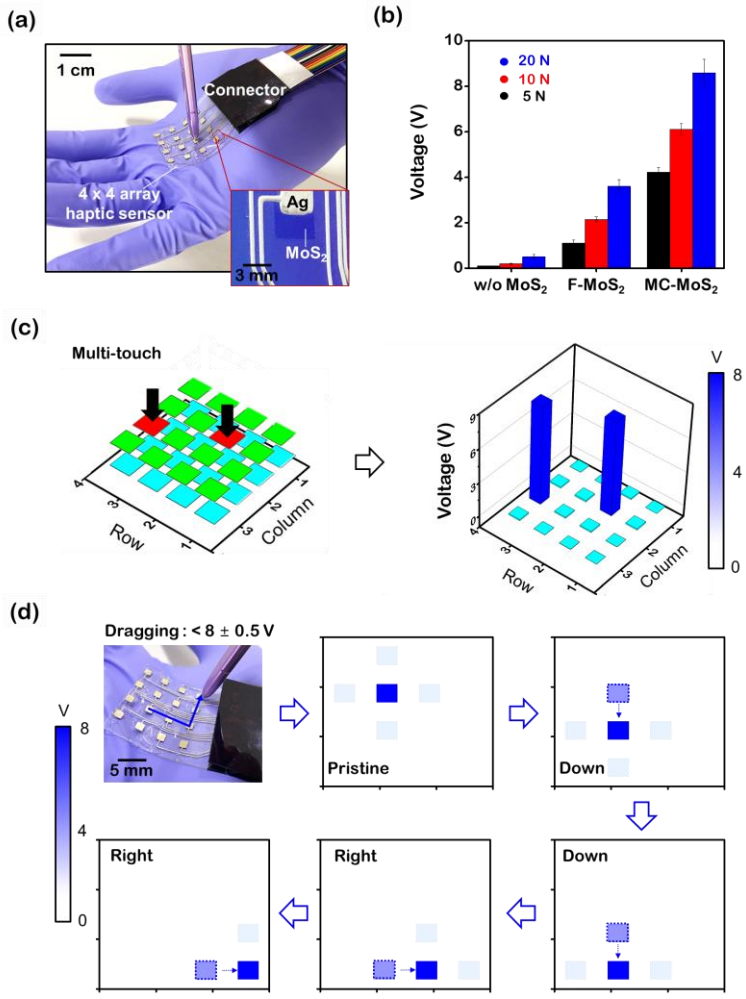

Figure 3-16. (a) Photograph of the laser-directed patterned MoS_2-based flexible triboelectric haptic sensor array on a human hand. Inset: the MC-MoS_2 and printed Ag electrode of a haptic sensor unit. (b) Triboelectric sensor output detected without the MoS_2 layer and the F- MoS_2 as well as the MC-MoS_2. (c) Multi-touch ability of triboelectric sensor signals on the hand. (d) Position mapping of trajectory of the stylus pen (touch pen) movement on the MC-

MoS_2-based flexible triboelectric haptic sensor.

3. 5. Conclusion

We have demonstrated a laser-directed synthesis method for achieving rapid, wafer-scale, and patternable 2D TMDC nanomaterial fabrication without using a vacuum. The MoS_2-surface morphology and strain can also be easily controlled by the laser irradiation with the synthesis simultaneously. The thermal-interfacial interaction was extensively studied by a variety of characterizations, as well as electronic properties. In particular, it was determined that modulating the work function of MoS_2 by surface crumpling critically affects the electron transferal process in triboelectric phenomena. Our results show not only direct development of as-synthesized MoS_2 surface roughness but also changes in work function by overall surface corrugation, thus demonstrating the importance of the electron transfer mechanism in triboelectric interaction between 2D TMDC and polymer. The crumpled MoS_2 surface synthesized by laser-directed thermolysis presented high-performance triboelectric energy harvesting output compared to previously reported MoS_2 TENG devices. The power output generated was up to 40% higher than for flat-surface MoS_2 synthesized using the same laser method. The laser-directed synthesis method was also used to fabricate a patterned MoS_2 triboelectric haptic sensor array on a flexible substrate with direct inkjet printing of electrodes. Multi-touch and position-mapping capabilities were confirmed

using flexible triboelectric sensor array. The triboelectric properties of laser-directed MoS_2 will be more inspected by additional following research about grain size, counterpart materials selection, laser source changes, etc. The present study lays the groundwork for future developments in laser synthesis of other 2D TMDC materials with modulated surface morphologies. Based on its findings, investigation of 2D TMDC materials should be broadened in order to realize milliwatt-level triboelectric energy harvesters and self-powered flexible sensors of future electronics.

3. 6. References

1. A. Ahmed, I. Hassan, M.F. El-Kady, A. Radhi, C.K. Jeong, P.R. Selvaganapathy, J. Zu, S. Ren, Q. Wang, R.B. Kaner, Integrated triboelectric nanogenerators in the era of the Internet of Things, Adv. Sci. 6 (2019) 1802230.

2. S.A. Han, J. Lee, W. Seung, J. Lee, S. Kim, J.H. Kim, Patchable and implantable 2D nanogenerator, Small (2019) 1903519.

3. B.-Y. Lee, D.H. Kim, J. Park, K.-I. Park, K.J. Lee, C.K. Jeong, Modulation of surface physics and chemistry in triboelectric energy harvesting technologies, Sci. Technol. Adv. Mater. 20 (2019) 758–773.

4. G.-J. Lee, M.-K. Lee, J.-J. Park, D.Y. Hyeon, C.K. Jeong, K.-I. Park, Piezoelectric energy harvesting from two-dimensional boron nitride nanoflakes, ACS Appl. Mater. Interfaces 11 (2019) 37920–37926.

5. Y. Zhang, H. Sun, C.K. Jeong, Biomimetic Porifera skeletal structure of lead-free piezocomposite energy harvesters, ACS Appl. Mater. Interfaces 10

(2018) 35539–35546.

6. S.S. Won, H. Seo, M. Kawahara, S. Glinsek, J. Lee, Y. Kim, C.K. Jeong, A.I. Kingon, S.-H. Kim, Flexible vibrational energy harvesting devices using strain-engineered perovskite piezoelectric thin films, Nano Energy 55 (2019) 182–192.

7. J.W. Lee, S. Jung, T.W. Lee, J. Jo, H.Y. Chae, K. Choi, J.J. Kim, J.H. Lee, C. Yang, J. M. Baik, High-output triboelectric nanogenerator based on dual inductive and resonance effects-controlled highly transparent polyimide for self-powered sensor network systems, Adv. Energy Mater. 9 (2019) 1901987.

8. I. Kim, Y. Chae, S. Jo, D. Kim, Levitating oscillator-based triboelectric nanogenerator for harvesting from rotational motion and sensing seismic oscillation, Nano Energy 72 (2020) 104674.

9. S. Niu, S. Wang, L. Lin, Y. Liu, Y.S. Zhou, Y. Hu, Z.L. Wang, Theoretical study of contact-mode triboelectric nanogenerators as an effective power source, Energy Environ. Sci. 6 (2013) 3576.

10. S. Niu, Z.L. Wang, Theoretical systems of triboelectric nanogenerators, Nano Energy 14 (2015) 161–192.

11. H. Cho, J. Chung, G. Shin, J.-Y. Sim, D.S. Kim, S. Lee, W. Hwang, Toward sustainable output generation of liquid–solid contact triboelectric nanogenerators: the role of hierarchical structures, Nano Energy 56 (2019) 56–64.

12. Y. Lee, J. Kim, B. Jang, S. Kim, B.K. Sharma, J.-H. Kim, J.-H. Ahn, Graphene-based stretchable/wearable self-powered touch sensor, Nano Energy 62 (2019) 259–267.

13. X. Chen, J.-H. Ahn, Biodegradable and bioabsorbable sensors based on

two- dimensional materials, J. Mater. Chem. B. 8 (2020) 1082–1092.

14. M. Seol, S. Kim, Y. Cho, K.-E. Byun, H. Kim, J. Kim, S.K. Kim, S.-W. Kim, H.-J. Shin, S. Park, Triboelectric series of 2D layered materials, Adv. Mater. 30 (2018) 1801210.

15. H. Wang, C.-C. Huang, T. Polcar, Triboelectrification of two-dimensional chemical vapor deposited WS_2 at nanoscale, Sci. Rep. 9 (2019) 12570.

16. H. Coy Diaz, R. Addou, M. Batzill, Interface properties of CVD grown graphene transferred onto MoS_2 (0001), Nanoscale 6 (2014) 1071–1078.

17. L. Han, M. Peng, Z. Wen, Y. Liu, Y. Zhang, Q. Zhu, H. Lei, S. Liu, L. Zheng, X. Sun, H. Li, Self-driven photodetection based on impedance matching effect between a triboelectric nanogenerator and a MoS_2 nanosheets photodetector, Nano Energy 59 (2019) 492–499.

18. S.A. Shankaregowda, C.B. Nanjegowda, X.-L. Cheng, M.-Y. Shi, Z.-F. Liu, H.- X. Zhang, A flexible and transparent graphene-based triboelectric nanogenerator, IEEE Trans. Nanotechnol. 15 (2016) 435–441.

19. H.-J. Choi, J.H. Lee, J. Jun, T.Y. Kim, S.-W. Kim, H. Lee, High-performance triboelectric nanogenerators with artificially well-tailored interlocked interfaces, Nano Energy 27 (2016) 595–601.

20. I.-W. Tcho, W.-G. Kim, S.-B. Jeon, S.-J. Park, B.J. Lee, H.-K. Bae, D. Kim, Y.-K. Choi, Surface structural analysis of a friction layer for a triboelectric nanogenerator, Nano Energy 42 (2017) 34–42.

21. M. Park, Y.J. Park, X. Chen, Y.-K. Park, M.-S. Kim, J.-H. Ahn, MoS_2-based tactile sensor for electronic skin applications, Adv. Mater. 28 (2016) 2556–2562.

22. I.J. Chung, W. Kim, W. Jang, H.-W. Park, A. Sohn, K.-B. Chung, D.-W.

Kim, D. Choi, Y.T. Park, Layer-by-layer assembled graphene multilayers on multidimensional surfaces for highly durable, scalable, and wearable triboelectric nanogenerators, J. Mater. Chem. A. 6 (2018) 3108–3115.

23. X. Ma, S. Li, S. Dong, J. Nie, M. Iwamoto, S. Lin, L. Zheng, X. Chen, Regulating the output performance of triboelectric nanogenerator by using P(VDF-TrFE) Langmuir monolayers, Nano Energy 66 (2019) 104090.

24. J.L. Brito, M. Ilija, P. Hern´andez, Thermal and reductive decomposition of ammonium thiomolybdates, Thermochim. Acta 256 (1995) 325–338.

25. K.-K. Liu, W. Zhang, Y.-H. Lee, Y.-C. Lin, M.-T. Chang, C.-Y. Su, C.-S. Chang, H. Li, Y. Shi, H. Zhang, C.-S. Lai, L.-J. Li, Growth of large-area and highly crystalline MoS_2 thin layers on insulating substrates, Nano Lett. 12 (2012) 1538–1544.

26. A. Giri, G. Park, H. Yang, M. Pal, J. Kwak, U. Jeong, Synthesis of 2D metal chalcogenide thin films through the process involving solution-phase deposition, Adv. Mater. 30 (2018) 1707577.

27. Z. Zhang, P. Chen, X. Yang, Y. Liu, H. Ma, J. Li, B. Zhao, J. Luo, X. Duan, X. Duan, Ultrafast growth of large single crystals of monolayer WS_2 and WSe_2, Natl. Sci. Rev. (2020).

28. N.B. Shinde, B. Francis, M.S. Ramachandra Rao, B.D. Ryu, S. Chandramohan, S. K. Eswaran, Rapid wafer-scale fabrication with layer-by-layer thickness control of atomically thin MoS_2 films using gas-phase chemical vapor deposition, Apl. Mater. 7 (2019), 081113.

29. T.H. Im, D.Y. Park, H.K. Lee, J.H. Park, C.K. Jeong, D.J. Joe, K.J. Lee, Xenon flash lamp-induced ultrafast multilayer graphene growth, Part. Part. Syst. Char. 34 (2017) 1600429.

30. Z. Yang, J. Hao, Progress in pulsed laser deposited two-dimensional layered

materials for device applications, J. Mater. Chem. C. 4 (2016) 8859–8878.

31. S.-K. Hyeong, K.-H. Choi, S.-W. Park, S. Bae, M. Park, S. Ryu, J.-H. Lee, S.-K. Lee, Review of the direct laser synthesis of functionalized graphene and its application in sensor technology, Appl. Sci. Converg. Technol. 28 (2019) 148–154.

32. J.H. Park, H.E. Lee, C.K. Jeong, D.H. Kim, S.K. Hong, K.-I. Park, K.J. Lee, Self- powered flexible electronics beyond thermal limits, Nano Energy 56 (2019) 531–546.

33. E. Kobeda, Intrinsic SiO_2 film stress measurements on thermally oxidized Si, J. Vac. Sci. Technol. B Microelectron. Nanom. Struct. 5 (1987) 15.

34. J.T. Fitch, Intrinsic stress and stress gradients at the SiO_2/ Si interface in structures prepared by thermal oxidation of Si and subjected to rapid thermal annealing, J. Vac. Sci. Technol. B Microelectron. Nanom. Struct. 7 (1989) 775.

35. K.T. Queeney, M.K. Weldon, J.P. Chang, Y.J. Chabal, A.B. Gurevich, J. Sapjeta, R. L. Opila, Infrared spectroscopic analysis of the Si/ SiO_2 interface structure of thermally oxidized silicon, J. Appl. Phys. 87 (2000) 1322–1330.

36. J. Jadwiszczak, C. O'Callaghan, Y. Zhou, D.S. Fox, E. Weitz, D. Keane, C.P. Cullen, I. O'Reilly, C. Downing, A. Shmeliov, P. Maguire, J.J. Gough, C. McGuinness, M. S. Ferreira, A.L. Bradley, J.J. Boland, G.S. Duesberg, V. Nicolosi, H. Zhang, Oxide- mediated recovery of field-effect mobility in plasma-treated MoS_2, Sci. Adv. 4 (2018).

37. H. Li, A.W. Contryman, X. Qian, S.M. Ardakani, Y. Gong, X. Wang, J.M. Weisse, C. H. Lee, J. Zhao, P.M. Ajayan, J. Li, H.C. Manoharan, X. Zheng, Optoelectronic crystal of artificial atoms in strain-textured molybdenum disulphide, Nat. Commun. 6 (2015) 7381.

38. C. Rice, R.J. Young, R. Zan, U. Bangert, D. Wolverson, T. Georgiou, R. Jalil, K. S. Novoselov, Raman-scattering measurements and first-principles calculations of strain-induced phonon shifts in monolayer MoS_2, Phys. Rev. B 87 (2013), 081307.

39. A. Castellanos-Gomez, R. Rold´an, E. Cappelluti, M. Buscema, F. Guinea, H.S.J. van der Zant, G.A. Steele, Local strain engineering in atomically thin MoS 2, Nano Lett. 13 (2013) 5361–5366.

40. S. Pak, J. Lee, Y.-W. Lee, A.-R. Jang, S. Ahn, K.Y. Ma, Y. Cho, J. Hong, S. Lee, H. Y. Jeong, H. Im, H.S. Shin, S.M. Morris, S. Cha, J.I. Sohn, J.M. Kim, Strain- Mediated interlayer coupling effects on the excitonic behaviors in an epitaxially grown MoS_2/ WS_2 van der Waals heterobilayer, Nano Lett. 17 (2017) 5634–5640.

41. M. Hosseini, M. Elahi, M. Pourfath, D. Esseni, Strain-induced modulation of electron mobility in single-layer transition metal dichalcogenides MX_2 (M =Mo, W ; X =S, Se), IEEE Trans. Electron. Dev. 62 (2015) 3192–3198.

42. J. Lee, Y.R. Lim, A.K. Katiyar, W. Song, J. Lim, S. Bae, T. Kim, S. Lee, J. Ahn, Direct synthesis of a self-assembled WSe_2/MoS_2 heterostructure array and its optoelectrical properties, Adv. Mater. 31 (2019) 1904194.

43. N.A. Lanzillo, A.J. Simbeck, S.K. Nayak, Strain engineering the work function in monolayer metal dichalcogenides, J. Phys. Condens. Matter 27 (2015) 175501.

44. J. Shakya, S. Kumar, D. Kanjilal, T. Mohanty, Work function modulation of molybdenum disulfide nanosheets by introducing systematic lattice strain, Sci. Rep. 7 (2017) 9576.

45. Y. Wang, J. Duan, X. Yang, L. Liu, L. Zhao, Q. Tang, The unique dielectricity of inorganic perovskites toward high-performance triboelectric

nanogenerators, Nano Energy 69 (2020) 104418.

46. C. Xu, B. Zhang, A.C. Wang, W. Cai, Y. Zi, P. Feng, Z.L. Wang, Effects of metal work function and contact potential difference on electron thermionic emission in contact electrification, Adv. Funct. Mater. 29 (2019) 1903142.

47. S. Pan, Z. Zhang, Triboelectric effect: a new perspective on electron transfer process, J. Appl. Phys. 122 (2017) 144302.

48 J. Liu, M. Miao, K. Jiang, F. Khan, A. Goswami, R. McGee, Z. Li, L. Nguyen, Z. Hu, J. Lee, K. Cadien, T. Thundat, Sustained electron tunneling at unbiased metal- insulator-semiconductor triboelectric contacts, Nano Energy 48 (2018) 320–326.

49. C.K. Jeong, K.M. Baek, S. Niu, T.W. Nam, Y.H. Hur, D.Y. Park, G.-T. Hwang, M. Byun, Z.L. Wang, Y.S. Jung, K.J. Lee, Topographically-designed triboelectric nanogenerator via block copolymer self-assembly, Nano Lett. 14 (2014) 7031–7038.

50. S. Pan, Z. Zhang, Fundamental theories and basic principles of triboelectric effect: a review, Friction 7 (2019) 2–17.

51. A. ˇSutka, K. M¯alnieks, L. Lapˇcinskis, P. Kaufelde, A. Linarts, A. B¯erzin¸a, R. Z¯abels, V. Jurk¸¯ans, I. Gorn¸evs, J. Bl¯ums, M. Knite, The role of intermolecular forces in contact electrification on polymer surfaces and triboelectric nanogenerators, Energy Environ. Sci. 12 (2019) 2417–2421.

52. M. Kim, S.H. Kim, M.U. Park, C. Lee, M. Kim, Y. Yi, K.-H. Yoo, MoS_2 triboelectric nanogenerators based on depletion layers, Nano Energy 65 (2019) 104079.

53. T. Ma, Z. Liu, J. Wen, Y. Gao, X. Ren, H. Chen, C. Jin, X.-L. Ma, N. Xu, H.-M. Cheng, W. Ren, Tailoring the thermal and electrical transport properties of graphene films by grain size engineering, Nat. Commun. 8

(2017) 14486.

54. J. Wang, X. Wang, J. Yu, T. Xiao, L. Peng, L. Fan, C. Wang, Q. Shen, W. Wu, Tailoring the grain size of Bi-layer graphene by pulsed laser deposition, Nanomaterials 8 (2018) 885.

55. J. Seo, Y. Kim, W.Y. Park, J.Y. Son, C.K. Jeong, H. Kim, W.-H. Kim, Out-of-plane piezoresponse of monolayer MoS_2 on plastic substrates enabled by highly uniform and layer-controllable CVD, Appl. Surf. Sci. 487 (2019) 1356–1361.

56. T.D. Nguyen, S. Mao, Y.-W. Yeh, P.K. Purohit, M.C. McAlpine, Nanoscale flexoelectricity, Adv. Mater. 25 (2013) 946–974.

57. I. Chae, C.K. Jeong, Z. Ounaies, S.H. Kim, Review on electromechanical coupling properties of biomaterials, ACS Appl. Bio Mater. 1 (2018) 936–953.

58. D. Seol, B. Kim, Y. Kim, Non-piezoelectric effects in piezoresponse force microscopy, Curr. Appl. Phys. 17 (2017) 661–674.

59. L. Lapˇcinskis, K. M¯alnieks, J. Bl¯ums, M. Knite, S. Oras, T. K¨a¨ambre, S. Vlassov, M. Antsov, M. Timusk, A. ˇSutka, The adhesion-enhanced contact electrification and efficiency of triboelectric nanogenerators, Macromol. Mater. Eng. 305 (2020) 1900638.

60. Y.J. Kim, J. Lee, S. Park, C. Park, C. Park, H.-J. Choi, Effect of the relative permittivity of oxides on the performance of triboelectric nanogenerators, RSC Adv. 7 (2017) 49368–49373.

61. X. Xie, Z. Wen, Q. Shen, C. Chen, M. Peng, Y. Yang, N. Sun, P. Cheng, H. Shao, Y. Zhang, Q. Zhu, X. Chen, X. Sun, Impedance matching effect between a triboelectric nanogenerator and a piezoresistive pressure sensor induced self- powered weighing, Adv. Mater. Technol. 3 (2018) 1800054.

62. W. Liu, X. Wang, Y. Song, R. Cao, L. Wang, Z. Yan, G. Shan, Self-powered forest fire alarm system based on impedance matching effect between triboelectric nanogenerator and thermosensitive sensor, Nano Energy 73 (2020) 104843.

63. X.-S. Zhang, M.-D. Han, R.-X. Wang, F.-Y. Zhu, Z.-H. Li, W. Wang, H.-X. Zhang, Frequency-multiplication high-output triboelectric nanogenerator for sustainably powering biomedical microsystems, Nano Lett. 13 (2013) 1168–1172.

64. X. Xiao, X. Zhang, S. Wang, H. Ouyang, P. Chen, L. Song, H. Yuan, Y. Ji, P. Wang, Z. Li, M. Xu, Z.L. Wang, Honeycomb structure inspired triboelectric nanogenerator for highly effective vibration energy harvesting and self-powered engine condition monitoring, Adv. Energy Mater. 9 (2019) 1902460.

65. H. Zhang, Y. Lu, A. Ghaffarinejad, P. Basset, Progressive contact-separate triboelectric nanogenerator based on conductive polyurethane foam regulated with a Bennet doubler conditioning circuit, Nano Energy 51 (2018) 10–18.

66. Y. Su, C. Dagdeviren, R. Li, Measured output voltages of piezoelectric devices depend on the resistance of voltmeter, Adv. Funct. Mater. 25 (2015) 5320–5325, https://doi.org/10.1002/adfm.201502280.

67. B. Dudem, N.D. Huynh, W. Kim, D.H. Kim, H.J. Hwang, D. Choi, J.S. Yu, Nanopillar-array architectured PDMS-based triboelectric nanogenerator integrated with a windmill model for effective wind energy harvesting, Nano Energy 42 (2017) 269–281.

68. D. Jang, Y. Kim, T.Y. Kim, K. Koh, U. Jeong, J. Cho, Force-assembled triboelectric nanogenerator with high-humidity-resistant electricity generation using hierarchical surface morphology, Nano Energy 20 (2016)

283–293.

69. Z. Yuan, T. Zhou, Y. Yin, R. Cao, C. Li, Z.L. Wang, Transparent and flexible triboelectric sensing array for touch security applications, ACS Nano 11 (2017) 8364–8369.

70. I.-W. Tcho, W.-G. Kim, Y.-K. Choi, A self-powered character recognition device based on a triboelectric nanogenerator, Nano Energy 70 (2020) 104534.

71. W. Kim, D. Choi, J.-Y. Kwon, D. Choi, A self-powered triboelectric microfluidic system for liquid sensing, J. Mater. Chem. A. 6 (2018) 14069–14076.

72. H. Chu, H. Jang, Y. Lee, Y. Chae, J.-H. Ahn, Conformal, graphene-based triboelectric nanogenerator for self-powered wearable electronics, Nano Energy 27 (2016) 298–305.

73. H. Wang, M. Shi, K. Zhu, Z. Su, X. Cheng, Y. Song, X. Chen, Z. Liao, M. Zhang, H. Zhang, High performance triboelectric nanogenerators with aligned carbon nanotubes, Nanoscale 8 (2016) 18489–18494.

Chapter 4. Conclusion

In this thesis, the synthesis of transition metal dichalcogenides, e.g., MoS_2, WS_2, and silver nanoparticles based wearable electronic devices are described, respectively.

In Chapter 2, we have successfully demonstrated the fabrication of patterned semiconducting MoS_2 and WS_2 films over a large area under ambient conditions using a rapid pyrolysis *via* laser annealing method. The resulting capabilities could facilitate applications not only in the fabrication of wafer-scale transistor arrays but also in customized electronics that require the formation of various patterns in a short time even under air condition. The obvious advantages, such as the ultrafast fabrication speed with process simplification, solution-based scalable/inexpensive process, and open-chamber process, are highly compatible with mass production. Our study is expected to contribute to the realization of high-performance TMD-based electronics with a similar technique as for present silicon-based electronics.

Chapter 3 describes a laser-directed synthesis method for achieving rapid, wafer-scale, and patternable 2D TMDC nanomaterial fabrication without using a vacuum. The MoS_2-surface morphology and strain can also be easily controlled by the laser irradiation with the synthesis simultaneously. The thermal-interfacial interaction was extensively studied by a variety of characterizations, as well as electronic properties. In particular, it was determined that modulating the work function of MoS_2 by surface crumpling

critically affects the electron transferal process in triboelectric phenomena. The power output generated was up to 40% higher than for flat-surface MoS_2 synthesized using the same laser method. The laser-directed synthesis method was also used to fabricate a patterned MoS_2 triboelectric haptic sensor array on a flexible substrate with direct inkjet printing of electrodes. Multi-touch and position-mapping capabilities were confirmed using flexible triboelectric sensor array.

In conclusion, we proposed the direct patterning method with simultaneous synthesis of TMDCs. This method begins with solution phase of precursor deposition, and then layer-selective annealing was applied onto the precursor or chemical reduction. Such processes lead to fast processing time without additional patterning steps. As a results, large-scale low-dimensional growth was successfully achieved as applicable transistor, strain gauge, and diode. Furthermore, work function modulation was demonstrated by strain-induced effects toward enhancing self-powered nanogenerator. Throughout of the profits, these method paves a way to next-generation electronic devices, which could apply to flexible, stretchable, and transparent material based wearable electronics.

요 약 (국문초록)

전이금속계화합물은 뛰어난 기계적, 광학적, 전기적 특성으로 인해 차세대 상업용 플렉시블 로직 디바이스 및 센서를 개발하기위한 탁월한 플랫폼으로 입을 수 있는 전자기기 제작을 위한 폼 팩터를 부여할 수 있습니다. 이를 구현하기 위해 전이금속계화합물의 대면적 박막 합성법은 복잡한 진공 기반 접근 방식을 거치는 문제점을 지녀왔습니다. 따라서, 임의의 기판 위에 대면적 전이금속계화합물 박막을 합성하여 대량 생산을 진행할 수 있는 간단하고 효과적인 방법을 개발하는 것이 중요합니다. 이 점에서 용액 기반 전이금속계화합물 합성 방법은 비 진공 분위기에서 제조 공정의 단순화와 대면적화를 동시에 이룰 수 있는 효율적인 합성법입니다.

제 1 장에서는 용액공정 기반의 전이금속계화합물 전구체 박막 증착 및 합성의 발전 과정을 요약하고, 증착 된 전구체를 열분해 시켜서 전이금속계화합물 박막으로 형성하는 합성 방법의 장단점에 대해 논의합니다. 마지막으로는 전자기기 및 센서에서 미래에 적용 가능한 응용분야에 대해 설명합니다.

제 2 장에서는 비진공 상태에서 펄스 레이저 어닐링 기법 (λ = 1.06 μm, 펄스 지속 시간 ~ 100 ps)을 사용하여 웨이퍼 규모에서 이황화몰리브데넘 및 이황화텅스텐 구조의 층간 선택 합성을 위한 직접적이고 신속한 제작 방법을 소개합니다. 그 결과 이황화몰리브데넘 기반 전계 효과 트랜지스터, 피부 부착 형 모션 센서 및

이황화몰리브데넘/이황화텅스텐 기반 이종 접합 다이오드의 동작을 시연했습니다.

제 3 장에서는 표면이 구겨진 형태를 가지는 이황화몰리브데넘 기반 마찰 전기 발생 장치를 제작하여 기존의 이황화 몰리브데넘 대비 약 40 % 향상된 전력을 가지는 이황화몰리브데넘의 형태학적 구조를 손쉽게 조절하는 합성법을 소개합니다. 표면이 구겨진 형태의 이황화몰리브데넘 기반 마찰 전기 발생 장치는 추가 공정 및 재료의 도움없이 고성능 에너지 수확 효율을 최대 ~ 25V 및 ~ 1.2 μA 까지 보여줍니다.

마지막으로, 4 장에서는 위 실험들에 관한 결론을 기술 하는 것으로 이 논문을 마무리하였다.

주요어: 전이금속계화합물, 광원 열처리, 용액 공정, 전자소자, 스트레인 센서

학번: 2019-35429

박 성 웅